Structural and functional principles of long-range connectivity in the rat vibrissal system

Dissertation

For obtaining the degree of

Doctor of Philosophy

The Medical Faculty

Rheinische Friedrich-Wilhelms-Universität Bonn

Presented by

Jason Michael Guest

From Miami, Florida USA

June 2020

Structural and functional principles of long-range connectivity in the rat vibrissal system

Dissertation

For obtaining the degree of

Doctor of Philosophy

The Medical Faculty

Rheinische Friedrich-Wilhelms-Universität Bonn

Presented by

Jason Michael Guest

From Miami, Florida USA

June 2020

Made with permission

The Medical Faculty of the University of Bonn

1st reviewer: Dr. Marcel Oberlaender

2nd reviewer: Prof. Dr. Heinz Beck

Day of the oral exam: October 29th 2020

Center of Advanced European Studies and Research

Managing Scientific Director: Dr. Kevin Briggman

Scientific Director: Prof. Dr. Jason Kerr

Contents

Abbreviations

AP	action potential
CC	cortico-cortical
CTB	cholera toxin beta subunit
FG	fluorogold
FN	facial nucleus
IC	Intra-cortical
ITs	intratelencephalic
L2/3	layer 2 and layer 3 of the neocortex
L3	layer 3 of the neocortex
L4	layer 4 of the neocortex
L5	layer 5 of the neocortex
L5PTs	layer 5 pyramidal tract neurons
L6	layer 6 of the neocortex
LFP	local field potential
PB	sodium phosphate buffer
PFA	paraformaldehyde
Pn, Pons	pontine nucleus
PNs	pyramidal neurons
Pom	posterior-medial thalamus
PTs	pyramidal tract neurons
rAAV	recombinant adeno associated virus serotype 2/1 expressing channel rhodopsin, mCherry, synapsin under a CAG promoter
SC	superior colliculus
SP5C	spinal trigeminal nucleus caudalis
TC	thalamo-cortical
TX	triton x-100
VGlut2	vesicular-glutamate transporter 2
VL	ventro-lateral
VPM	ventro-posterior-medial thalamus
vS1	vibrissal part of the somatosensory cortex
wMNs	whisker motor neurons

Chapter 1

Introduction

Anatomical and functional principles of long-range connectivity in the mammalian brain has been a major area of research in neuroscience. Decades of classical anatomy, physiology and advanced imaging studies have revealed many long-range pathways that are imbedded in complex neural networks throughout the brain. Examples of long-range pathways include ascending thalamo-cortical (TC) circuits that relay sensory information to primary neocortical areas, descending pathways from long-range projecting pyramidal tract neurons (PTs) and cortical-cortical (CC) projections interconnecting different cortical areas all organized with and between neural systems [1]. Long-range pathways have been shown to be necessary components for neuronal signaling between brain areas, serve essential roles in sensory information processing and may be important for cognitive brain functions (reviewed in [2-4]). CC top-down projections from the secondary motor cortex in mice have been shown to modulate the sensory-evoked activity of PTs in layer 5 (L5) of auditory cortex [5]. Through descending long-range projecting axons, PTs in L5 of the neocortex, in part function to provide motor and sensory output signals to various downstream brain areas [6]. Ascending pathways that comprise of TC

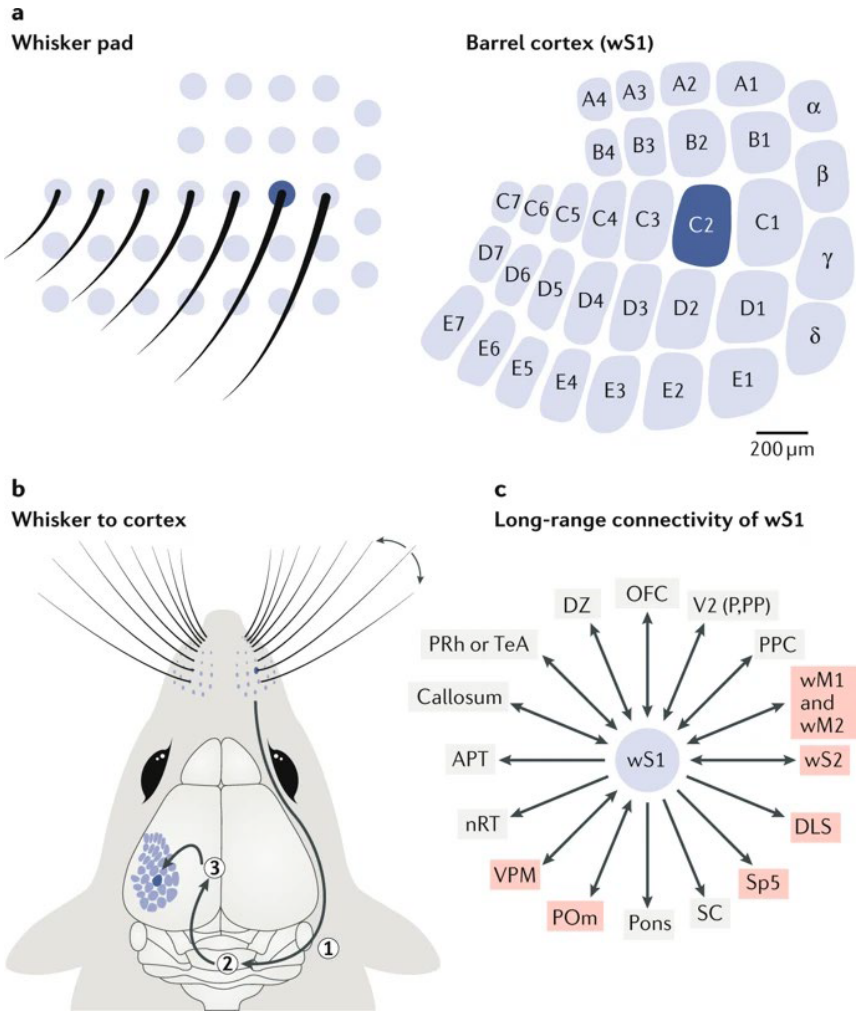

Figure1.1: Structural connectivity in rodent whisker system. (A) Left: Schematic illustrating the macro-vibrissa (major whiskers) on the mystacial pad of the snout. Left: Schematic illustrating the somatotopic organization of whisker “barrels” in layer 4 of vS1. (B) Whisker touch evokes excitation in an ascending pathway sending tactile sensory information to the trigeminal nuclei in the brainstem propagating into the thalamus then relayed into the neocortex. (C). Schematic illustrating the long-range input and output pathways involved in whisker-related sensory information processing [7-10]. APT, anterior pretectal nucleus; DLS, dorsolateral striatum; DZ, dysgranular zone surrounding wS1; nRT, nucleus reticularis of the thalamus; OFC, orbitofrontal cortex; POm, posterior medial nucleus of the thalamus; PPC, posterior parietal cortex; PRh, perirhinal cortex; SC, superior colliculus; Sp5, spinal trigeminal nuclei; TeA, temporal association cortex; wM1, whisker-related primary motor cortex; wM2, whisker-related secondary motor cortex; wS2, whisker-related secondary somatosensory cortex; VPM, ventral posterior medial nucleus of the thalamus; V2 (P,PP), secondary visual area. Figure is adopted from [11]

projections, function to relay information to the neocortex upon sensory stimulation, have been shown to coordinate the integration of distant brain regions and can regulate cortical states [12-14]. For the purposes of the thesis I will focus on long-range pathways that comprise of TC connections and neocortical output pathways originating from L5PTs within the rat whisker system.

The ventro-posterior-medial thalamus (VPM) is part of an ascending pathway that relays tactile-based sensory information to the vibrissal part of the primary somatosensory cortex (vS1) (for a review of the rodent whisker system see [11, 15] Figure 1.1). The VPM projects long-range axon collaterals to provide synchronous and sustained excitatory inputs to all excitatory morphological cell types in vS1 [16-18]. Cortically processed information is then sent out of vS1 to other cortical areas from intratelencephalic (IT) neurons in L2/3 and L5 [19-21] or to subcortical brain areas via long-range projections from L5PTs [20].

The following description of the morphology and function of neocortical layer 5 pyramidal neurons and the description of an IC gating mechanism to explain the origins of L5PTs broadly tuned sensory-evoked responses are adapted from Piloni, Guest, et al. 2017 [22] and Egger, Narayanan, Guest et al. 2020 [23].

L5PTs are fundamental components of cortical circuitry and represent the primary output cell type of the neocortex [24]. Having a complex dendritic arbor that can reach all six layer of the neocortex, L5PTs receive synaptic input patterns from practically all types of excitatory and inhibitory neurons. Integrating feedforward TC and recurrent IC inputs with those from top down CC populations, L5PTs broadcast the results of cortical processing via descending projections outside of the neocortex (reviewed in [25]).

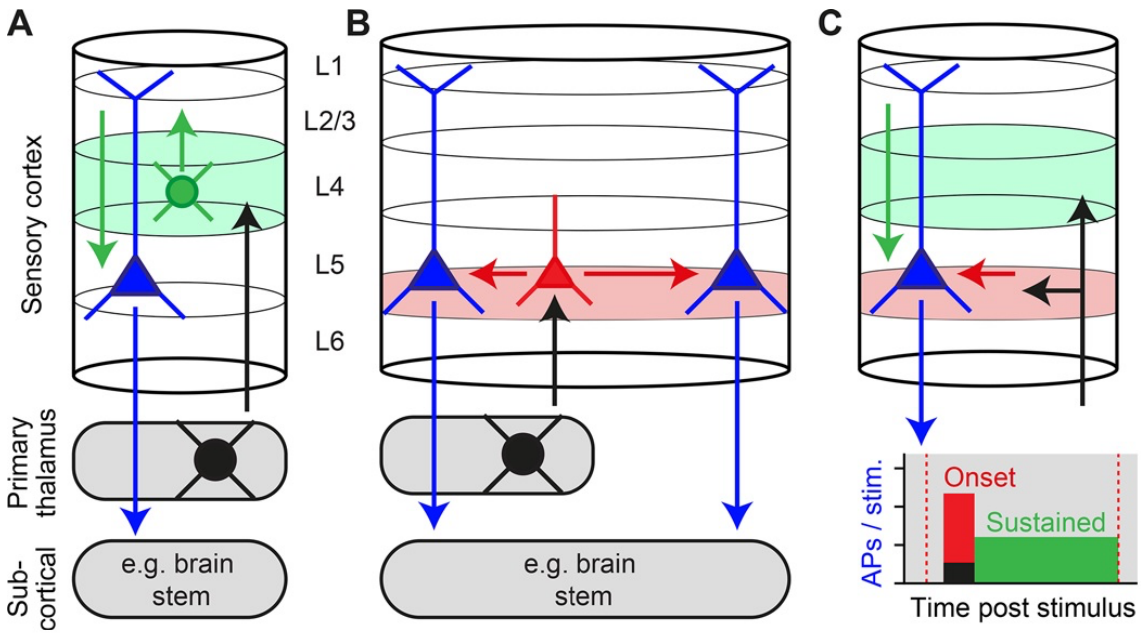

Figure 1.2: Suggested organizational model of information processing in primary sensory cortex by complementary pathways. (A) TC sensory evoked input is relayed vertical to L2/3 via L4SPs. (B) Thalamorecipient pathway in the deep layers activates L5PTs, and L5 is the terminal point of signal flow from the upper layers. (C) The complementary pathway theory therefore provides a possible explanation for sensory-evoked sustained responses observed for L5PTs. Figure is adopted from [23]

Compared to other pyramidal neuron cell types in the cortex, L5PTs have relatively sparse IC axon projections [26], evidence that L5PTs may have a limited involvement in local computations. L5PTs project glutamatergic long-range projections thereby providing excitatory input to several subcortical brain areas [6, 27]. The subcortical long-range axonal targets usually depend on the cortical area the L5PTs is located in, but vary from neuron to neuron even within the same cortical area (reviewed in [28]). Therefore L5PTs are thought to represent an end point of local cortical circuits by integrating specific

combinations of local and long-range inputs and sending the results of this integration to their respective subcortical axonal targets [19].

One hallmark functional feature of L5PTs is their reliable and broadly tuned action potential (AP) responses to sensory stimulation [29, 30]. The onset sensory evoked AP responses of L5PTs can often be more reliable and even be faster than those in the primary input layer 4 [31]. In 2013, a study by Constantinople and Bruno [32], the authors reported that the fast onset AP responses of L5PTs are driven directly by sensory-evoked synaptic inputs from the VPM. However, direct evidence that primary TC projections alone are sufficient to drive sensory evoked AP responses in L5PTs especially with respect their broad receptive field response properties was still lacking. Therefore in a study that was published in 2020 by Egger, Narayanan, Guest et al. [23] in which I was a contributing author, sought to provide such direct evidence for the mechanistic origins of the L5PTs' ability to respond to a broad range of stimuli with onset latencies that rival and even precede those of their IC input neurons. My co-authors and I successfully reported the discovery of an IC gating mechanism by which CC excitatory neurons in L6 act to provide input to L5PTs throughout the cortical area to amplify additional inputs from TC and other IC populations. The fast onsets and broadly tuned characteristics of L5PT responses therefore reflect this gating mechanism in the deep layers [23] (Figure 1.2). Therefore if the AP activity of L5PTs is not directly driven by primary TC connections alone, then their functional role in L5PTs ability to transform sensory-evoked input into cortical output activity patterns still remains unknown.

The primary focus of this thesis is to explore what functional role the primary thalamus (VPM) might play in transforming sensory-evoked input into output activity by

neocortical L5PTs with respect to their long-range subcortical targets. In addition to L5PTs, L5 of the neocortex consists of a second morphological excitatory neuron type, the L5ITs. L5ITs project long-range axons to the striatum and to other cortical brain areas [20, 33]. Though the morphology and physiology of L5PTs is widely consistent across the neocortex, it is different from that of L5ITs [19]. L5ITs and L5PTs have been shown to process corresponding sensory information, both in the mouse primary visual cortex (V1) [34] and also in vS1 [35, 36]. There are studies that have suggested that L5ITs may have diverse functional roles when processing the same sensory stimulus that depends on the cortical area they project their long-range axons into. For example, ITs located in L3 of mouse vS1 were reported to project long-range axons either to the whisker related part of the primary motor cortex (vM1) or secondary somatosensory cortex (vS2). A larger portion of vS2 projecting ITs than vM1 projecting ITs showed whisker touch-related responses during texture discrimination, whereas the opposite was found during an object detection task [21]. Therefore in a collaborative effort I investigated whether L5PTs in vS1 have structural and functional properties that relate to the subcortical targets they project to. In addition, in order to bring further insight into how long-range inputs from the primary thalamus may contribute to cortical output activity, I investigated the structural organization of primary TC synapses on the dendrites of L5PTs.

Here in this thesis, I will report several new structural and functional principles of long-range pathways involving cortical output and primary thalamic input. By combining multiple in vivo functional and anatomical experimental methods I will provide empirical evidence for the following: As observed for ITs in the L3 of vS1 [21] and L5 of V1 [37], L5PTs in rat vS1 also have structural and functional properties that reflect their respective

long-range axonal subcortical targets. L5PTs have soma depth locations and layer-specific dendrite distributions that allow for predicting the subcortical target they project to. Additionally L5PTs have AP spiking patterns during both periods of ongoing activity and during sensory stimulation that are also target-related. In order to find an anatomical basis for the target-related function of L5PTs, I also investigated the brain-wide structural organization of whisker-related neuronal networks, to explore whether L5PTs may be imbedded in long-range target-specific subnetworks. I find that L5PTs that project to the brainstem have a shorter synaptic distance to the whisker muscles compared to L5PTs with different targets and find anatomical evidence that L5PTs may integrate inputs from different presynaptic neuronal populations depending on the subcortical brain area they target. Finally, by investigating the structural organization of primary TC inputs in vS1, I find that the same neurons in the thalamus that provide feedforward excitation to the basal dendrites of L5PTs, additionally and specifically form a dense area of synaptic connections on the apical dendrite that corresponds with the location of calcium channels.

Chapter 2

Methods

Note: The description of these methods is in part adopted from Piloni, Guest et al. 2017, Guest et al. 2018, and Egger, Narayanan, Guest et al. 2020 [22], [38], [23]

2.1 Stereotaxic injection of neuronal tracer agents

All experimental procedures were carried out after evaluation by the local German authorities, in accordance with the animal welfare guidelines of the Max Planck Society and under sterile conditions. For animals described below in section 2.1.4 injected with the replication competent N2c strain of rabies virus: all experimental procedures were conducted at the University of Pittsburgh and in accordance with National Institutes Health guidelines and were approved by the relevant Institutional Animal Care and Use and Biosafety Committees. Animal were housed in a vivarium with normal day/night cycles and in groups of 2 animals per cage. Please note: all rats injected with retrograde tracers into subcortical brain structures (Pons, SP5C, S.C. and POm) as well as the in vivo recordings of these retrograde tracer injected rats were performed by Gerardo Rojas-Piloni at the Max Plank Florida Institute for Neuroscience (Jupiter, Fl. USA). All other procedures involving tracer injections and in vivo recordings described below were performed by myself at the Center of Advanced Studies and Research (Bonn, Germany) or at the University of Pittsburgh (Pittsburgh, Pa. USA).

2.1.1 Injection of monosynaptic neuronal tracers into subcortical brain structures

Young adult (P22-P35) male Wistar rats (Charles River) were injected with 1mg/ml buprenorphine (.1ml/100g .i.p.) approxamatley 30 minutes prior to surgery. Rats were then anesthetized with ketamine-xylazine mixture (70/6mg/kg i.p.) and supplemented with isofluorane/O2 gas. Rats were placed in a stereotaxic frame (Kopf Instruments, model 1900) and given an injection of .25% bupivacaine (0.10cc, s.q.) at the incision site. Then a 5 cm incision across the midline, just past the base of the neck was made to expose the skull. Both bregma and lambda were located and marked with a surgical pen. A small craniotomy (or craniotomies for multiple site injection experiments) in the skull was made using a dental drill (Osada, model EXL-M40) over the injection site of the right cerebral hemisphere (for Sp5C injections no craniotomy was necessary). Injection site coordinates were as follows (in mm): Pom: 2.1 lateral from midline, 3.25 posterior to bregma and 5.2 deep from the pia; Vpm: 3.25 from the midline, 2.9 posterior from bregma and 5.5mm deep from pia; SC: 1.3 from the midline, 2.0 anterior to lambda and 3.5 deep from the pia; Pons: 1.1 from the midline, 1.8 anterior to lambda and 8.5 deep from the pia. Prior to injecting tracers into the Pons, SC, Pom, and VPM the head of the rat was leveled with a precision of 1 µm in both the medial–lateral and anterior–posterior planes using an electronic leveling device (eLeVeLeR; Sigmann Elektronics, Hüffenhardt, Germany) mounted to an adapter for the Kopf stereotax. The distance of the two aluminum probes of the leveling piece was adjusted to the distance of bregma and lambda. The probes were lowered onto the skull and placed on the markings for bregma and lambda. The tilt

of the rats head was then adjusted until both sensors showed the same relative distance. The leveler was raised so the probes were no longer touching the skull, the leveler was turned 90° and the probes were lowered back to the surface of the skull. The same procedure was then repeated to adjust the coronal tilt. Injections into Sp5C of the left side of the brain stem were performed through the atlanto-occipital foramen, 3.0 mm from the midline, 1.4 mm depth at the obex level. Monosynaptic neuronal tracers were pressure injected (50–200 nL) under visual control using a 30cc syringe coupled to a calibrated glass injection capillary. After injection of tracers, the incision site was thoroughly cleaned with saline and sutured closed. 12 rats were single injected with the retrograde tracer Fluorogold (Fluorchrome, 3% in distilled water) into one of the flowing four targets: Pom, SP5C, SC, or Pons for anatomical analysis only. Injections into multiple targets of the same animal were performed using combinations of three retrograde tracers: FG (Fluorochrome; 3% in distilled water), CTB-594 and CTB-647 (Molecular Probes; 1 mg/ml in PBS). In 30 (FG: 3/CTB-594: 19/CTB-647: 8), 24 (23/1/0), 17 (4/7/6), and 23 (1/4/17) of the triple injected animals, injections were targeted at the Pom, SC, Pons, or Sp5C, respectively. These rats were used for both anatomical and physiological analysis. 48 rats were also single injected with the anterograde virus tracer rAAV-2/1-CAG-hChR2(H134R)-Syn-mCherry (titer $1x10x^{12}$ gc ml^{-1}) provided by Martin Schwartz (University of Bonn) into the VPM of the left hemisphere. These rats were used for both anatomical and physiological analysis. All rats injected with retrograde tracers underwent a 5-7 day incubation period before either being transcardially perfused or re-anesthetized for in vivo recording experiments. Rats injected with rAAV virus into the VPM underwent

a 16-21 day incubation period before either being perfused transcardially or re-anesthetized for in vivo recording experiments.

2.1.3 Injection of monosynaptic retrograde tracers into single intrinsic whisker muscles

Young adult (P28-35) male Wistar rats were anesthetized with a ketamine-xylazine mixture (70/6 mg/kg, i.p.) and placed in a stereotaxic frame (Helmut Saur Laboratories). The rat's head was rotated 20 degrees upwards in the ventral-dorsal direction to give better visual access to the right whisker pad on the snout. Whiskers targeted for injections were identified visually under a surgical stereoscope (Leica MZ6) and marked at the base of the snout with a surgical pen. The fur surrounding the targeted whisker or whiskers in experiments where multiple whiskers were injected, was trimmed away and a small incision next to the targeted whisker follicle was made. A steel injection needle attached to a 5µm glass Hamilton syringe was inserted into the incision approximately 1mm below the skin of the whisker pad using a manual micromanipulator (Narishige Model BE-8). 500 to 700 nL of cholera toxin beta subunit (CTB) conjugated to AlexaFluor 488, 594, or 647 (Molecular Probes 1mg/ml in PBS) was then pressure injected close to the base of the targeted whisker follicle under visual control. Rats underwent a 6 day survival period after tracer injections then perfused transcardially for anatomical analysis.

2.1.4 Injection of replication competent rabies virus into a single whisker muscle

All experimental procedures were conducted at the University of Pittsburgh and in accordance with National Institutes of Health guidelines and were approved by the relevant Institutional Animal Care and Use and Biosafety Committees. The procedures for handling rabies virus and animals infected with rabies have been described previously [23, 24] and are in accordance with or exceed the recommendations from the Department of Health and Human Services (Biosafety in Microbiological and Biomedical Procedures). Injections of rabies virus were carried out identical to injections of CTB, as described above. 500 to 700nL of the N2c strain of rabies virus (1 × 109 pfu/mL, 0.25-1.0 mL, provided by M. Schnell, Thomas Jefferson University, Philadelphia) was pressure injected at the base of the follicle of the C3 whisker under visual control. Rats underwent survival periods of 3 to 5 days before being perfused transcardially for anatomical analysis.

2.2 In vivo cell attached recordings

In vivo cell-attached recordings and biocytin fillings have been described in detail previously. Briefly, rats triple injected with monosynaptic retrograde tracers or single injected with rAAV were (re-)anesthetized with urethane (1.8 g/kg) by intraperitoneal injection. The depth of anesthesia was assessed by monitoring pinch withdrawal, eyelid reflexes and vibrissae movements. Throughout the experiment, the animal's body temperature was maintained at 36.5±0.5°C by a heating pad. A cranial window with a size of 2 x 2 mm was made 2.1 mm posterior and 5.5 mm lateral to the bregma on the right cerebral hemisphere above vS1. Patch pipettes were prepared from borosilicate glass with a pipette tip diameter of 1 µm (3-5 MΩ) and were filled with normal rat ringer supplemented with 2% biocytin (Sigma: 576-19-2). The pipette was advanced in 1 µm steps to locate single neurons, which was indicated by an increase in electrode resistance (unbiased sampling, irrespective of spiking activity). At this stage, AP waveforms were recorded using an extracellular loose patch amplifier (ELC-01X, npi electronic GmbH) and digitized using a CED power1401 data acquisition board (CED, Cambridge Electronic Design, Cambridge, UK). Subsequently, the pipette was advanced until the resistance was 25-35 MΩ and APs had an amplitude of 3-8 mV. For all tracer injected rats, ongoing and sensory-evoked spiking of each neuron was recorded during 20-30 trials of passive multi-whisker deflections. Specifically, a plastic tube (1 mm tip diameter) was placed at a distance of 8-10 cm from the whisker pad and delivered an air puff (10 PSI), which deflected the principal and all surrounding whiskers along the caudal axis for 700 ms. Stimulation was repeated at constant intervals (0.3 Hz) and occurred randomly with

respect to up- and down-states. For rats injected with rAAV, thalamic evoked spiking was recorded during 30 to 100 trials of photo stimulation by applying 10ms pulses of light (470nm wavelength) at frequencies of 0.4Hz, 2Hz, and 10Hz on the cortical surface in close proximity to the placement of the recording electrode. Photo stimulation occurred randomly with respect to the up-and down-states. Following the recording, juxtasomal biocytin filling for the purpose of labeling cell morphology was performed by applying continuous, low intensity square pulses of positive current (<7 nA, 200 ms on / 200 ms off), while gradually increasing the current in steps of 0.1 nA and monitoring the AP waveform and frequency. The membrane opening was indicated by a sudden increase in AP frequency. Filling sessions were repeated several times (5-10 min) and diffusion was allowed for 1-2 hours to obtain high-quality fillings. Rats were then perfused transcardially for anatomical analysis.

2.3 In vivo optogenetic photo stimulation

Photo stimulation of channel rhodopsin expressing primary thalamic (VPM) boutons was achieved by the following. A 400μm diameter optical fiber (ThorLabs #RJPSF2) coupled to a 470nm wavelength LED source (ThorLabs M470F3) and powered by an LED driver (ThorLabs #DC2200). With a maximum output power of 1000mA of the LED controller, a 10ms pulse of light was measured at the end of the optical fiber using a laser power meter (ThorLabs #PM100A) couple to a photodiode (ThorLabs #S121C). The optical fiber was positioned using a 3 axis motorized micromanipulator (Luigs and Neuman) approximately 1-2mm above the cortical surface so the light beam resulted in a 1-2mm disc of light on the brain surface in close proximity to the recording site. Control of the LED driver was implemented with Spike2 software (CED, Cambridge, UK.).

2.4 Histology

2.4.1 Fixation of brain tissue

Rats were perfused transcardially first with 100mM sodium phosphate buffer (P.B.) (Sigma Alderich (1ml per 1g of body weight pH= 7.2) then approximately with 50-75 ml of 4% paraformaldehyde (Sigma Alderich) in 100mM P.B. pH=7.2 (PFA). Brains were then surgically removed, post fixed in 50ml of 4% PFA overnight at 4^{o}C, then washed 4-5 times in 100mM P.B. For rats that were injected with CTB into whisker muscles, the mystacial pad containing the injected muscles on the rat's snout was surgically removed, placed between two glass microscope slides and also fixed overnight in 4% PFA.

2.4.2 Gelatin embedding of brain tissue

For brains that were sliced in the coronal plane and as well as the mystacial pads, were all embedded in 10% gelatin using the following protocol prior to serial sectioning. The cerebellum and brainstem structures were first dissected from the rest of the brain by slicing with a single edged razor blade in the coronal plane in between the most rostral part of the cerebellum and the most caudal part of the neocortex, taking extra care that little to no damage is done to structures exposed to the cutting edge of the blade. 10% molten gelatin mixture was made by dissolving 10g of gelatin from porcine skin (Sigma Aldrich #G2500) at 50^{o} C in 100mM PB. Brains were placed in a plastic square shaped

mold facing upward and 50° C molten gelatin mixture was slowly in stages (to prevent brains from floating in the gelatin) pipetted into the mold chamber until brains were completely covered. The gelatin was allowed to solidify for approximately 30 minutes at room temperature before cooling the molds for 2 hours at 4° C. Then brain-gelatin blocks were carefully removed from the molds preventing any breaks or tears in the gelatin. Using a single edged razor blade the gelatin was cut away around the brain into the shape of a pyramid. Angled cuts in the top right and bottom left corners from the surface of the gelatin-brain block to the base were made to conserve the orientation of the tissue post slicing. The mystacial pads where removed from the glass slides and placed on their anterior side into a small plastic weighing dish before being covered with molten gelatin mix. The gelatin was allowed to solidify at room temperature and then cooled at 4° C. Both brain gelatin blocks and mystacial pad gelatin blocks were post fixed in 4% PFA overnight at 4° C and washed 4-5 times in 100 mM PB.

2.4.3 Serial sectioning of brain tissue

All brain tissue unless otherwise noted was serially sectioned with a thickness of 50μm either in the coronal plane or in a plane tangential to the cortical surface prior to antibody treatment using a vibrating microtome (Leica VT1200). For experiments where rats were injected with neuronal tracers into subcortical brain structures only and not followed by an electrophysiological recording experiment, brains were serially sectioned in the coronal plane to include only vS1 and the corresponding injection target site(s). For rats that were injected with CTB into individual whisker muscles, only the brain stem was serially sectioned in the coronal plane to include to the facial nucleus. For these whisker injected animals, 300μm thick serial sections of the mystacial pads were also made in the sagittal plane. For rats injected with replication competent rabies virus into a single (C3) whisker muscle, serial sections (approximately 350 – 400 in total) of the entire brain were made, including brainstem and cerebellum. For all rats where electrophysiological recordings were performed, brains were serially sectioned by the following procedure to achieve a slicing plane tangential to the neocortex. The cerebellum and brainstem structures were first removed by the procedure already described above in section 2.2.2. The left and right hemispheres were then separated by making a precise cut down the midline using a single edged razor blade. The recorded hemisphere was glued using cyanoacrylic glue onto a custom built aluminum cutting block down on the medial side of the tissue so that the midline was facing away from the cutting blade with the brain surface facing upward towards the cutting blade. The custom aluminum block was then placed into the custom built buffer chamber and raised at a 45^{o} angle. This cutting angle assured

that slicing was done perpendicular to the cortical columns. 48 serial sections were then made of the neocortex starting from the pia slicing down to the white matter. The remaining unsliced hemisphere was carefully removed from the cutting block taking care to not leave any glue on the tissue and blocked in gelatin using the same procedure as described above in section 2.2.2. The unsliced hemisphere gelatin block was then serial sectioned in the coronal plane to recover the injection site(s). All tissue slices were placed in individual wells (1 slice per well) of 24 well tissue culture plates filled with 100mM P.B. (2-3mL) preserving the exact order they were sliced in and stored at 4^{o}C until immunohistochemical staining procedure.

2.4.4 Immunohistochemical staining

All slices were first washed 3 times in 100mM PB then permeabilized and blocked in 4% normal goat serum (NGS) (Jackson ImmunoResearch Laboratories #005-000-121) in 100mM PB containing 0.5% TritonX-100 (TX) (Sigma Alderich #9002-93-1), 500µL per well, for 2 hours at room temperature. Next tissue slices were treated with primary antibodies diluted (1:500) in 100mM PB containing 1% NGS, 400µL per well, for 24-48hrs at 4^{o}C. All slices were removed of primary antibody solution and washed 3 times in 100mM PB. Slices were then treated with secondary antibodies diluted (1:500) in 100mM PB containing 3% NGS and 0.3% TX for 2-3 hours at room temperature. Slices were removed of secondary antibody solution and washed again 3 times in 100mM PB. For the purpose of counting FG retrogradely labeled neurons with respect to all neurons (NeuN [39]) from the 12 single FG injection experiments the following antibodies were used:

rabbit IgG anti-FG primary antibody (EMD Millipore #AB153), mouse IgG1 anti-NeuN primary antibody (EMD Millipore #MAB377), goat anti-rabbit IgG AlexaFluor 488 secondary antibody (Invitrogen #A11008) and goat anti-mouse IgG1 AlexaFluor 647 secondary antibody (Invitrogen #A21240). In all other experiments where FG was injected in combination with CTB Alexa594 and CTB Alexa647, anti-NeuN/Alexa647 was excluded and AlexaFluor 488 was replaced with AlexaFluor 405 to visualize FG positive neurons. For the purpose of counting rabies retrogradeley labeled neurons with respect to all neurons the following antibodies were used: mouse anti-RABV-P 31G10 (Thomas Jefferson University) primary antibody, rabbit anti-NeuN (EMD Millipore #MAB377) primary antibody, goat anti-mouse IgG AlexaFluor 488 (Invitrogen #A11029) secondary antibody, and goat anti-Rabbit IgG AlexaFluor 647 (Invitrogen #A21245) secondary antibody. For experiments where rAAV was injected into the VPM the following antibodies were used in order to enhance the fluorescence expressed by the virus and to label primary thalamic glutamatergic synapses: rabbit anti-mCherry (Invitrogen #PA534974) primary antibody, mouse anti-VGlut2 (SynapticSystems #135421) primary antibody, goat anti-Rabbit IgG AlexaFluor 647(Invitrogen #A21245) secondary antibody, and goat anti-mouse IgG Alexa 405 (Invitrogen #A31553). For all tangentially sectioned tissue slices that were obtained from tracer injection experiments that were followed by an in vivo recording with biocytin cell filling procedure, were additionally treated with streptavidin conjugated to AlexaFluor 488 for the purpose of visualizing the biocyin filled neuronal structures. First slices were washed 3 times in 100mM PB then treated with streptavidin AlexaFluor488 conjugate (Molecular Probes #S11223) diluted (5mg/ml) in 100mM PB containing 0.3% TX for 3-5 hours at room temperature. Slices were then washed 3 times

in 100mM PB. All tissue slices were embedded with slowfade gold (Invitrogen #S36936) anti-fade protectant mounting medium on glass microscope slides and enclosed with a glass coverslip. The edges of the coverslips were then sealed with clear nail polish to prevent any leakage of the mounting medium and were stored at 4^{o}C.

2.5 Image acquisition

2.5.1 Wide-field fluorescence microscopy

All images as described in this section were acquired using a fluorescence wide-field microscope (BX51, Olympus) equipped with a motorized x,y,z stage and controlled using image acquisition software program Surveyor.

For experiments where electrophysiology with biocytin cell filling occurred, 45-48 consecutive tangentially sliced tissue sections were imaged prior to confocal image acquisition, as follows in order to contour the pia, white matter, and barrels for the purpose of registration of neuron morphologies. Wide-field, single z plane images with a maximum 5x7 fields of view to include the entire tissue section were acquired using a 4x dry objective (Olympus) at resolution of 2.30μm x 2.30μm per pixel and a GFP filter cube (Olympus #MNIBA2).

The injection sites that were targeted with either FG retrograde tracer or rAAV anterograde tracer expressing mCherry were also imaged using a 4x dry objective at

resolution of 2.30μm x 2.30μm per pixel using a U.V. filter cube (Olympus) or RFP filter cube (Olympus) respectively.

For triple CTB injection experiments targeting single whisker muscles, quadruple sequential channel (using GFP for CTB-Alexa488, 560nm for CTB-Alexa594, RFP for CTB-Alexa647 filter cubes, and a blank filter cube–brightfield for delineating the Facial Nucleus) widefield images of 2x2 fields of view of the facial nucleus were acquired using a 10x dry objective (Olympus) at a resolution of 0.926 x 0.926 x0.5 μm per voxel. Sequential channel (using the same filters above) widefield images of 7x9 fields of view of the mystacial pads from these triple whisker injection experiments were acquired using a 4x dry objective at a resolution of 2.3 x 2.3 x0.5μm per voxel.

2.5.2 Confocal laser microscopy

All images described in this section were acquired using a confocal laser scanning system (Leica Application Suite Advanced Fluorescence SP5; Leica Microsystems) equipped with glycerol/oil objectives (HC PL APO 10x .4N.A., HC PL APO 20x .7N.A., and HCX PL APO 63x 1.3N.A.), a tandem scanning system (Resonance Scanner: 8kHz scanning speed), spectral detectors with hybrid technology (GaAsP photocathode; 8x line average) and mosaic scanning software (Matrix Screener, beta version provided by Frank Sieckmann, Leica Microsystems). The following excitation/emission settings were used for all experiments where applicable: AlexaFluor-405 (excitation: 405nm (UV-laser); emission detection range (410-455nm), AlexaFluor-488 (excitation: 488nm (Argon-laser);

emission detection range (495-550nm), AlexaFluor-594 (excitation: 561nm (DPSS-laser); emission detection range (600-630nm), AlexaFluor-647 (excitation 633nm (HeNe-laser); emission detection range (650-785nm).

For imaging of biocytin-streptavidin AlexaFluor488 labeled neuronal structures from the in vivo recording experiments for the purpose of 3D reconstruction of dendrite morphologies, 3D single channel image stacks of up to 0.8mm x 0.8mm x 0.05mm were acquired at a resolution of 0.092 x 0.092 x 0.5µm per voxel, using a 63x glycerol immersion objective, a digital zoom of 2.5, and emission/excitation laser/detector settings for AlexaFluor-488. For experiments where in vivo recordings were done in combination with an rAAV injection into the VPm, laser/detector settings for AlexaFluor-647 were used in combination with AlexaFluor-488 to generate dual channel images containing both neuronal structures labeled by biocytin-streptavidin AlexaFluor 488 and rAAV labeled VPm boutons enhanced with AlexaFluor-647 for identification of putative primary thalamic synapses on the 3D reconstructed dendrite morphologies. For all in vivo recording experiments, image stacks were acquired for maximum of 30 consecutive tissue sections (depending on morphological cell type) in order to cover complete dendrite morphologies.

For FG, CTB-594, CTB-647 triple injection experiments done in combination with an in vivo recording/cell filling the following images were acquired in order to assign a long-range axonal target to the biocytin-streptavidin AlexaFluor 488 labeled L5 pyramidal tract neurons. Sequential channel images of single fields of view were acquired using a 20x glycerol immersion objective at a resolution of 0.361 x 0.361 µm per pixel, a digital zoom of 2.0 and excitation/emission settings for AlexaFluor-405, AlexaFluor-488, AlexaFluor594, and AlexaFluor-647.

For counting of neuron somata in the single Fluorogold injection experiments, dual channel mosaic images of areas up to 7.5 x 10mm were acquired using a 10x glycerol immersion objective at a resolution of 0.868 x 0.868 per pixel, a digital zoom of 1.7 and excitation/emission settings for AlexaFluor-488 and AlexaFluor-647.

For counting of neuron somata in the experiments where replication competent rabies virus was injected into a single (C2) whisker muscle, dual channel mosaic images of areas of up to 14 x 20mm (in order to cover the entire tissue slice) were acquired using a 10x glycerol immersion objective at a resolution of 0.868 x 0.868 per pixel, a digital zoom of 1.7 and excitation/emission settings for AlexaFluor-488 and AlexaFluor-647.

2.5.3 Super resolution confocal laser microscopy

For validation of putative TC synapses and rAAV efficiency image stacks were acquired with a super-resolution enhanced laser scanning system (Leica Application Suite Advanced Lightening Fluorescence SP8; Leica Microsystems) equipped with glycerol/oil immersion objectives (HC PL APO 10x 0.4 N.A., HC PL APO 20x 0.7 N.A., and HCX PL APO 63x 1.3 N.A.), a tandem scanning system (Resonance Scanner: 8kHz scanning speed), spectral detectors with hybrid technology (GaAsP photocathode; 8x line average): VGlut2 AlexaFluor-405 (excitation: 405nm (UV-diode laser); emission detection range (410-455nm), biocytin-streptavidin AlexaFluor-488 (excitation: 488nm (Argon-laser); emission detection range (500-550nm), rAAV-AlexaFluor-647 (excitation: 647nm (White Light Laser); emission detection range (650-785nm). Sequential triple-channel image stacks of representative parts of the basal/apical dendrite of all reconstructed

L5PTs in L5, L4, and L2/3 were acquired at a resolution of 29.5 x 29.5 x 130 nm per voxel (i.e. as determined by the default settings of the lightening suite).

2.6 Reconstruction of dendrites/assignment to morphological cell types

Three-dimensional reconstruction of dendrite morphologies acquired from the in vivo recording/cell filling experiments was based on a previously described method for semi-automated reconstruction of neuron morphology from brightfield microscope images [40]. Here, the tracing software was adapted to the 3D confocal image stacks acquired by the method described above in section 2.3.2. The 3D confocal image stacks were deconvolved using linear Tikhonov-Miller algorithm and theoretically computed point spread function of the confocal microscope[41] using Huygens software (SVI, the Netherlands). Neuronal structures were automatically detected in the image stacks using custom-designed software [40]. Proof editing of the automated tracing results, as well as alignment and splicing of neuronal branches across consecutive histological slices was done using the FilamentEditor [42]. Three-dimensional dendrite reconstructions were augmented with contours of anatomical reference structures (pia surface, white matter tract, and L4 barrels), which were drawn manually from the 4x overview images acquired using the method described above in section 2.3.1. Next using the reconstructions of these anatomical reference structures, all reconstructed dendrite morphologies acquired from the in vivo recording experiments were registered to a standardized 3D reference

frame of vS1 (ref). The shortest distance to the pia surface to the soma location, as well as 20 morphological and topological features that have been previously shown to separate between morphological excitatory neuron types in rat vS1 were calculated for each reconstructed and registered dendrite morphology.

2.7 Identification and validation of rAAV labeled VPM putative synapses

Dual channel image stacks (rAAV-AlexaFluor647 and biocytin-streptavidin-AlexaFluor488) were loaded into Amira visualization software (FEI) and aligned to the reconstructed dendrites (described above) corresponding to each imaged tissue section. All reconstructed dendrites acquired from the rAAV-VPM injection experiments were manually inspected, and landmarks were placed onto each spine head that was overlapping with a VPM bouton to mark as a putative synapse.

For validation of putative VPM synapses, super resolution confocal image stacks that were acquired as described above in section 2.3.3 were loaded into Amira visualization software and manually inspected for overlap within a single optical section between spine heads and rAAV/VGlut2-postive VPM boutons. The efficiency of the rAAV injection method was also calculated by quantifying the rAAV/VGlut2 overlap not only across experiments but also across different layers of the cortex within each experiment. To do so the percentage of rAAV labeled VPM boutons that co-localized with VGlut2 labeled vesicle pools as well as the percentage of rAAV boutons that were counted that did not

co-localize with VGlut2 labeled vesicle pools (i.e. rAAV false positives) from representative sample areas in layer 5, layer 4, and layer 2/3 were measured for each rAAV-VPM injection experiment where a dendrite morphology of a L5PT was reconstructed.

2.8 Detection of somata

For experiments where retrograde tracer agents were either single or triple injected into subcortical brain structures, retrogradely labeled neurons were detected manually from 2D confocal images described in 2.3.2 using Amira Software [43]. For triple tracer injection experiments, retrogradely labeled neurons were marked in each image channel (i.e. AlexaFluor-405, AlexaFluor-594, AlexaFluor-647) separately. Double and triple-labeled neurons were determined as those that were marked in two and three channels, respectively. NeuN-labeled somata were detected automatically using previously reported custom-designed software [44]. Images form coronal slices were aligned such that the vertical cortical axes were parallel before marking soma locations. Soma distributions from each slice were then converted into 1D density profiles along the vertical cortical axis by summing all somata in 50 µm intervals. One-dimensional profiles were aligned vertically using the L4 peak of the NeuN profiles in each respective slice, and the aligned 1D NeuN, as well as FG profiles were averaged for each of the four targets. To estimate the total number of retrogradely labeled somata per average barrel column, the present NeuN profile was aligned and uniformly scaled to match the 1D profile

of the 3D density of NeuN-positive somata determined previously [45]. The scaling factor was determined by minimizing the squared error between the respective NeuN profiles. The 1D profiles of FG-positive somata were scaled accordingly.

For experiments where retrograde tracers were triple injected into whisker muscles retrogradley labeled somata were detected manually using Amira Software in 2D.

2.9 Physiological analysis

Ongoing and stimulus-evoked spiking was recorded with Spike-2 software (CED, Cambridge). Spiking profiles during periods of ongoing activity, whisker stimulation, and photo stimulation were calculated offline by Spike-2 software, custom written Matlab routines provided by Robert Egger (Max Planck Institute for Biological Cybernetics) or custom written Python routines provided by Arco Bast (Max Planck Group In Silico Brain Science, Center of Advanced European Studies and Research). To determine ongoing activity, spontaneous occurring spikes were detected during 200ms before stimulating the whiskers. Ongoing and sensory evoked spikes by whisker stimulation were measured for 30 air puff trials and the resultant post time stimulus histograms (PTSH) were analyzed at a temporal resolution of 5ms bins. For relationships between functional properties and long-range axonal targets of L5PTs, similarity between sensory-evoked responses was calculated as follows: First ongoing spike rates were subtracted from each 5ms bin of the four target related averages PSTHs and PSTHs of each individual L5PT. If subtraction of ongoing spiking resulted in negative values, the respective bins were set to zero. Second,

each resultant PSTH of sensory-evoked spiking was then normalized to the respective bin with maximal spike rates. Third, for each L5PT, the bin-wise absolute difference between its normalized sensory evoked PSTH and each of the four target-related PSTHs was calculated. Fourth, The bin-wise differences were summed across the entire recording period (-200 to 1100ms post stimulus). This sum was defined as the similarity between PSTHs (i.e., the smaller the similarity value, the more similar the PSTHs). The four similarity values of each PT were combined as two similarity indices:

$\frac{\text{Similarity}_{\text{to Pons}} - \text{Similarity}_{\text{to SC}}}{\text{Similarity}_{\text{to SC}} + \text{Similarity}_{\text{to Pons}}}$ (x-axis); $\frac{\text{Similarity}_{\text{to Sp5C}} - \text{Similarity}_{\text{to POm}}}{\text{Similarity}_{\text{to Pom}} + \text{Similarity}_{\text{to SP5C}}}$ (y-axis).

Analysis of post synaptic action potential activity in response to photo stimulation of primary TC synapses was done as follows: First, onset responses to photo stimulation were determined by measuring the action potential (AP) activity during the first 20ms post stimulation across all trials. There were three different responses to photo stimulation that were observed; neurons either responded with a single AP, a burst of 2 APs, or a burst of 3 or more APs (Note bursts were defined as 2 or more action potentials occurring at a rate of more than 100Hz as previously reported [46]). These three types of observed AP responses were then defined as an onset event and onset event probabilities for each recorded neuron were calculated by dividing the number of observed AP events by the total number of trials for each respective photo stimulation protocol. Light was pulsed for 10ms at frequencies of 0.4Hz, 1.96Hz, and 9.09Hz sequentially for trials of 30, 50, and 100 respectively for each pulse frequency. For every onset event that was observed the number of singe AP, double A.P. bursts and ≥ triple AP bursts for each neuron was determined and the probability of observing one of the three events for each type of photo

stimulation protocol was determined by dividing the number of observed events by the total number of trials. Finally, for all neurons that had an onset response event, onset latencies were determined for each photo stimulation protocol where an onset event had occurred. This was done by determining the time post stimulus an action potential occurred for each trial and averaging these post stimulus times across all trials.

2.10 Statistical Analysis

All statistical analysis was done using either Microsoft Excel, Igor (Wavemetrics) or GraphPad. All results are presented as the mean ± standard error of the mean, unless otherwise noted.

Chapter 3

Method Results

Several in vivo anatomical and physiological experiments in young adult rats have been described so far in the previous chapter. First, for the purpose of quantifying the primary thalamic synaptic input patterns of excitatory neurons, pre and post synaptic structures were identified by labeling the axonal terminal boutons of neurons located in the VPM and the dendrites of individually recorded neurons in the vibrissal part of the primary somatosensory cortex (vS1). Dendrites of single neurons were labeled by biocytin filling during cell attached recordings and primary TC synaptic terminals (boutons) were selectively labeled by adeno-associated virus injections into the VPM. The virus expressed both a fluorescent marker and channel rhodopsin which allowed for measuring the postsynaptic responses to light stimulated primary TC input. Next monosynaptic retrograde tracers were injected into multiple subcortical brain areas in order to identify populations of PTs in layer 5 of vS1 according to their long-range axonal targets. Combining these injection experiments with cell attached recordings provided in vivo access to the electrophysiology and morphology of PTs whose long-range axonal targets could be identified. In the last set of experiments it was asked whether PTs may

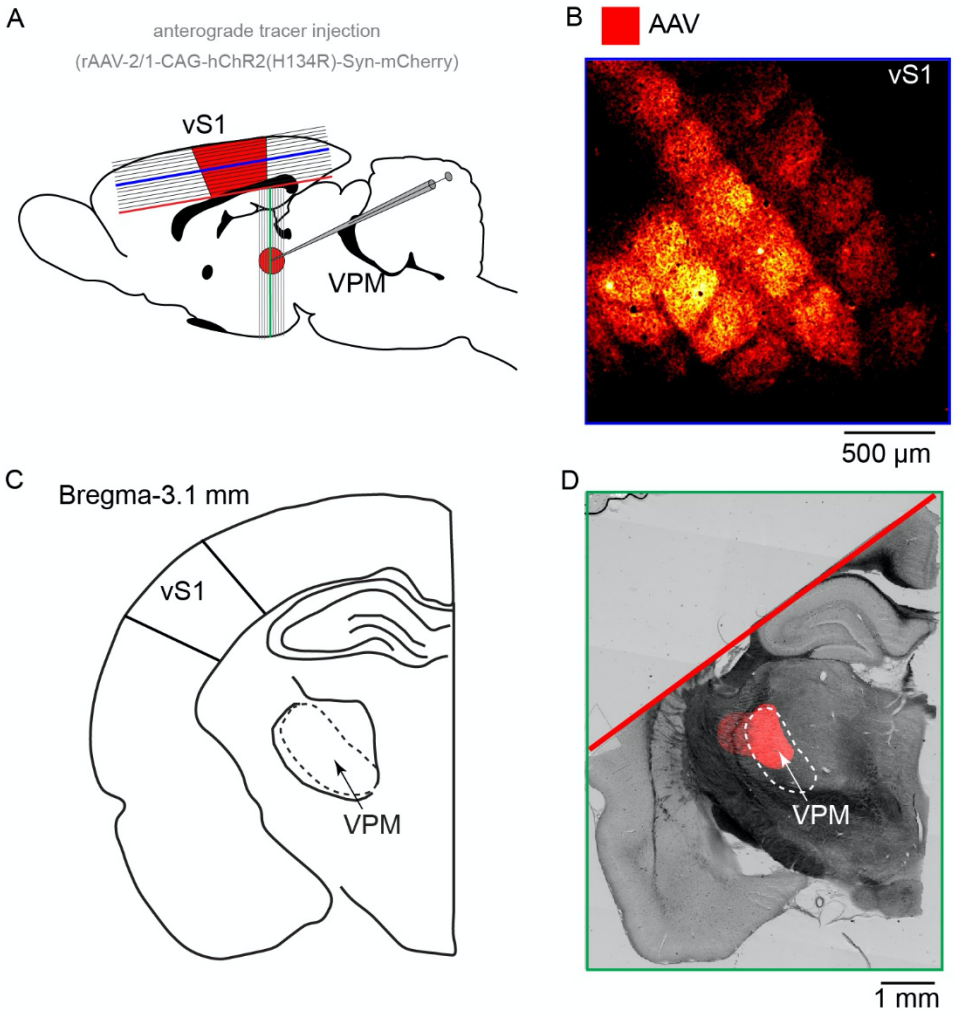

Figure 3.1: Injection of AAV into VPM. (A) Schematic of a virus injection experiment into VPM, cortex was cut tangentially for dendrite reconstruction and synapse mapping, the remaining brain tissue was cut coronally to recover the injection site. (B) Exemplary example image of barrel specific labeling in layer 4 of vS1, this image corresponds to the injection site image shown in D. (C) Representative coronal diagram from the Paxinos atlas showing the location of VPM. (D) Injection site illustrating AAV expression is locally confined to the VPM. Image is scaled to the diagram shown in C.

be embedded into long-range target specific subnetworks and if so which of these subnetworks could be involved in sensory-motor whisker control. Therefore in a purely anatomical study, trans-synaptic tracer agents were injected into single intrinsic whisker muscles to investigate the structural organization of brain-wide whisker related networks.

The results of these experiments yielded many significant biological findings that will be described in detail in the next chapter. However, these finding are largely the result of using different experimental techniques as well as different types of neuronal tracers that will have a large impact on how the data should be analyzed and also interpreted. Therefore the experimental methods themselves as well as the results of these methods require validation. In this chapter I will now present the methodological results as well as controls used to validate the methods used in this thesis.

3.1 Virus mediated thalamo-cortical input mapping

3.1.1 Quantification of rAAV injections

In the first set of experiments I adapted a high-throughput method previously used for mapping TC inputs onto the dendrites of L4 excitatory neurons [47]. rAAV injections, cell attached recordings/optogenetic photo stimulation with dendritic reconstructions were combined to quantify the distribution of TC inputs onto the full dendritic arbors of L5PTs. A total of 48 rats were first injected with adeno-associated virus expressing synapsin-mCherry fusion protein and channel rhodopsin (H134R) into the VPM of the left

hemisphere (Figure 3.1A). After a 17-24 day incubation period rats were then re-anesthetized for cell attached recording/photo stimulation experiments followed by histological procedures (see methods 2.2). Of the 48 rats injected with rAAV into the VPM, post hoc analysis revealed 36 of the rats expressed the barrel specific labeling expected by fluorescently labeling primary TC presynaptic terminals [16] (Figure 3.1B), were designated as being successfully injected and were used for further analysis. Out of these 36 successfully injected rats, 65 morphological identifiable neurons were recovered from the in vivo recording/photo stimulation experiments. Of these 65 cell morphologies 25 were classified as L5PTs, 5 were classified as L5 slender tufted (L4ST), 4 - L4 spiny stellate (L4spiny), and 6 - L6 cortical-cortical (L6CC) according to soma depth, dendrite morphology and or by previous classification methods [17]. Also, 22 neurons were classified as interneurons by small soma size, lack of spines on their dendrites and the presence of dendritic swellings. For the purpose of this thesis, 10 L5PTs, 1 L6CC, 1 L4spiny and 1 L5ST had their complete dendrite morphologies reconstructed and primary TC input distribution mapped from 11 different successfully injected rats. The dendrites of a single layer 4 interneuron was also reconstructed (reconstruction provided by Fernando Messore, Max Planck Group In Silico Brain Sciences, Center of Advanced European Studies and Research). All 65 neurons were used for physiological analysis. These results will be discussed in the next chapter.

By using this injection method it allowed for the selective fluorescent labeling of primary TC synapses within vS1 [16]. However, this means that the results are completely dependent on both the efficiency of the virus (i.e. how many primary TC synapses actually

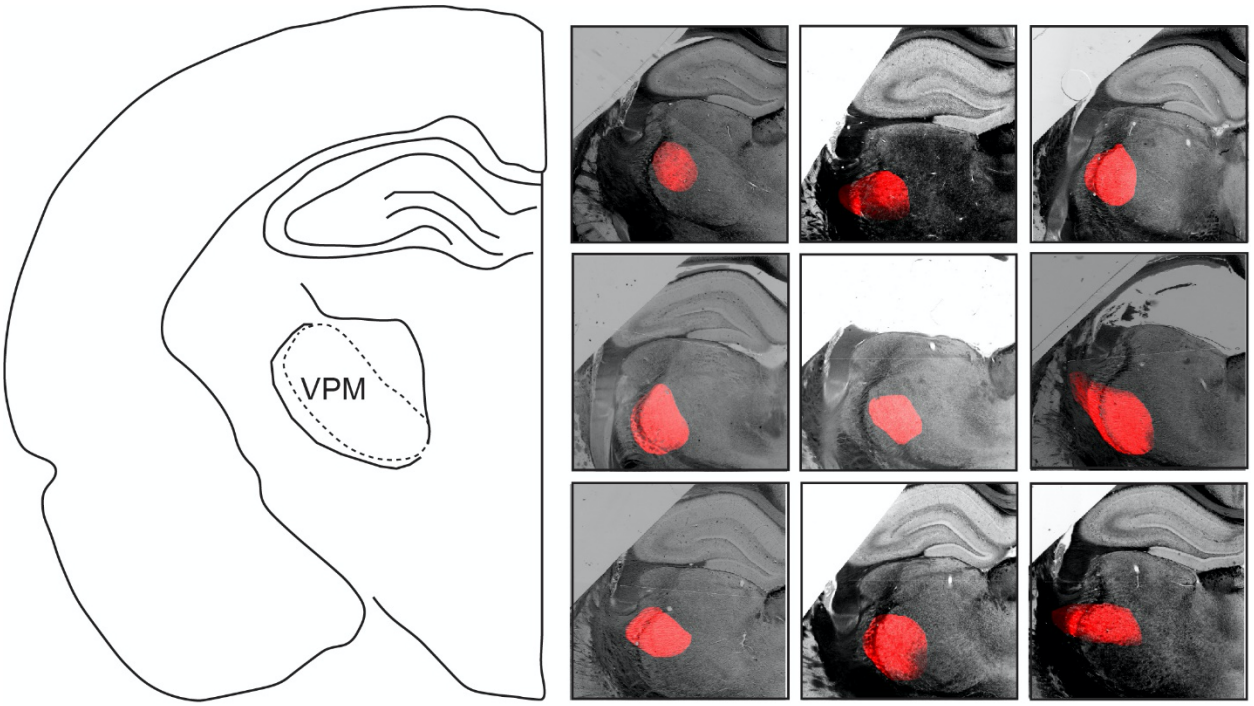

Figure 3.2: VPM injection site verification Center locations of rAAV injections targeting the VPM in the left hemisphere from nine experiments where ten L5PT neurons were recovered (shown in Figure 4.7 & 4.8). Images were aligned to the Paxions atlas (left) to illustrate rAAV injection volume is confined within the VPM borders and did not spread into the higher order thalamus Pom. Fluorescent channel was merged with the respective bright-field channel to delineate the outlines of brain structures.

expressed the virally encoded proteins) and how accurately the VPM was targeted from experiment to experiment (i.e. did the virus stay locally confined to the injection target?). Keeping the injection volume locally confined to the target (VPM) is equally if not more important since higher order thalamus (Pom) also projects to vS1 [16] and could result in falsely identifying higher order TC inputs as primary TC inputs. Therefore, rAAV injection experiments (n = 9) were validated for both injection accuracy and efficiency by the following:

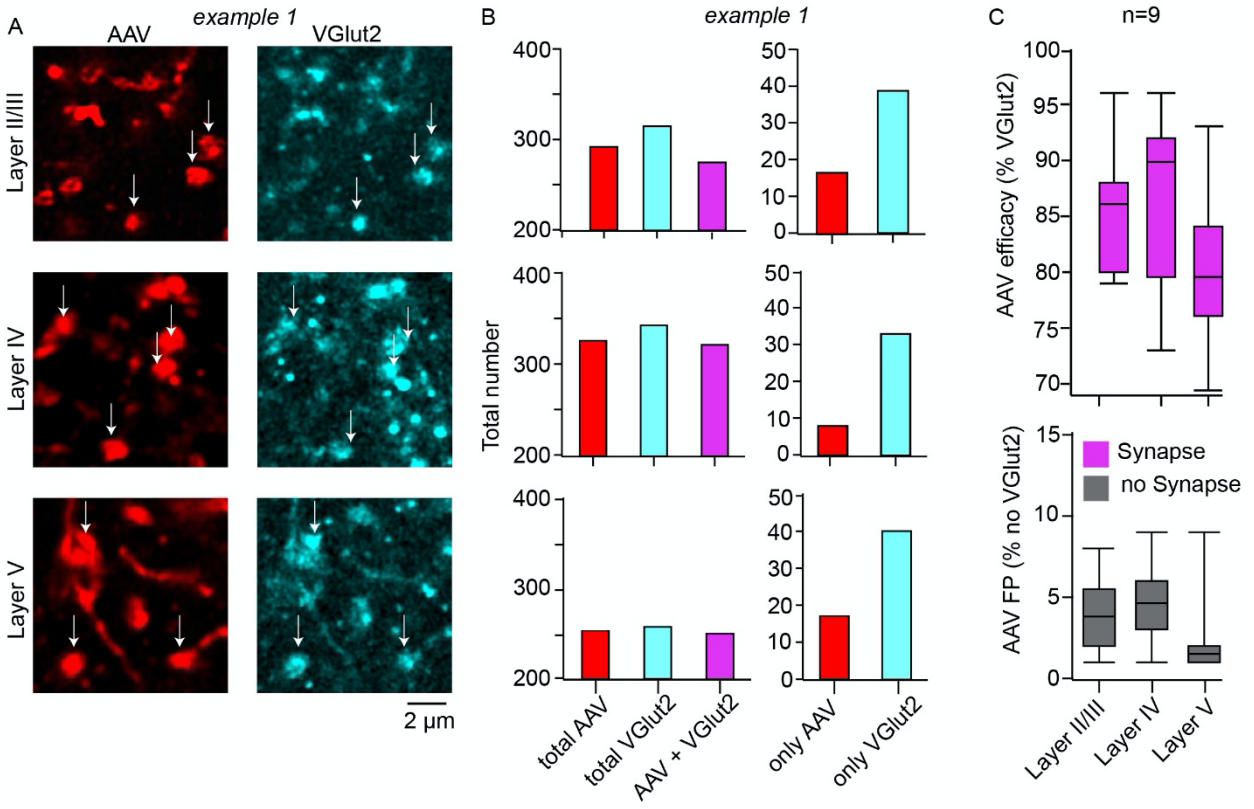

Figure 3.3: rAAV injection into VPM selectively labels primary TC inputs in vS1. (A) Exemplary super resolution images of layer 2/3, layer 4, and layer 5 in neocortex from the same experiment shown in figure 3.1. Right panels illustrate selectively labeled primary thalamic terminals (boutons) by rAAV injection into the VPM (red) and left panel illustrates vesicular glutamate transporter 2 labeling by treatment with VGlut2 antibody (cyan). (B) Total counts from all super resolution images of the experiment shown in panel A. All rAVV labeled boutons, all VGlut2 vesicle pools, and rAAV boutons that co-localized with VGlut2 were counted in representative super resolution images in L2/3, L4 and layer 5 for 9 different injection experiments to estimate both the rAAV labeling efficiency and number of falsely labeled or identified (i.e. false positives) primary TC boutons. (C) Box plots illustrating rAAV efficiency and rAAV false postives for 9 experiments for layer 2/3, layer 4, and layer 5.

After the cortex of was sectioned tangentially, the remaining part of the brain tissue was sectioned coronally to recover the injection sites (Figure 3.1A, D). Low resolution images were made of the tissue sections within the location of the injection target (Figure

3.1D, Figure 3.2). These images were then aligned with corresponding coronal diagrams from the Paxinos Rat Brain Atlas [48] in order to assess whether the injection volume was confined to the VPM or spread into the Pom (Figure 3.1C, D; Figure 3.2). For the 9 injection experiments validated by this method the injection volume remained confined to the VPM without spreading to the Pom (Figure 3.2).

Since this was at most a qualitative assessment of virus injection accuracy, it was important to perform a validation analysis in order to quantify the virus efficiency and selectivity. Therefore, representative tissue sections from layer 5, 4, and 2/3 were also treated with the vesicular glutamate transporter 2 (VGlut2) antibody to immuno-label primary thalamic but not secondary nor cortical synapses [49], [50] (see methods). Additional immuno-labeling of primary TC synapses, allowed for both quantifying the number of TC boutons labeled by the virus and the number of falsely identified virus labeled TC boutons. All positively identified virus labeled boutons should also be co-localized with VGlut2 immuno-labeled vesical pools. Therefore dual channel super-resolution confocal microscopic images were generated from select tangential tissue sections additionally stained with VGlut2 antibody. Individual image channels representing virus labeled primary TC terminals and VGlut2 immuno-labeled primary TC synapses were loaded into Amira visualization software and landmarks were placed on fluorescently labeled structures (i.e. rAAV labeled boutons or VGlut2 vesicle pools) on sample image volumes of 6.2μm^3 (Figure 3.3). The efficiency of the virus labeling was determined by calculating the percentage of rAAV labeled TC boutons that co-localized with a VGlut2 labeled vesicles from the total number of VGlut2 labeled vesicles counted. The percentage of

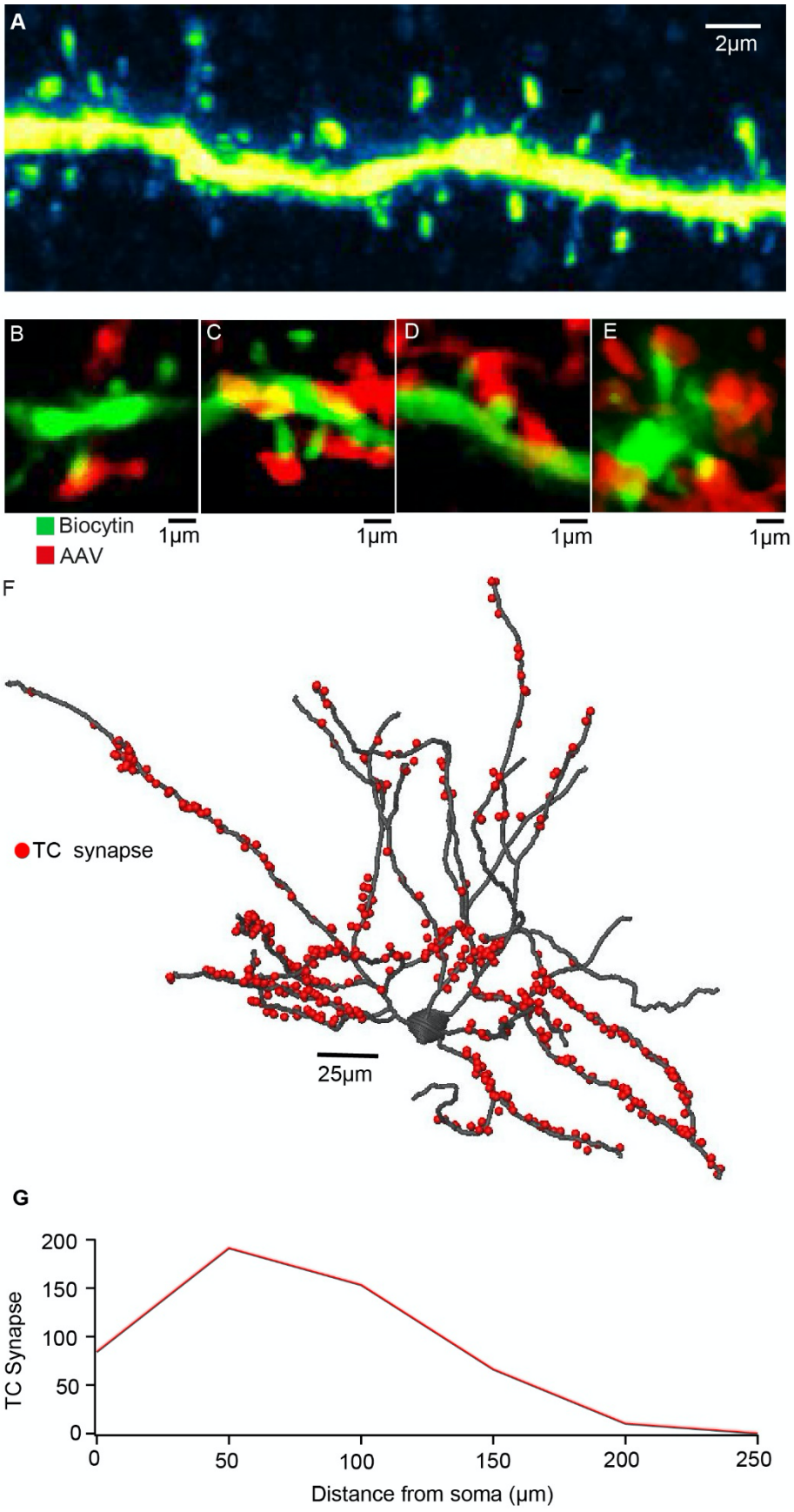
A
2μm
B
C
D
E
Biocytin
AAV
1μm
1μm
1μm
1μm
F
TC synapse
25μm
G
TC Synapse
200
150
100
50
0
0
50
100
150
200
250
Distance from soma (μm)

Figure 3.4 (*previous page*): Primary TC input mapping of L4 Spiny Stellate. (A) Exemplary image of a dendrite branch from an in vivo recorded and biocytin filled L4 spiny stellate to illustrate spine quality labeling. (B-E) Exemplary images to illustrate putative primary TC synapses defined as overlap between a biocytin labeled spine head and a selectively labeled rAAV VPM bouton. (F) Putative primary TC synapse distribution along the dendrites of a reconstructed layer 4 spiny stellate. Red spheres represent spine locations along the dendrite that overlapped with a rAAV labeled VPM bouton. (G) Histogram of TC synapse distribution with respect to distance to the soma from panel F (bin size is 50μm).

rAAV labeled TC terminals that were identified but did not co-localize with VGlut2 were designated at false-positives (Figure 3.3). This was not only calculated across experiments but also across cortical layers within each experiment. It was found that across all experiments in general the virus had a mean efficiency of 85 ± 1.14% (range: 77% - 96%, *N* = 9) The mean labeling efficiency in layer 2/3 was found to be 86 ± 1.67%, $1^{st}/3^{rd}$ quartile: 84% - 87% , *N* = 9). For layer 4 the mean virus labeling efficiency was found to be 88 ± 2.02%, $1^{st}/3^{rd}$ quartile: 77% - 92%. Finally similarly to layer 2/3 and layer 4 the mean virus labeling efficiency in layer 5 was found to be 82 ± 1.98%, $1^{st}/3^{rd}$ quartile: 77% - 86% (Figure 3.3). For the number of falsely identified virus labeled TC terminals, the mean percentage across all experiments was found to be 4 ± 0.54%. The mean percentage of false positives in layer 2/3 was found to be 5 ± 1%, $1^{st}/3^{rd}$ quartile: 2% - 6%, *N* = 9). For layer 4 the mean percentage of false positives was found to be 5 ± 0.85%, $1^{st}/3^{rd}$ quartile: 3% - 6%. Finally similarly to layer 2/3 and layer 4 the mean percentage of false positives in layer 5 was found to be 2 ± 0.86%, $1^{st}/3^{rd}$ quartile: 1% - 2% (Figure 3.3). Because the average labeling efficiency was determined to be 85% and the average number of false positives was determined to be only 4% then the putative TC synaptic

densities reported in this thesis should be an underestimation. This control validation therefore provides empirical evidence that injection of rAAV into the VPM is a reliable and consistent method to selectively label primary TC synaptic terminals of rat vS1.

Finally to illustrate the reliability and reproducibility of this method for mapping primary TC inputs before using this method on the full dendritic arbors of L5PTs, I quantified the primary TC inputs on the dendrites of a fully reconstructed layer 4 spiny stellate neuron (Figure 3.4). As stated above 4 neurons recovered from these VPM injection experiments were morphologically classified as layer 4 spiny stellates. VPM input maps of layer 4 spiny stellates using light microscopy has been previously reported [47]. In the study by Schoonover et al. 2014 [47], the authors used high resolution confocal light microscopy to map putative primary TC synapses on the spines of in vivo recorded layer 4 spiny stellates. They reimaged a subset of these putatively designated primary TC synapses with an electron microscope to confirm whether they contained the "basic ultrastructural features of true synapses." The authors reported that 87.5% of their putatively designated primary TC synapses by light microscopy were true synapses and concluded this method to be a reliable strategy to map virus labeled primary TC inputs onto the dendrites of excitatory neurons. I therefore repeated, for one of the layer 4 spiny stellates recovered from my experiments, the light microscopy method for putatively designating primary thalamic synapses reported in Schoonover et al. 2014 [47]. I first imaged both the dendrites and virus labeled primary TC axonal boutons on a laser confocal microscope with a high magnification objective (See methods 2.5.2). I first counted all the dendritic spines from the individual single channel image planes by placing landmarks on each spine using Amira visualization software. Next, using the individual

dual channel image planes, I counted all the putative primary TC synapses by placing landmarks on locations where a virus labeled axonal bouton overlapped with a biocytin labeled dendritic spine head. The counts resulted in a total of 3095 dendritic spines, of which 16% were designated as putative primary TC synapses (Figure 3.4). Taking in account with measured estimates of primary TC synapse false positives, these results are determined to be in agreement with previous reports [47].

3.1.2 Optogenetic activation of primary thalamo-cortical synapses in vS1

I have shown that AAV injections into the VPM have reliably and efficiently labeled primary TC terminals in vS1. In addition to a fluorescent marker the primary TC terminals also expressed channel rhodopsin (H124R), a light gated ion channel. This allowed for recording the action potential activity of neurons in vivo in response to optogenetic light stimulated primary TC synapses. It has been previously reported that L5 PTs receive monosynaptic connections and can be activated by neurons in the VPM [32]. In the study by Constantinople and Bruno 2013, the authors used whole cell paired recordings of L5 PTs and VPM neurons to measure post synaptic potentials in response to whisker stimulations. They reported that neurons located near the layer 5/6 border which included L5PTs had similar response latencies to whisker stimulation as neurons in layer 4 that are known to receive direct connections from VPM neurons. I however, sought to measure action potential activity during cell attached recordings of L5 PTs in response to

direct light stimulation of primary TC synapses in vS1. Optogenetically activating a subpopulation of presynaptic inputs while recording from their potential post synaptic neuronal targets poses some challenges. Therefore proper control experiments must be carried out in order for accurate analysis and interpretation of the data that is yielded. I first systematically measured the output power at the end of the optical fiber in order to generate a calibration curve. This determined the driver output power and stimulus width necessary to achieve a certain wattage at the end of the optical fiber. I then used local field potential measurements while recording in the deep layers of vS1 to determine if the photo stimulation method was sufficient to activate neuronal populations throughout the depth of the cortex.

Calibration of light stimulus.

The optogenetic photo stimulation setup used to record action potential responses to light activated primary TC synapses consisted of a 400µm optical fiber coupled to a 470nm LED source. The LED source was powered by a driver that was integrated into the analogue digital converter of the recording setup. The light stimulus duration, frequency, and start/stop time were controlled using Spike2 which aligned the light stimulus to the recorded spike times. It has been previously reported that 1mW of output power at the end of an optical fiber was sufficient to activate ChR2 positive neurons in layer 5B of mouse cortex [51]. In order to determine the appropriate light stimulus parameters to achieve 1mW of output power at the end of the optical fiber, I systematically made power measurements using combinations of light pulse widths versus increasing

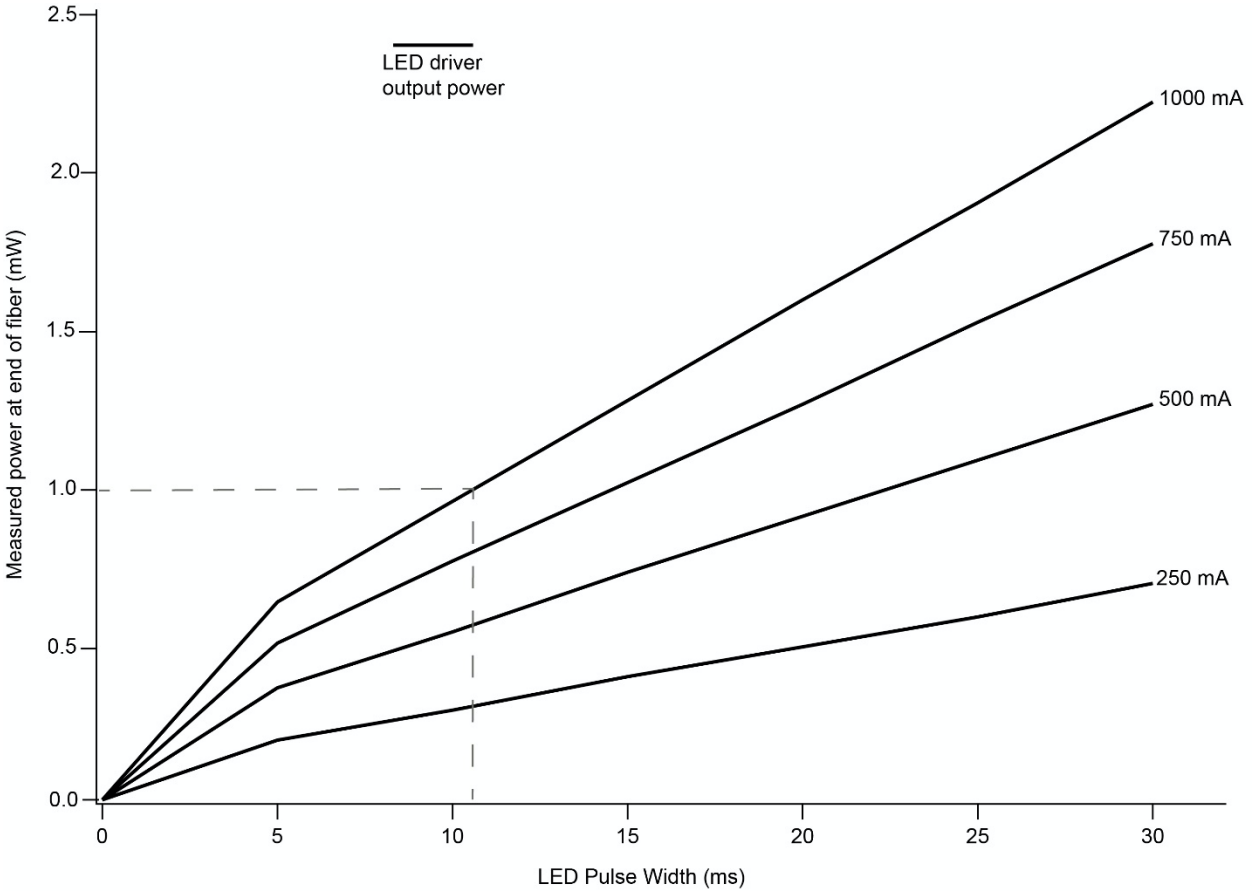

Figure 3.5 Calibration of LED photo stimulation: Calibration curve illustrating fiber optic output power resulting in systematic increases in LED driver power and LED pulse width. At maximum LED driver power of 1000mA, 10ms was the shortest pulse width that achieved a maximum fiber optic output power of 1mW.

changes in amperage of the LED driver. Using a photodiode attached to a power meter I measured the output wattage at the end of the optical fiber. I systematically increased the power settings of the LED driver in 25% increments while changing the pulse width of the light stimulus by 5ms respectively. With these measurements I then calculated a calibration curve and determined the appropriate LED power and stimulus duration to achieve 1mW of output power at the end of the optical fiber (Figure 3.5). I determined that

1000mA of LED driver power with a light pulse width of 10ms was sufficient to achieve a consistent maximum output power of 1mW at the end of the optical fiber.

Optogenetic activation of primary TC inputs in vS1

In the previous section I reported the LED power and light pulse width settings to achieve the optical fiber output power sufficient to optogenetically activate individual neurons as previously reported. It was now necessary to determine if the output power was sufficient to optogenetically activate primary TC inputs in the deep layers with pulsed light onto the cortical surface. I therefore used a local field potential (LFP) guided approach which has been previously reported as a reliable method for precise targeting of cortical columns within vS1 in mice [52] to test whether optogenetic activation was possible in the deep layers. LFPs are measured extracellularly at low frequencies that represent the overall activity of neurons in close proximity to the recording electrode [53]. Electrophysiological recordings in rat vS1 has one major advantage in that a large population of neurons across all cortical layers of vS1 not only increase their action potential firing rates but also have sharp onset responses to whisker stimulation [54]. The TC evoked neuronal activity from a whisker deflection is represented by a sharp depolarization in the LFP (Figure 3.6A). It is then possible to use LFP recordings from whisker deflections as a reference signal in comparison to LFP recordings from light stimulated primary TC synapses since light stimulated TC synapses should evoke a similar LFP signal. I therefore compared LFPs from both whisker stimulation and light stimulation recorded from the same pipet, located near the layer 5/6 border approximately 1350μm below the pia surface. I was able to generate a light evoked sharp depolarization

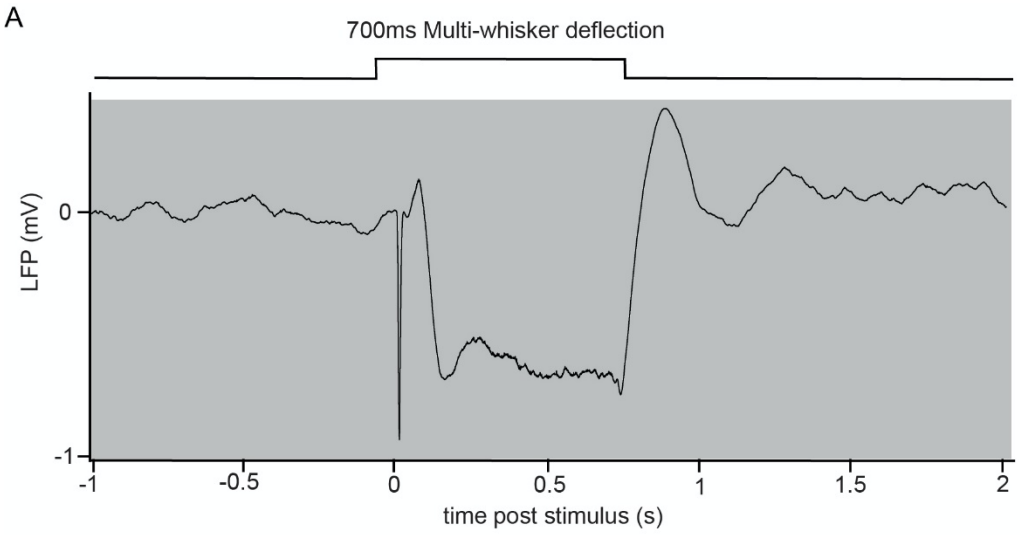
A
700ms Multi-whisker deflection
LFP (mV)
0
-1
-1
-0.5
0
0.5
1
1.5
2
time post stimulus (s)

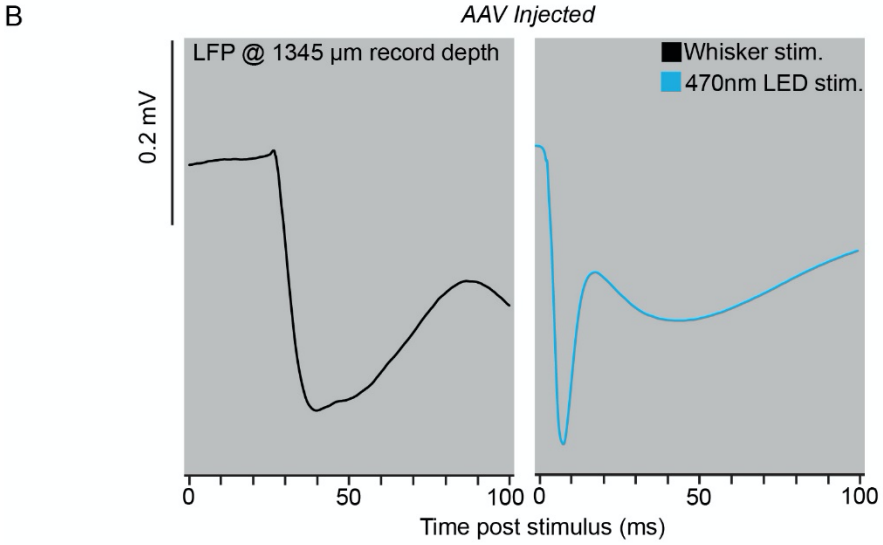
B
AAV Injected
LFP @ 1345 µm record depth
Whisker stim.
470nm LED stim.
0.2 mV
0
50
100
0
50
100
Time post stimulus (ms)

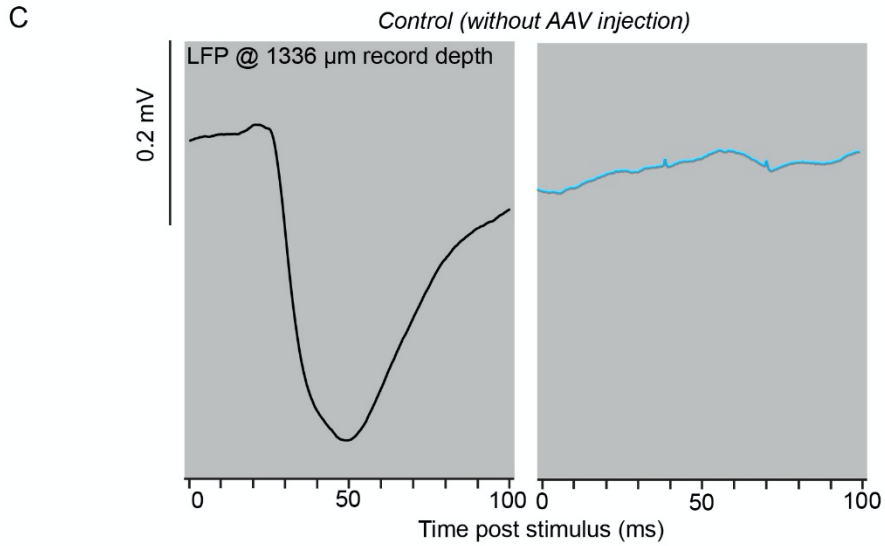
C
Control (without AAV injection)
LFP @ 1336 µm record depth
0.2 mV
0
50
100
0
50
100
Time post stimulus (ms)

Figure 3.6 (*previous page*): Optogenetic activation of primary TC inputs in vS1. (A) Example three second LFP recording window during a 700ms multi-whisker air puff stimulus illustrating the sharp depolarization in the recording trace at the onset of the stimulus. (B) Left panel example 100ms recording window during multi-whisker air puff stimulus and right panel same experiment as shown in left panel of 100ms recording window of 10ms LED stimulus at a recording depth of 1345 μm (layer 6) below the pia surface from an animal injected with rAAV expressing channel rhodopsin into VPM. Note: 10ms LED stimulus evokes similar depolarization in LFP as multi-whisker stimulation. (C) Same as panel B but for non-injected animal (no channel rhodopsin present in primary TC synapses) to illustrate that LFP depolarization shown above in B is from light activation of primary TC synapses and a stimulus artifact.

similar to the depolarization generated upon whisker deflection (Figure 3.6B). This confirmed both that a 10ms width light pulse generating 1 mW of power at the end of the optical fiber positioned just above the cortical surface proximal to the recording electrode was sufficient to evoke neuronal activity in the deep layers of the cortex. Since the optical fiber was positioned just proximal to the recording electrode it was a concern that the light evoked LFP observed may actually be an artifact induced by the stimulus itself. I then repeated the same LFP recording at a similar cortical depth but in a non-injected animal. For the non-injected animal I was unable to generate a light evoked sharp depolarization in the LFP recording but only a sharp depolarization was generated upon whisker deflection providing direct evidence that light evoked LFPs in virus injected animals are not due to any stimulus induced artifacts (Figure 3.6C).

3.2 Retrograde tracer injections into subcortical brain areas

The following description is adapted from Rojas-Piloni, Guest et al. 2017 [22]. Experiments to retrogradely label PTs and in vivo recordings were carried out by Gerardo Rojas-Piloni (Max Planck Florida Institute for Neuroscience).

Pyramidal tract neurons (PTs) located in layer 5 represent the major output cell type of the neocortex. Through long-range projecting axons, L5PTs broadcast results of cortical processing to specific groups of subcortical brain areas. Examining principles of how processed cortical information is broadcast to downstream targets requires experimental approaches which gives accesses to in vivo electrophysiology of PTs, whose long-range axonal subcortical targets are identified. Such an in vivo approach how ever does present some challenges. For example there are genetic markers available to differentiate PTs from other pyramidal cell types in layer 5 of the neocortex but none are known to differentiate them according to their long-range axonal target [55]. There are also large distances to and between the different subcortical brain regions. This makes fully reconstructing the axonal arbor of PTs below the cortex after in vivo electrophysiological recordings quite time consuming and may yield few results. Therefore to overcome these challenges we injected different retrograde tracer agents into multiple subcortical areas, performed in vivo cell-attached recordings of the retrogradely labeled PTs, and filled them with biocytin to reconstruct their dendritic morphologies. This allowed for the investigation of whether cortical output from

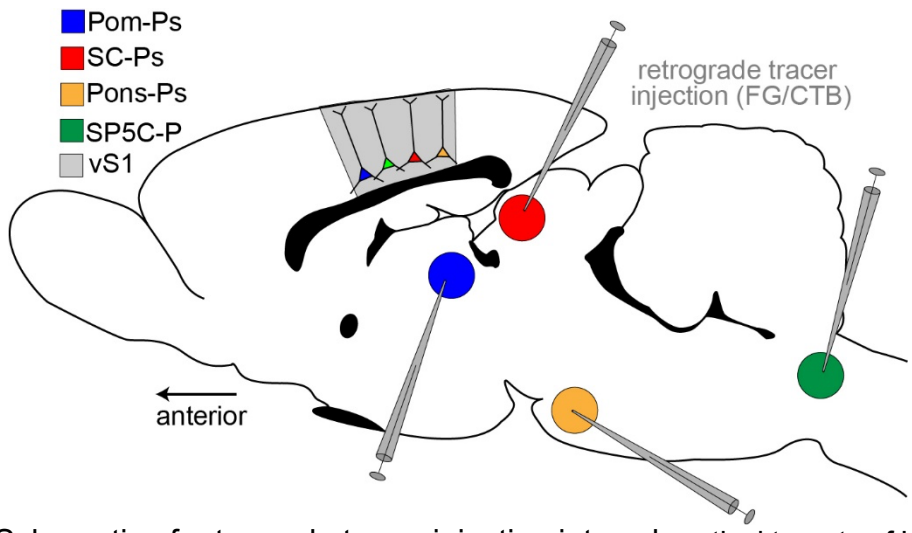

Figure 3.7: Schematic of retrograde tracer injection into subcortical targets of L5PTs in vS1. Illustration of injecting the monosynaptic retrograde tracer Fluorogold into one of the four long-range axonal targets (Pom, SC, Pons, SP5C) of L5PTs per experiment. Resulting in fluorescently labelling L5PTs in vS1 that project to the injected brain region. Figure is adopted from [22].

subcortically projecting layer 5 PTs is organized into long-range target-specific functional pathways. In this section I will present the results of using such a multi-injection retrograde tracer strategy to identify PTs in layer 5 of vS1 according to their respective long-range axonal target as well as analytical results for method validation.

Retrograde Tracer Injections label different populations of PTs.

Experiments to label PTs by long-range axonal target were performed by Gerardo Rojas-Piloni (Max Planck Florida Institute). Previous studies have reported the major subcortical brain regions that are targets of PTs located within vS1 [24], [20], [56], [57]. Here we first determined the respective numbers of PTs that project to four of these major

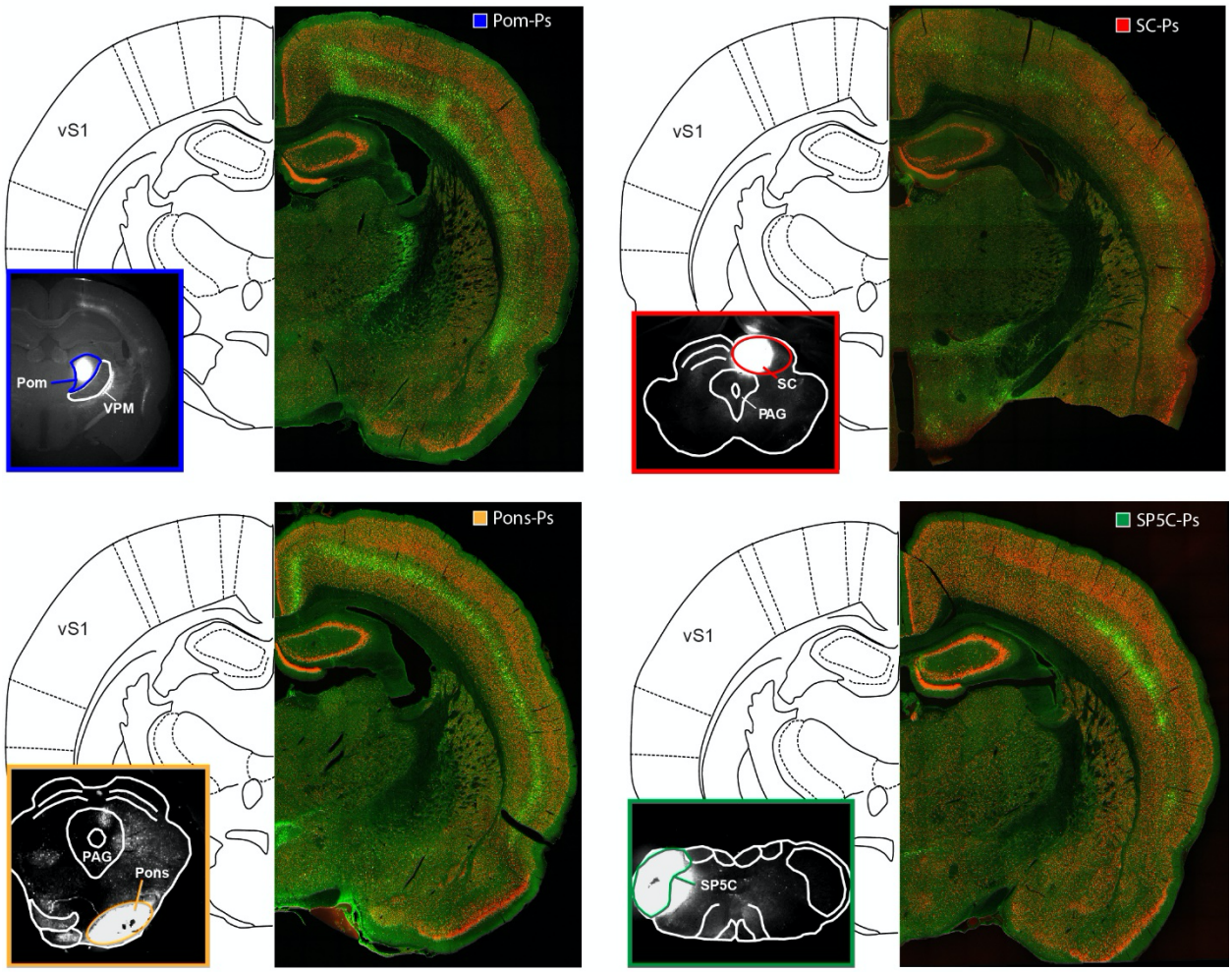

Figure 3.8: Cortex and layer specific labeling of PTs by retrograde injection: Exemplary images illustrating the four subcortical injection sites (Pom, SC, Pons, SP5C) and the respective cortical area and layer-specific retrograde labeling of PTs. Green cells represent retrogradely labeled PTs and red cells represent all neuron somata (NeuN). Images were aligned to the corresponding Paxinos Rat Brain Atlas figure illustrating the center location of vS1 and the center locations of the four brain regions injected with Fluorogold (*n*=3 for each target. Figure is adopted from [22]

brain areas: the posterior medial nucleus of the thalamus (Pom), Pons (Pn), superior colliculus (SC), and the trigeminal nucleus caudalis of the medulla (SP5C) by retrograde injection (Figure 3.7). The monosynaptic retrograde tracer agent Fluorogold (FG) was

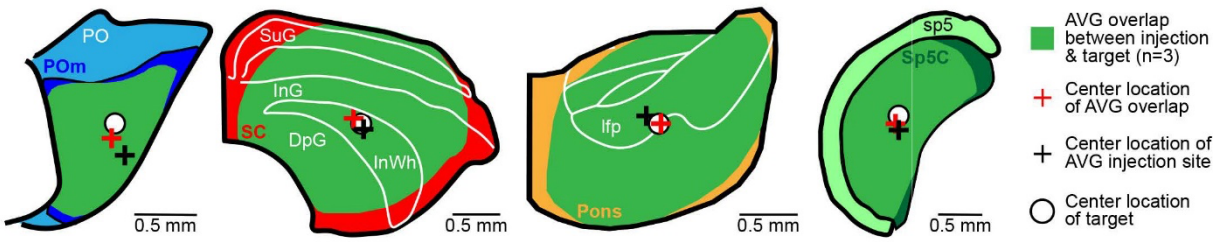

Figure 3.9: Quantification of Fluorogold injection sites. Quantification of the location and overlap of injection sites with the respective target areas (n = 3 for each target). Images of the injection sites shown in Figure 3.8 were aligned to corresponding Paxinos Rat Brain Atlas. The outlines of the targeted brain regions represent those from the atlas. On average, injections sites overlapped to 90 ± 8% with the target ares and the centers of the overlap are were on average ~ 100 µm away from the center locatins of the respective target area. The "average" injection/target overlaps (green shaded areas) correspond to the average soma distributions shown in Figure 3.10. Figure is adopted from [22]

injected into one of the four targets per animal. A total of 12 rats were injected for *n* =3 per injection target. After a six day survival period rats were perfused transcardaily and consecutive 50µm coronal tissue sections were made of vS1 and the injected subcortical brain area. Fluorogold (FG) was immuno-labeled with AlexaFluor488 (FG-488) and all neurons were immuno-labeled with AlexaFluor647 (NeuN-647) (see methods 2.4. 4). FG injection into the four targets resulted in PT target specific labeling in the neocortex (Figure 3.8).

For these single subcortical brain area injections, the locations of the injection sites and their respective overlap within the target region were quantified. To do so low resolution images of the injection sites (shown in Figure 3.8) were aligned and scaled to match the corresponding figures from the Paxinos atlas [48]. The Paxinos atlas figures used for reference were as follows: for Pom – figure 36; for SC – figure 43; for Pons –

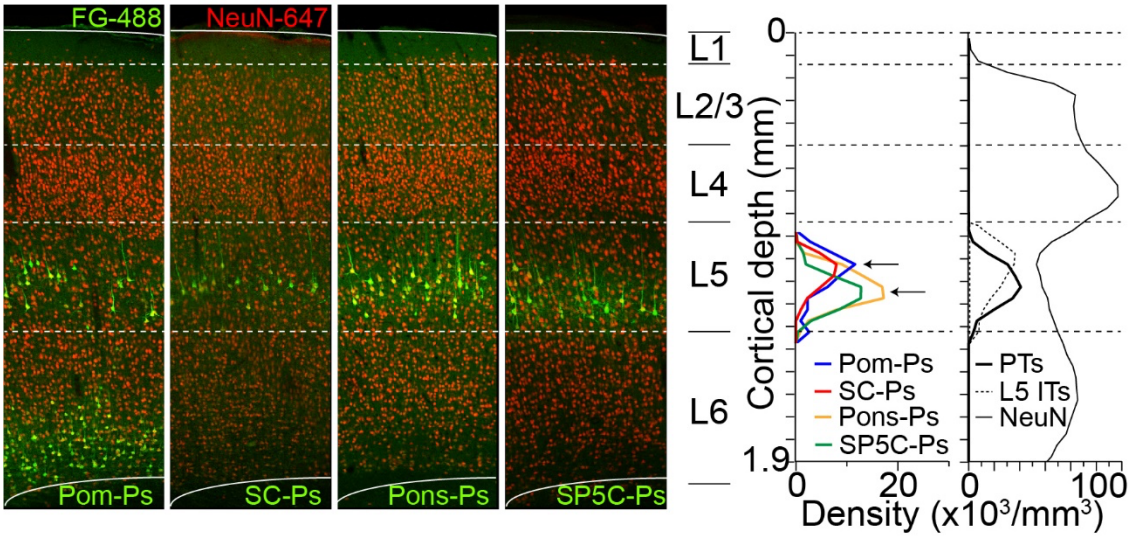

Figure 3.10: L5PTs innervate different subcortical targets: Left panels represent example images from coronal slices of vS1 for each of the four retrograde injected targets. Dashed lines represent layer borders. The respective numbers of L5PTs (FG-488) were quantified with the respect to all neurons (NeuN-647). Right panels illustrate average vertical distributions of L5PT somata. The vertical profile of L5ITs represents the distribution of L5 slender-tufted neurons as determined previously [17, 26]. Figure is adopted from [22]

figure 52; and for SP5C – figure 77. Contours were made to outline the fluorescence signal representing the injection site as well as the target area from the atlas figures were traced using the FilamentEditor [42] in Amira Software [43]. Contours representing the over laps were averaged for each target using the FilamentEditor. The average injection sites and center locations were then measured for a quantitative assessment of tracer spread within and around the targeted brain area (Figure 3.9). It was found that the distance between the center locations of the targeted brain areas and the injection site was 231 ± 121µm (median: 186 µm; range 94 – 487 µm; n = 3 for each target). The injections had a diameter of 2.30 ± 0.45 mm, covering 90 ± 8% of the respective target

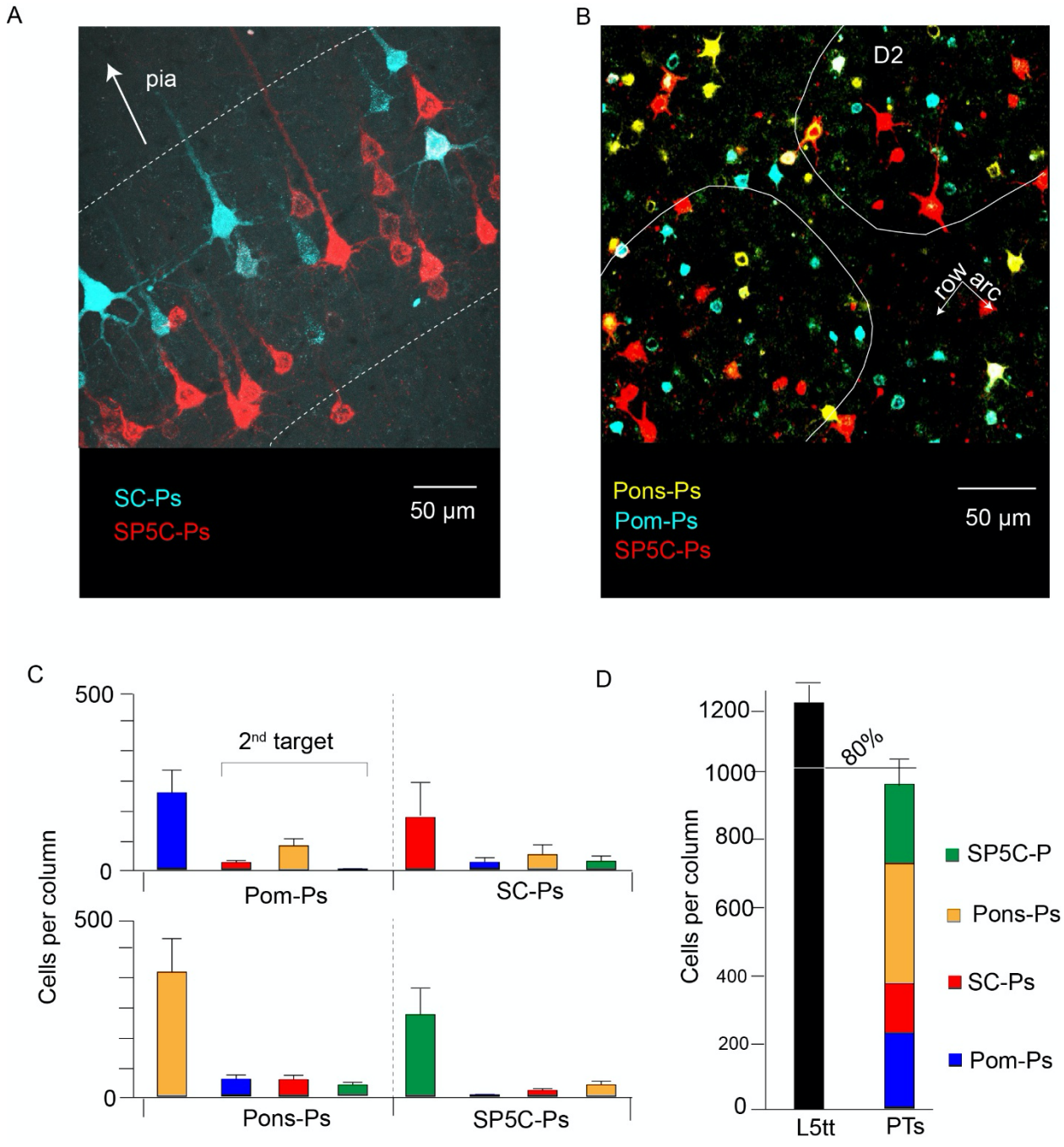
A
pia
SC-Ps
SP5C-Ps
50 µm
B
D2
row
arc
Pons-Ps
Pom-Ps
SP5C-Ps
50 µm
C
500
0
2nd target
Pom-Ps
SC-Ps
500
0
Pons-Ps
SP5C-Ps
Cells per column
D
1200
1000
800
600
400
200
0
80%
Cells per column
L5tt
PTs
SP5C-P
Pons-Ps
SC-Ps
Pom-Ps

Figure 3.11 (*previous page*): L5PTs are organized in target-related sublayers in vS1: (A) Example image from dual tracer injection illustrates overlapping, target-related sublayers in L5 of vS1. (B) Example image from a tangential tissue section of vS1 in L5 illustrate presence of L5PTs in barrel columns and septa. (C) Number of L5PTs per average (C2) barrel column and fractions of L5PTs projecting to two targets. Error bars denote SDs. (D) The total amount of retrogradely labeled L5PTs from panel F shows that ~82% of the L5PNs in vS1 with thick-tufted apical dendrites project to the four subcortical targets injected with CTB/FG. Figure is adopted from [22].

areas (median: 91%; range 74 – 99%) This analysis shows the accuracy of the representative population of PTs labeled by subsequent target injection.

The results from the single target injections also revealed that each subcortical brain area investigated receives input from different cortical areas and layers (for example Pom receives input from layer 6) but always from layer 5 of vS1 (Figure 3.8). The resultant number of FG-488 positive neurons were quantified with respect to all neurons (NeuN-647) for each of the four targets (Pom, SC, Pn, SP5C) within vS1. It was found that the soma distributions of PTs overlapped within L5, but peak densities of PTs projecting to Pom and PTs projecting to SC were found to be located 100 µm superficial than those of PTs projecting to the Pons and PTs projecting to the SP5C (Figure 3.10).

Next, retrograde tracers were injected into multiple subcortical targets within the same animal. CTB conjugated to either Alexafluor594 or AlexaFluor647 (CTB-594, CTB-647) were injected in addition to FG into three of four targets of the same animal (n ≥2 for each animal). Quantification of the retrogradely labeled neurons in consecutive coronal slices from multi-tracer injected brains yielded similar results shown above from single

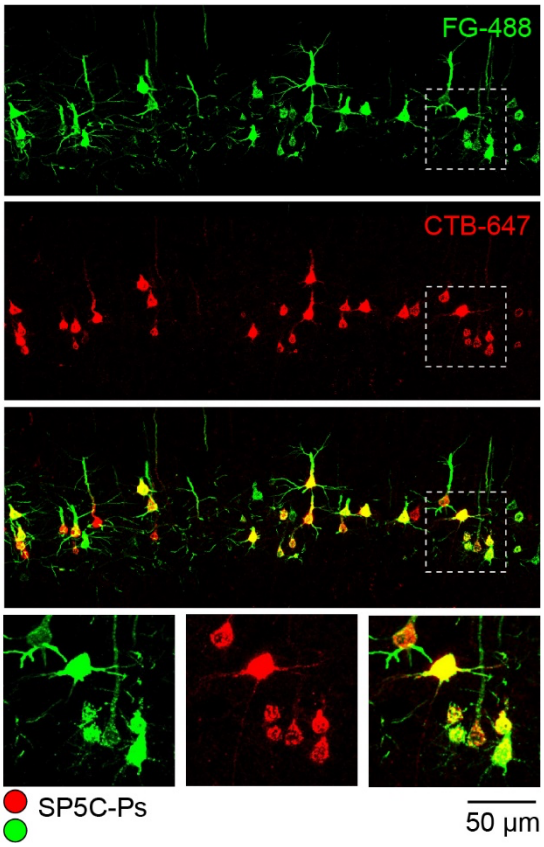

Figure 3.12: FG and CTB have similar labeling efficiencies. Example image of vS1 from control experiments where FG and CTB-647 were both injected into the SP5C via the same pipet. This resulted in double labeling of SP5C projecting L5PTs equally with both tracers, illustrating that FG and CTB have similar labeling efficiencies. Figure is adopted from [22].

tracer injections. The somata of PTs with different target regions intermingled within layer 5, but peak densities of the respective soma depth distributions were target dependent (Figure 3.11A). The results from counting the PTs labeled from the target injections revealed that Pons projectors constitute the largest population of PTs in L5 of vS1, followed by SP5C projectors, Pom projectors, and SC projectors (Figure 3.11C). Quantification of somata distributions of PTs with respect to their target across vS1 from tangential sections were found to be equally abundant within barrel columns and septa

(two-sided *t*-test across 13 tissue sections from 3 rats: $P \geq 0.16$) (Figure 3.11B). A total of 19 ± 12% of the PTs within each group projected to every other second target and 2 ± 3% of PTs were found to project to three targets. Overlap between Pom and SP5C projectors was largely absent. Summing the four distributions of retrogradely labeled somata resulted in a vertical density profile which resembled the distribution of L5 PNs with thick-tufted apical dendrites, as reported previously [17, 26].

Results of injecting FG and CTB in multiple subcortical brain areas within the same animal revealed that most PTs within vS1 only project to one of the four targets investigated. To test whether this is a realistic observation or an artifact from using two types of tracers (FG, CTB) control injection experiments were performed. The two tracers were added to the same injection pipet and injected into the SP5C. The results showed that all SP5C projecting PTs that were fluorescently labeled by FG were also labeled by CTB (Figure 3.12). The result of the dual tracer control injections into the same target illustrate that FG and CTB have similar efficiencies and to not compete with each other.

Identifying subcortical targets of in vivo recorded PTs

The results from injecting retrograde tracers into subcortical brain areas revealed that PTs project their long-range axons largely to only one of the four targets we investigated. The results also revealed that the number of retrogradely neurons, when compared to all neurons in layer 5 of vS1 was relatively low. This can be explained due to that 76% of neurons located in layer 5 of vS1 have been found previously to be excitatory neurons [45], and of those classified as excitatory less than 50% are classified

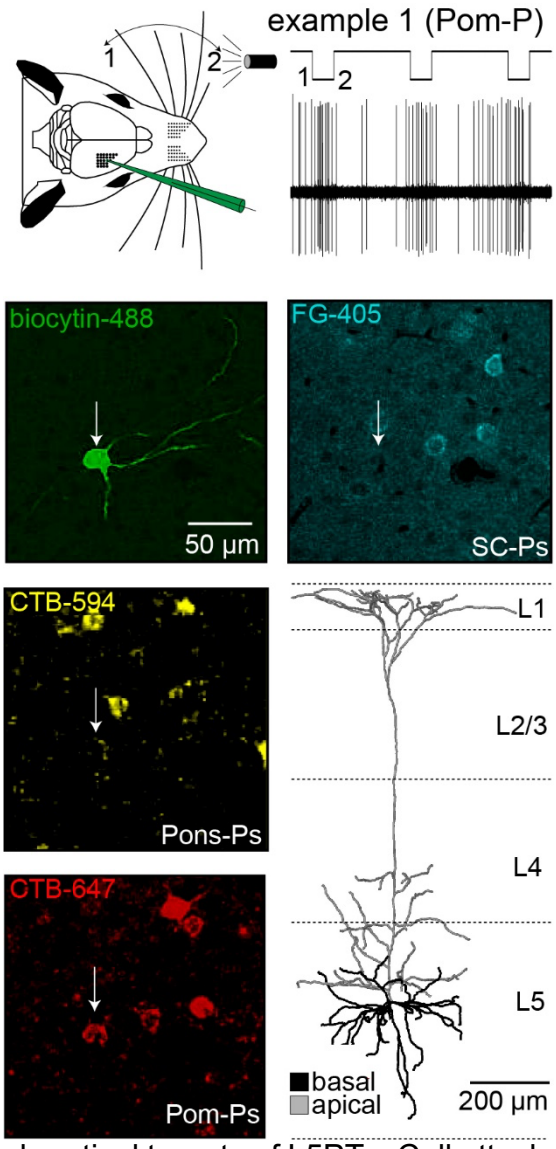

Figure 3.13: Identifying subcortical targets of L5PTs. Cell attached recording and biocytin labeling of exemplary neuron in layer 5, after retrograde tracer injections into SC (FG), Pons (CTB-594), and Pom (CTB-647). Slices were stained with Alexa-405 and Alexa-488 to reveal FG-positive and biocytin-labeled neurons (white arrow). Bottom right panel: 3D dendrite reconstruction of the exemplary L5PT. Figure is adopted from [22].

as PTs [17]. In addition, the labeling efficiency of the retrograde tracers used has been found to be approximately 80% [21]. Therefore, the low fraction of L5 neurons that can in principle be labeled by injections into a single subcortical target (roughly 5 – 10%) is likely a reason that so far has prevented from in vivo recordings of retrogradely labeled L5PTs. To overcome this limitation, we combined retrograde injections of FG and CTB into three targets with cell attached recordings. We used CTB conjugated to Alexa594, CTB conjugated to Alexa647, and FG was immuno-labeled post hoc with Alexa405. During the cell attached recording experiments the recorded neurons were filled with biocytin which was labeled post hoc with streptavidin conjugated to Alexa488. Therefore for each injection-recording combination experiment; 3 populations of PTs were labeled with Alexa405, Alexa594, and Alexa647 with respect to their long range targets and the recorded/filled neuron morphologies were labeled with Alexa488. These four fluorophore combinations were chosen because of the laser configuration of the confocal microscope used for imaging and thus allowed for sufficient separation of the four signals when identifying the long-range target of the recorded neurons.

By combining FG-405, CTB-594, CTB-647 into three targets per experiment at least 20% of L5 neurons were labeled in vS1, thus increasing the success rate of blind patching them. As stated above the recorded neurons were filled with biocytin which allowed for both the identification of the neurons subcortical target and for 3D morphological reconstruction of the neurons' dendrites (Figure 3.13). Measurements of spontaneous and sensory evoked action potential activity were made in anesthetized young rats ages P33 to P42 (n = 32). The morphology of 97 in vivo recorded neurons were also recovered (see example neurons Figure 3.14). Eighty-nine of the labeled

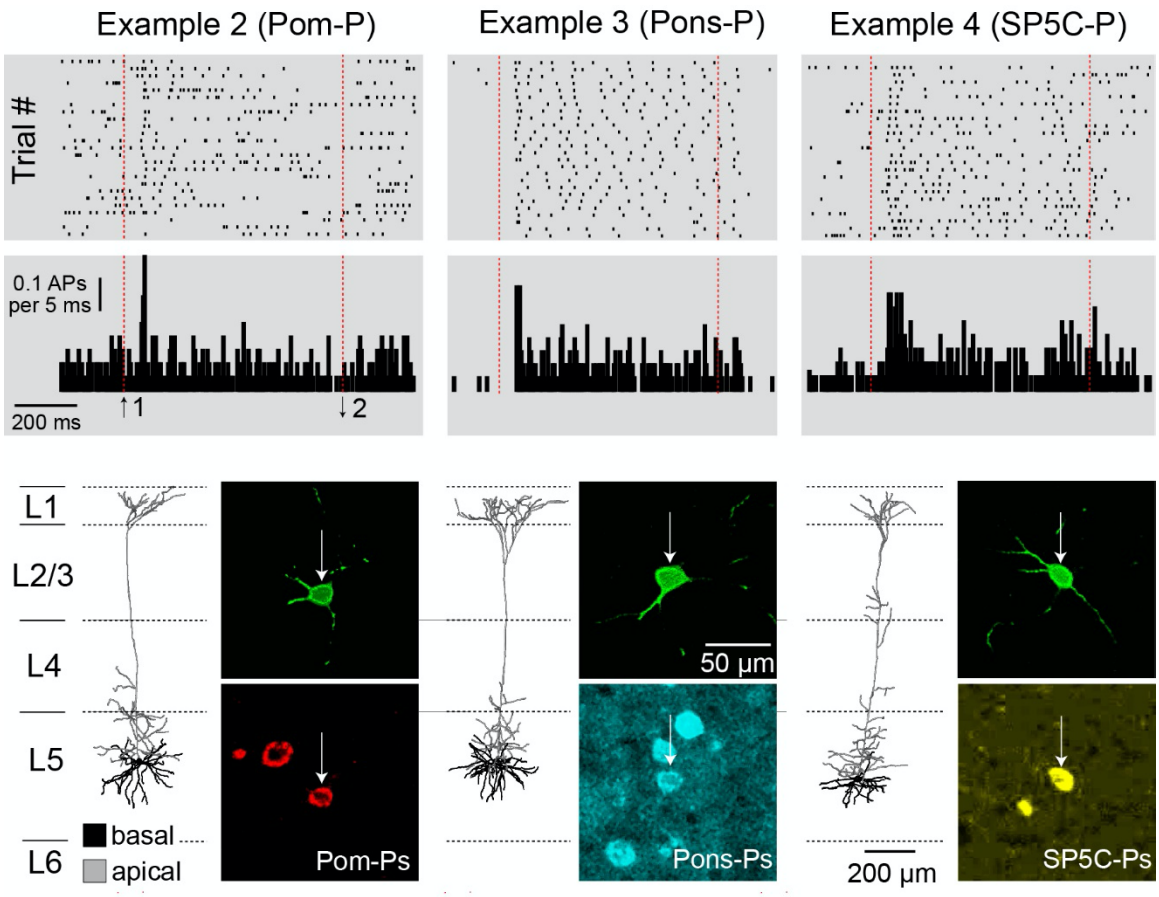

Figure 3.14: In vivo physiology of L5PTs according to their subcortical target. Top panels: raster plots and PSTHs of AP spiking activity before (ongoing), during, and after multi-whisker stimulation (red dashed line) for three example in vivo recorded neurons. Bottom panels: 3D dendrite reconstructions and identification of the respective subcortical targets of the three example L5PTs. Figure is adopted from [22].

neurons were identified as PTs located in layer 5. In agreement with the estimates stated above, 48% of the L5 PNs (43 of 89) were identified as PTs by their dendritic morphology (i.e. thick-tufted apical dendrites). A total of 20 of these PTs were also labeled by a single retrograde tracer and 3 were labeled by 2 retrograde tracers.

3.3 Retrograde tracer injections into whisker muscles

Note: This description is adapted from Guest, et al. 2018 [38]. The generation of the standardized reference frame of the facial nucleus and calculation of volumes or “slabs” representing wMNs of different whisker rows was carried out by Mythreya M. Seetharama (Max Planck Group In Silico Brain Sciences, Center of Advanced European Studies and Research). Procedures to label, image, and manually count rabies positive neurons were done by Aman Maharjan, Li Yida, and Fiorella Osorio (Max Planck Group In Silico Brain Sciences, Center of Advance European Studies and Research) under my supervision.

In a third part of my thesis I aimed to investigate the structural organization of brain-wide whisker related neuronal networks in order to understand if L5PTs within vS1 constitute multiple long-range target specific subnetworks and which of these subnetworks could be involved in whisker motor control. This however requires an experimental approach that would give whisker specific access to the brain wide connectivity of many cortical and subcortical areas across multiple synapses at cellular resolution. Whisker motor neurons (wMNs) located in the lateral part of the facial nucleus (FN), directly innervate muscles that control movement of facial whiskers [58], [59], [60]. As a result wMNs should represent the terminal point of the neuronal networks involved in whisker motor control. By targeting a single whisker muscle with a multi-synaptic neuronal tracer would thereby provide access to the brain-wide structural organization of whisker specific neuronal networks.

Previous studies have illustrated that fixed strains of replication competent rabies virus, such as N2c, allow for specific tracing of motor networks involved in the control of single muscles [61], [62]. Following intramuscular injection, rabies virus enters the central nervous system exclusively through motor neurons [63], [64]. The virus propagates via trans-synaptic transfer exclusively in the retrograde direction, because intracellular transport of the virus after replication is restricted to the soma and dendrites [65], [66]. The trans-synaptic transfer is not gradual, but occurs step-wise at regular intervals of approximately 8 to 10 hours [65], [63], [67]. Rabies tracing thus allows for a precise identification of the trans-synaptic order of labeling, because of the stepwise visualization of successive synaptic relays that is strictly time-dependent and the synchronous labeling of neuronal populations of the same order. For example the trans-synaptic spread of the virus does not depend on the locations of the synapses along the dendrites or axonal length between pre- and postsynaptic neuronal populations [61].

Some studies that have successfully used rabies virus to map muscle specific motor networks involved injecting the virus into arm muscles of monkeys [68], [69]. The authors of these studies not only had visual access to the targeted muscles but could also use electrical stimulation to confirm the identity of the virus injected muscle and as a result provide experimental evidence that the virus was successfully contained within the desired targeted muscle. I however, by injecting an intrinsic muscle innervating a single facial whisker, did not have complete visual access to the targeted muscle nor could perform the electrical muscle stimulation that was done in the monkey studies. Therefore it was necessary to implement an experimental methodology that would provide empirical evidence that a single intrinsic whisker muscle was successfully targeted, even across

experiments representing different synaptic spreads of the virus. In this section I will describe the following methodological results:

1. Labeling whisker specific wMNs in the facial nucleus using monosynaptic retrograde tracer agents.

2. Registration of CTB labeled wMNs across multiple experiments to a standardized reference frame of the FN reveals whisker-row specific organization of wMNs within the ventrolateral part of the FN.

3. Registration of rabies labeled wMNs from injections targeting a single intrinsic whisker muscle into the standardized reference frame of the FN illustrates the accuracy and variability of virus injections across multiple experiments.

Labeling of whisker-specific wMNs in rat FN

I first injected the monosynaptic tracer agents CTB conjugated with Alexa488 (CTB-488), Alexa594 (CTB-594), and Alexa647 (CTB-647) into the mystacial pad, targeting the intrinsic muscles of three adjacent whiskers within the same arc (B2/C2/D2), n = 3 rats) or within the same row (C1/C2/C3, n = 3 rats) (Figure 3.15A,B). After a 6 day survival period the rats were deeply anesthetized and perfused transcardialy. The whisker pads were removed, sliced sagittaly into consecutive 150μm thick sections, and low resolution images were made (Figure 3.15B-D). To illustrate the accuracy of each injection, I made several measurements of the tracer spread throughout the mystacial pad. These measurements revealed that the center of the injections was 910 ± 415 μm (median: 950 μm, range: 400 - 1400 μm) underneath the mystacial pads' surface and 609

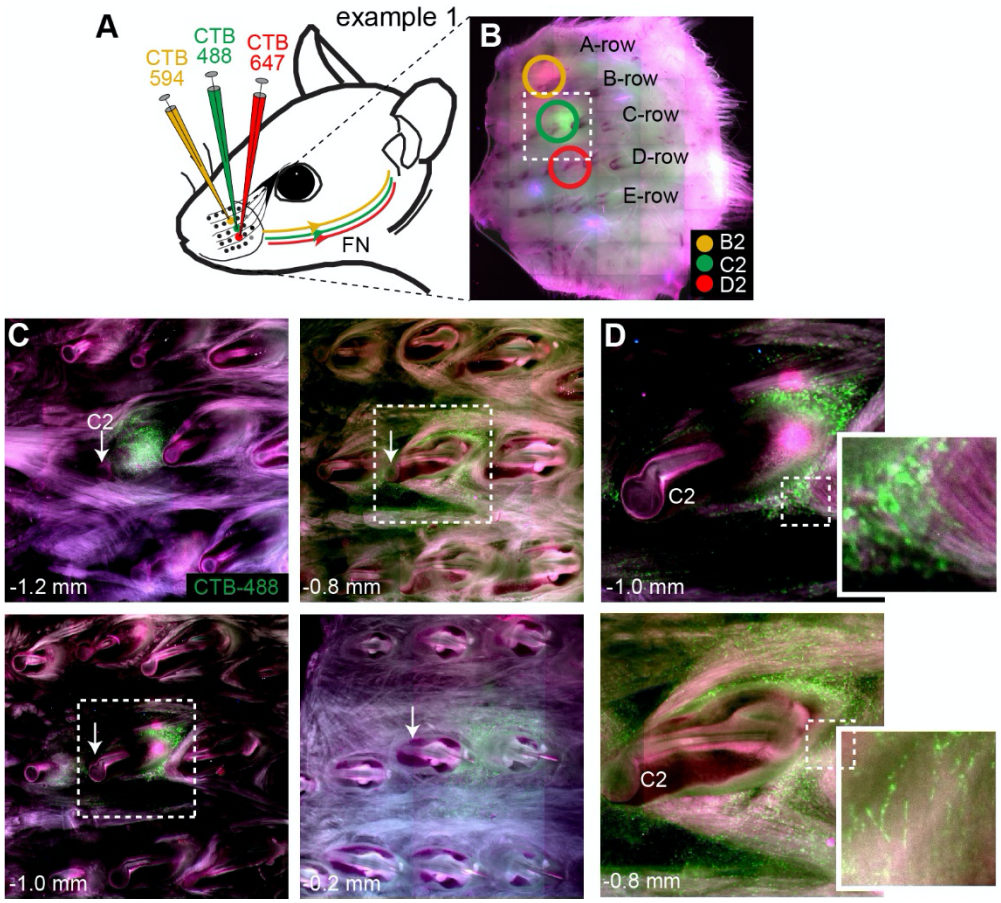

Figure 3.15: Monosynaptic tracer injections into individual whisker muscles. (A) Schematic illustration of the injection experiments of targeting single intrinsic muscles of facial whiskers. Injections of CTB-488, CTB-594, CTB-647 were targeted to the intrinsic muscles of 3 adjacent whiskers (N= 6). (B-D) Illustrations of the injection sites for one exemplary experiment, in which injections were targeted to the B2, C2, and D2 whiskers respectively. (B) Example image of the mystacial pad showing the injection sites. (C) The mystacial pad shown in panel B was sliced into consecutive 150-µm thick sections. Top left panel (1.2 mm underneath the surface of the pad) shows the center location of the injection, which is posterior tot the base of the follicle (white arrow) of the targeted C2 whisker. The remaining three panels illustrate that injections did not spread into the follicle and adjacent intrinsic (see panels at 0.8 and 1.0 mm depths) or extrinsic (see panel at 0.2 mm depth (muscles). (D) Zoom-ins to panels in C illustrate that the retrograde tracer spreads within the injected muscle, i.e. the shape of the injection site resembles the sling of the injected intrinsic muscle. Figure is adopted from [38].

± 415μm (median: 518 μm, range: 185 – 1702 μm) posterior to the base of the follicle. At this depth, the injection sites overlapped with the intrinsic muscle of the targeted whisker and had diameters of 412 ± 182 μm (median: 374 μm, range: 190 – 819 μm). In order to verify whether the tracer stayed within the targeted muscle or may have spread to adjacent muscles I measured the distance between the surrounding follicles. I found that separation between follicles of adjacent whiskers to be more than twice the diameter of the injection sites, and significantly smaller within rows than across rows (789 ± 108 μm vs. 1114 ± 173 μm; $p < 10^{-8}$, n = 22 whiskers, N = 6 rats). Closer examination of the mystacial pad sections also revealed that the CTB did not infect the follicle (i.e. sensory pathways) or tissue between the muscles (Figure 3.15C). Instead the CTB spread within the injected muscle, resulting in injection sites whose shapes resembled the sling of the infected intrinsic muscle (Figure 3.15D). As a result, the CTB injections were precise and small enough to specifically infect the intrinsic muscle of an individual whisker and the spread of CTB to adjacent whiskers if at all was more likely to occur within rows than across rows.

After quantification of the injections sites within the mystacial pads, I sliced the brainstems of these rats into 50-μm-thick consecutive coronal sections and acquired high resolution images for the entire volume of the FN (i.e. N = 3 rats for B2/C2/D/2 and C1/C2/C3, respectively). Quantification of the retrogradely labeled wMNs confirmed the observations made from the mystacial pad injection site analysis. First, wMNs were labeled largely by just a single retrograde tracer, indicating that the injections were in fact restricted to individual whiskers (Figure 3.16A). Second, overlap in labeling was observed exclusively for adjacent whiskers. For example neurons positive for two tracers occurred

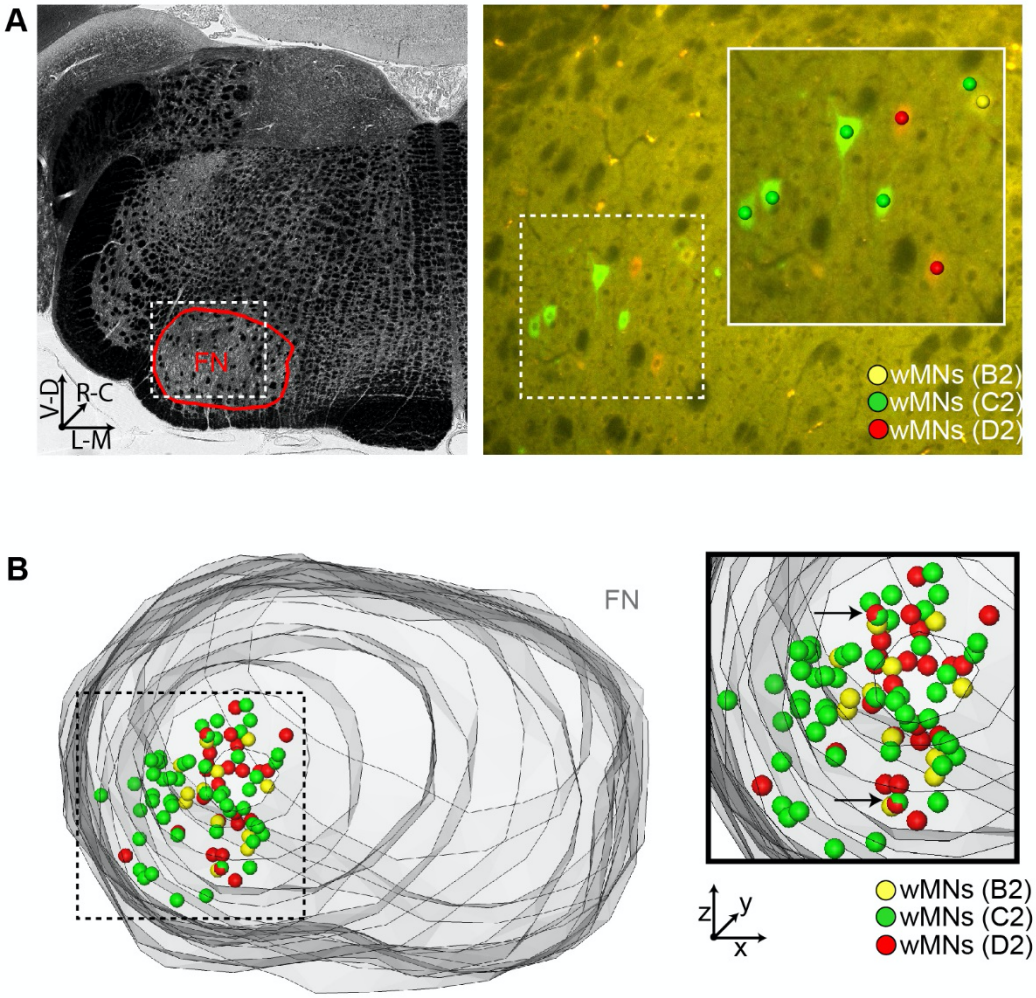

Figure 3.16: Labeling whisker-specific vMNs in rat FN. (A) Left panel: Bright field image of a 50-μm-thick coronal section allows delineating the outlines of the FN. Right panel: Wide-field fluorescent images (merged with bright field image) illustrate that each CTB injection (i.e. corresponding to Figure 3.15 B-D) labels specific set of wMNs. (B) 3D reconstruction of the FN and distributions of all retrogradely labeled wMNs. The zoom-in shows that wMNs were largely whisker specific and confined to the ventrolateral part of the FN. The black arrows denote the wMNs that were labeled by two retrograde markers (i.e. C2/D2), likely reflecting the small spread of the C2 injection toward the D2 whisker (see Figure 3.15 C). Figure is adopted from [38].

as a result of C2/D2 injections but not in B2/D2 injections. Overlap between the tracers was also more noticeable for whiskers injected within the same row (median 4% dual tracer labeling, range: 0 – 30%) than across rows (median 1%, range 0 – 5%). This observation reflects that separation of whisker follicles is larger across rows than within rows. Third, retrogradely neurons were restricted to the ventrolateral (VL) part of the FN (Figure 3.16B), confirming that the CTB did not spread into the extrinsic muscles [70]. Finally, as expected from the variability of the injection site depth, diameter and overlap with the targeted muscle, the number of retrogradely labeled neurons per injection deviated substantially within and across experiments (mean ± SD: 42 ± 32; n = 18 injections in *N* = 6 rats).

Organization of vMNs in rat FN

It has been previously observed that wMNs located within the VL part of the FN exclusively innervate intrinsic whisker muscles and their locations within the FN are organized somatotopically with respect the whisker rows [70]. For example wMNs that innervate A-row intrinsic whisker muscles have been observed in the far lateral part of the FN while in contrast the wMNS that innervate E-row intrinsic muscles have been observed in the more medial part of the FN. In the previous section I provided empirical evidence that it is experimentally possible to infect a single intrinsic whisker muscle with a retrograde tracer agent by quantifying the location of the tracer spread at the site of injection with respect to the resulting wMN labeling in the facial nucleus. This allowed the possibility to be able to give a quantitative account of the whisker specific number and 3D distribution of intrinsic innervating wMNs within the facial nucleus. This however poses

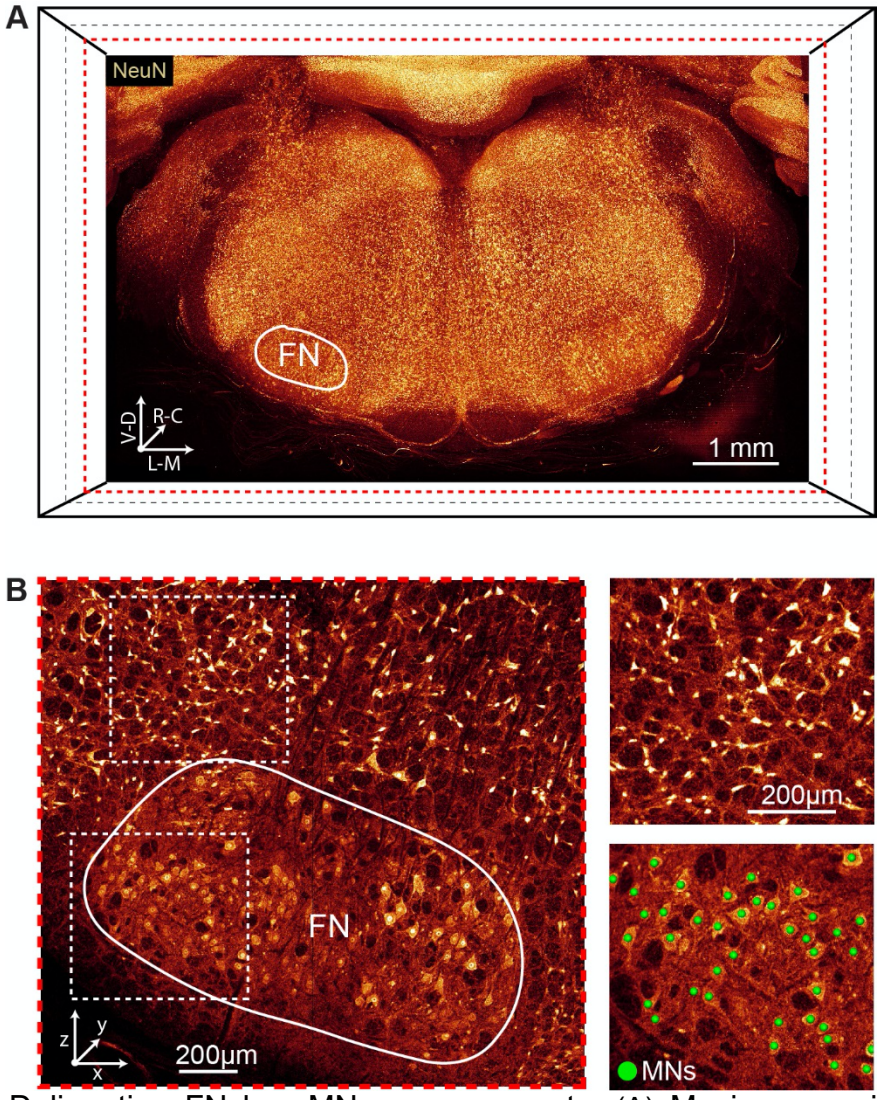

Figure 3.17: Delineating FN by vMN neuron somata. (A) Maximum projection image across all histological brain sections that comprise the FN. Tissue sections were immuno-labeled with NeuN to reveal neuron somata. (B) Zoom-in to one optical section from the image stack in panel A. The outlines of the FN were identified by differences in soma size. Right panels show zoom-ins to illustrate the criteria to delineate the FN by NeuN-labeling. The center locations of all somata within the FN were marked (green spheres). Figure is adopted from [38].

some challenges as giving such a quantitative account of the FN would require collecting data across multiple experiments. In doing so one has to then take into account the animal to animal variability with respect to FN nucleus geometry, volume, and soma density. Therefore similar to previous work done in the lab on the rat barrel cortex [71], my colleague Mythreya Seetharama (Max Planck Group In Silico Brain Sciences, Center of Advance European Studies and Research) generated a 3D reference frame for registration of anatomical data into an average model of the FN geometry. This allowed the comparison of anatomical results of CTB injections into single whiskers across all experiments and to assess the reliability of my rabies virus injections.

The generation of the FN reference frame has been described in detail in Guest et al. 2018 [71]. Briefly, in order to define the FN, I made 50 μm consecutive coronal sections from brainstems from 3 rats. Neuron somata from these tissue sections were immune-labeled with NeuN and high resolution confocal images were acquired. The FN was identifiable by soma morphology and delineated by contouring the outline of the FN using the FilamentEditor [42] (Figure 3.17). All somata were detected manually within each FN contour using Amira software. The resultant 3D distribution of FN neuron somata was largely homogeneous throughout the FN, with soma densities being lowest in the intermediate subdivision between the lateral and medial parts (Figure 3.17B). The mean density of neurons in the FN was 3 ± 1 per 50 μm^3.

This quantification was repeated for 2 additional animals and the volumes of the FN were approximated with an ellipsoid (see methods [38]) (Figure 3.18). The extents of the ellipsoids were found to be 1.3 ± 0.03mm, 1.6 ± 0.02mm and 0.9 ± 0.06mm along the lateral-medial, rostral-caudal, ventral-dorsal axes, respectively. The difference between

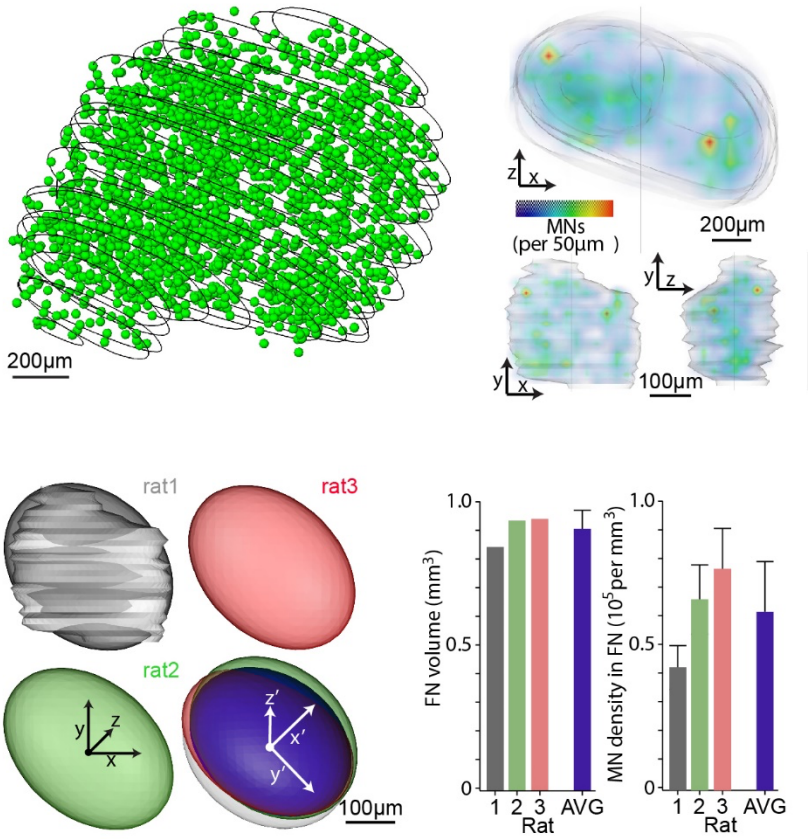

Figure 3.18: Geometry and cellular organization of the rat FN (A) Result of reconstructing the FN outlines and marking all somata from the example experiment shown in Figure 3.17. (B) The outlines were transformed into a surface that delineates the volume of the FN. The soma counts were transformed into a 3D density at 50-µm^3 resolution. (C) The shape and volume of the FN were approximated by an ellipsoid. The experiment shown in Figure 3.17 was repeated for two additional rats and the three FN reconstructions were aligned to yield an average ellipsoid (blue), which represents the FN reference frame. (D) Average (± SDs) volume and soma density if the FN model. Figure is adopted from [38].

the reconstructed FN volume and its approximation by an ellipsoid was 16%. The FN volume determined in this manner remarkably preserved across animals, deviating on average by less than 5%. Thus the ellipsoid is defined as the 3D geometrical reference frame of the rat FN. When extracting the outlines of the FN, different anatomical datasets

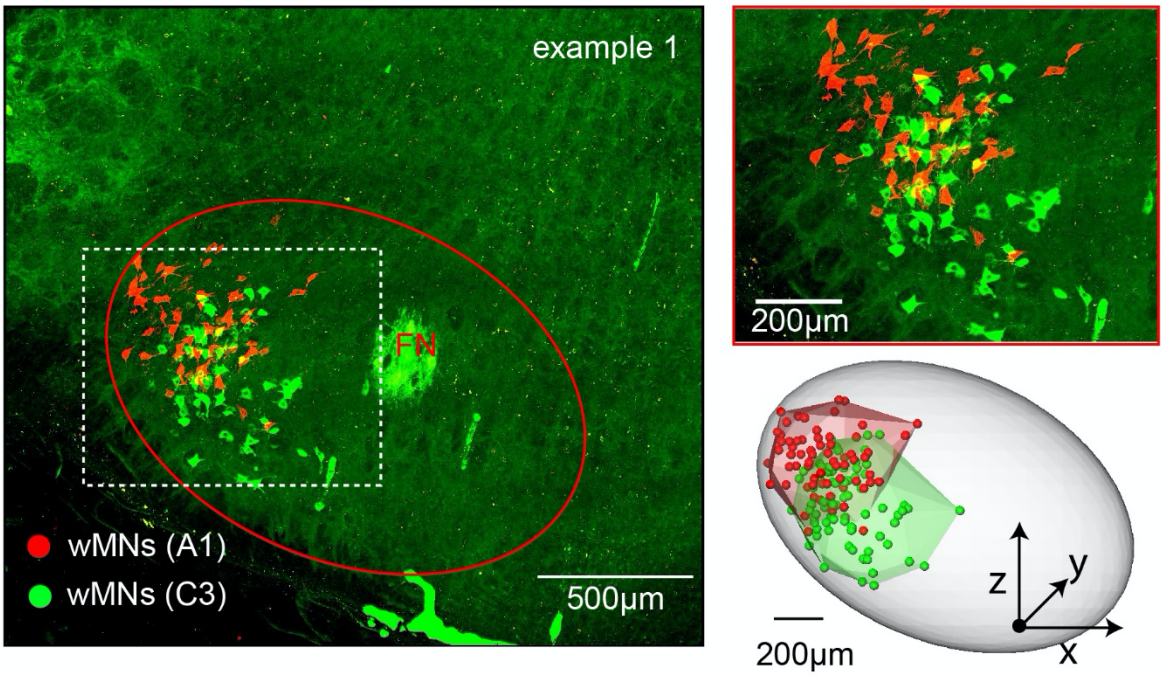

Figure 3.19: Organization of wMNs in rat FN. Example of one of the 13 experiments in which CTB was injected into intrinsic whisker muscles that were separated by at least one whisker. Here, injections were targeted to the intrinsic muscle of the A1 and C3 whisker, respectively. Left panel: maximum projection image across all histological brain sections that comprised the FN. wMNs for both injected whiskers were found throughout the FN along the rostral to caudal axis. wMNs were whisker specific and were confined to the ventrolateral part. Right panels show zoom-in (top) and the center locations of all retrogradely labeled wMNs (bottom). Figure is adopted from [38].

can be registered with an accuracy of approximately ±60 µm to the standardized reference frame, allowing for precise structural analyses across animals and experimental conditions.

I repeated the CTB intrinsic whisker muscle injections in 13 additional animals. In these experiments, I targeted the intrinsic muscles of 36 whiskers that were located

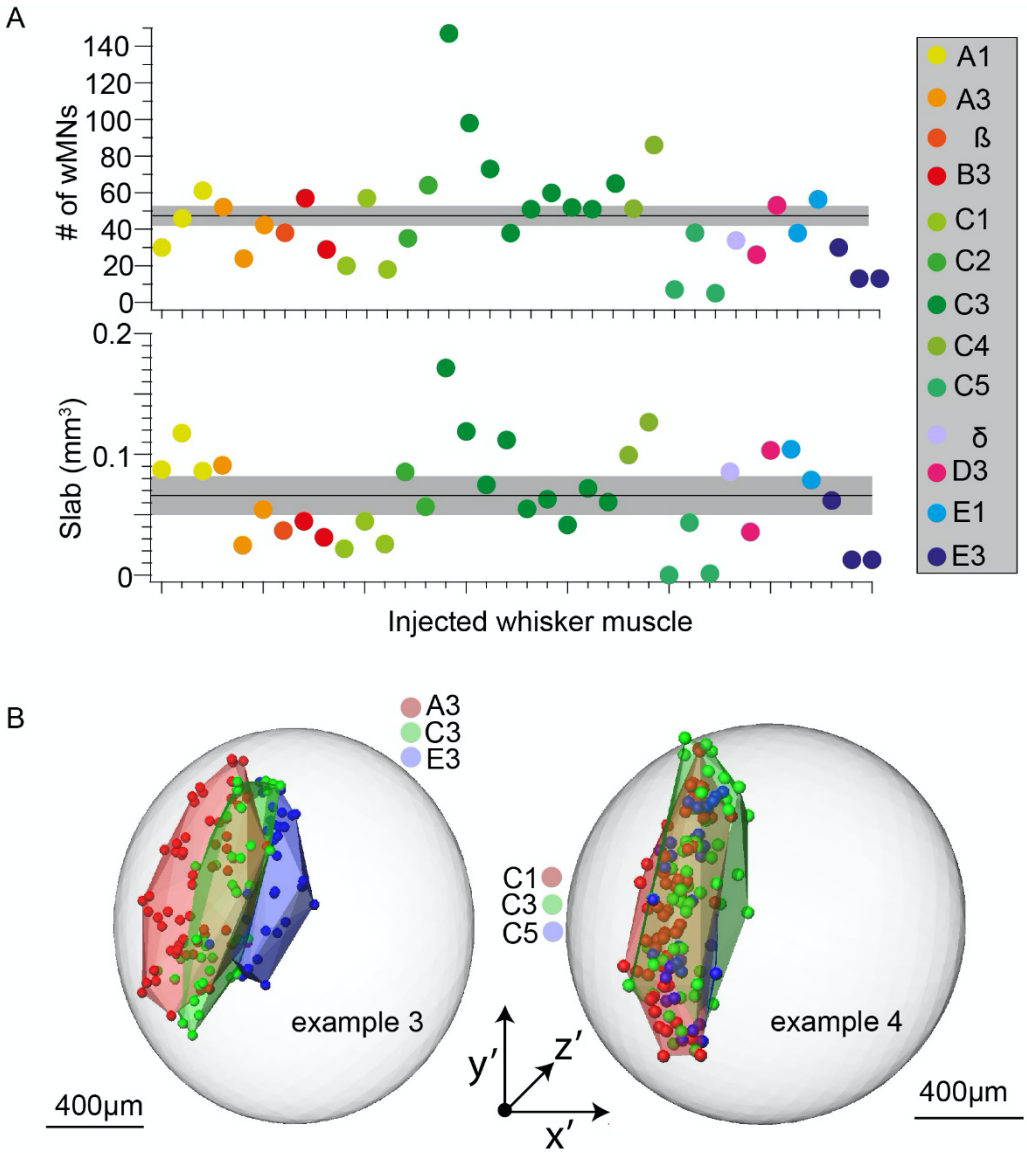

Figure 3.20: wMN distribution and whisker row representative slabs in rat FN. (A) The number of retrogradely labeled wMNs (top) and the respective slab volumes for all injected whisker muscles (n = 36). The black lines and grey shaded areas represent mean and SEM, respectively. (B) Reconstruction of retrogradely labeled wMNs and slab volumes for two additional example experiments. Here, injections were targeted to the intrinsic muscles of the A3, C3 and E3 whisker (left panel), and to the C1, C3 and C5 whisker (right panel). Whisker MNs representing whiskers within the same row are disjoint, but located within the same slab. Figure is adopted from [38].

across the entire whisker pad always separated by at least one whisker. Specifically I injected CTB into three whiskers muscles within the same row (C1/C3/C5, *N* = 3), within the same whisker arc (A3/C3E3, N = 3), along a diagonal axis (A1/C3, *N* = 3) and into mixture of both arcs and rows (C2/C4/E1, *N* = 2; B3/D3/β or δ, *N* = 2). Each injection resulted in labeling a specific set of wMNs, with no overlap between the respective populations (Figure 3.19). The center of the locations of each retrogradely labeled wMN were marked and the outlines of the FN within each brain section were contoured. As a consequence of the variability of the injection procedure, the number of wMNs per whisker deviated substantially across experiments (median: 44 range 5 – 147). However, the number of wMNs was not significantly correlated with the position of the injected whisker in a particular row (Pearson: *R* = -0.17) or arc (*R* = -0.07). Given the efficacy of the CTB (~80% [21]), it is therefore estimated that the intrinsic muscles of each whisker are represented by approximately 60 wMNs in the ventrolateral part of the FN (mean ± SEM of CTB labeled vMNs per injection: 46 ± 5; Figure 3.20A top).

Next a convex hull was calculated around the soma distributions of the respective wMNs (Figure 3.19 lower bottom right). This allowed approximating the volume occupied by the wMNs within the FN (Figure 3.20A). The resultant volumes resembled elongated shells - which will now be referred to as “slabs” – with a maximal extent approximately parallel caudal to rostral (i.e. y’) axis (Figure 3.20B). Similar to the generation of the FN reference frame, each wMN slab was approximated with an ellipsoid. The slab volume (mean ± SEM: 0.065 ± 0.007mm^3) was not significantly correlated with the position of the injected whisker in a particular row (*R* = -0.12) or arc (*R* = -0.20). Slabs representing wMNs of different whisker rows were segregated along the axis that was

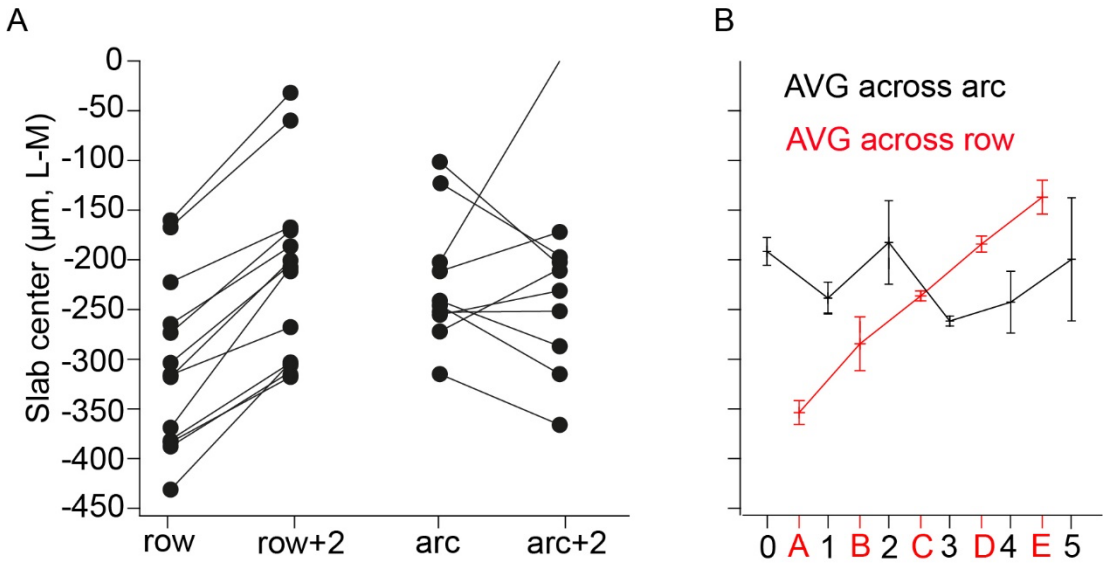

Figure 3.21: Quantification of slab positions within rat FN. (A) Quantification of the slab positions along the lateral to medial axis within each individual experiment (*n* = 36 injections in *N* = 13 rats). Slabs representing different whisker rows were always shifted with respect to each other. Slabs representing different whisker arcs (i.e. within the same row) showed no systematic shift with respect to each other (two-sided t-test: $P < 0.01$). (B) Quantification of the average slab locations along the lateral to medial axis. Error bars denote mean ± SEM. Figure is adopted from [38].

approximately parallel to the lateral to medial (i.e. x') axis (Figure 3.21A). In contrast, slabs of wMNs that represented different whiskers within the same row shared largely the same volume. To quantify the distance between the center locations of slabs that were separated by one row or arc, respectively (Figure 3.21B). In experiments where injections were separated by one row (*n* = 13), the slab representing the whisker closer to the bottom of the snout was always located more medial within the FN. In contrast, slabs representing whiskers of the same row, but different arcs (*n* = 10), were not systematically shifted with respect to each other. Slabs of wMNs that represent intrinsic muscles of whiskers within the A-row are located in the most lateral part of the FN, approximately 0.35mm from the

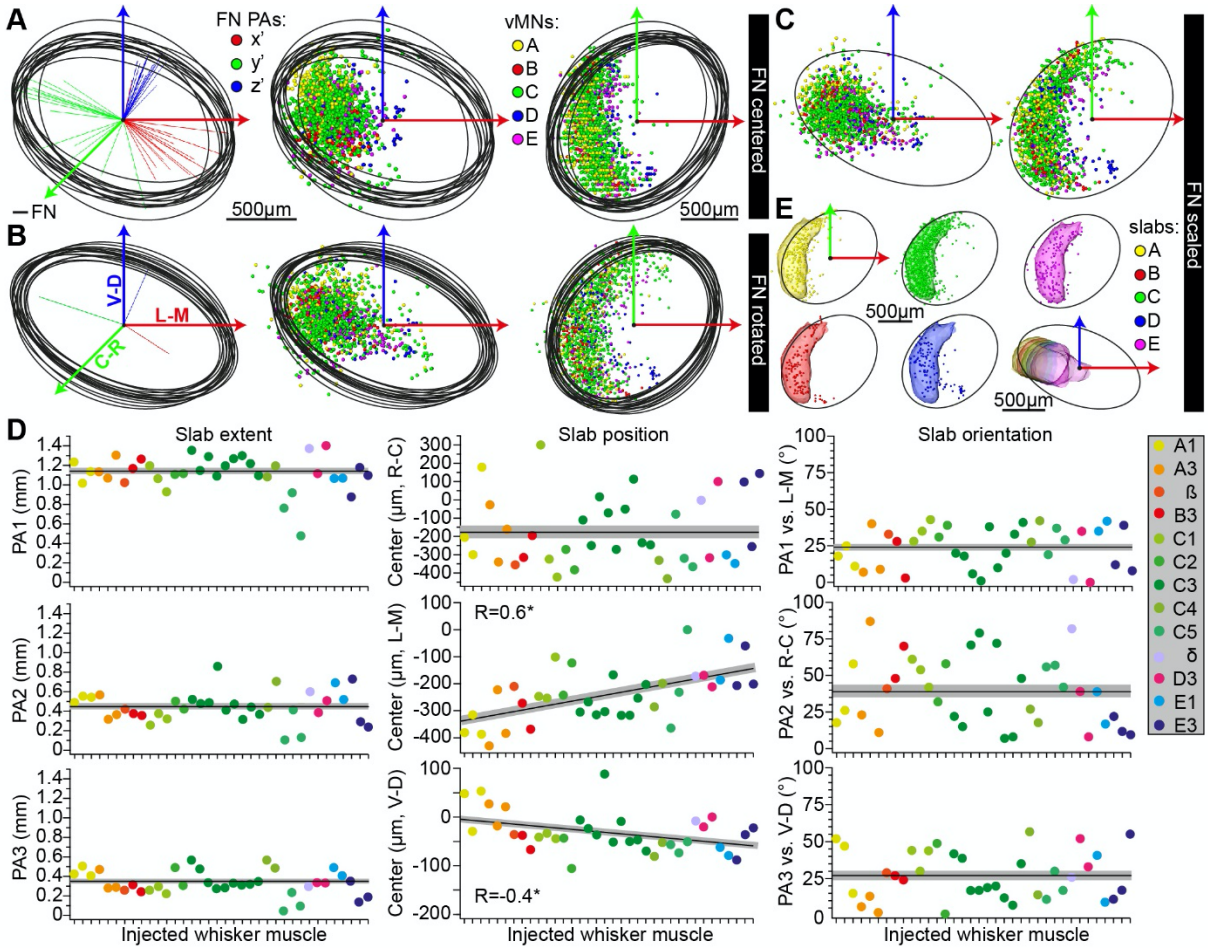
A
FN PAs:
x'
y'
z'
vMNs:
A
B
C
D
E
FN centered
FN
500µm
500µm
B
V-D
L-M
C-R
FN rotated
C
FN scaled
E
slabs:
A
B
C
D
E
500µm
500µm
D
Slab extent
Slab position
Slab orientation
PA1 (mm)
PA2 (mm)
PA3 (mm)
Center (µm, R-C)
Center (µm, L-M)
Center (µm, V-D)
R=0.6*
R=-0.4*
PA1 vs. L-M (°)
PA2 vs. R-C (°)
PA3 vs. V-D (°)
Injected whisker muscle
Injected whisker muscle
Injected whisker muscle
A1
A3
ß
B3
C1
C2
C3
C4
C5
δ
D3
E1
E3

Figure 3.22 (*previous page*): Standardized FN reference frame with wMN slabs. (A-C) The FN of all CTB-injected animals *(N* = 13) were approximated by an ellipsoid, whose centers of symmetry were aligned to the one of the FN reference frame (panel A), whose principle axes were rotated to match the respective ones of the FN reference frame (panel B) and whose dimensions were linearly scaled to match the respective dimensions of the FN reference frame (panel C). In all panels, the respective distributions of retrogradely labeled somata were transformed accordingly. (D) After registration, each wMN slab was approximated by an ellipsoid (*n* = 36) and their respective geometrical parameters are plotted after sorting them by whisker row and then by arc (i.e. from left to right: A1-E3). The black lines and grey shaded areas represent the mean and SEM of the respective parameter in each panel. Left: The 3D extent of the ellipsoids (i.e. length of the three principle axes) did not correlate with the location of a particular whisker along the row or arc. Center: The slab ellipsoids' center locations along the lateral to medial and ventral to dorsal axes (but not along the rostral to caudal axis) did correlate with the location of a particular whisker along the row (but not along the arc). Right: The 3D orientations of the slab ellipsoids did also not correlate with the location of a particular whisker along the row or arc. (E) Geometrical reference frame of the rat FN including the average map of whisker row-specific slabs. Slab positions represent the mean of the respective parameters shown in panel D. Slab sizes and orientations are equal for all slabs and based on the C-row slab. Figure is adopted from [38].

center of the FN reference frame. Slabs of the B-to-E row are shifted with respect to each other toward the medial part of the FN (Figure 3.21B).

Next the soma distributions of retrogradely labeled wMNs, and the resultant sab ellipsoids, were registered into the standard FN reference frame (Figure 3.22). The center of the symmetry and principle axes for each vMN slab ellipsoid were then calculated to determine the relative positon and 3D orientation of each slab within the FN (Figure 3.22). Except for the center positons along the lateral to medial and ventral to dorsal axes, none

of the slabs' geometrical properties such as 3D extent, rostral-caudal position or 3D orientation were significantly correlated with the positon of the injected whisker in a particular arc ($R^2 \leq 0.08$). Consequently, wMNs that represent intrinsic muscles of individual whiskers form a map of shell shaped slabs within the ventrolateral part of the FN, with slab size and orientation being independent of whisker identity, and slab centers being shifted in a row-specific manner (from A to E) by 54 and 19 μm along the lateral to medial and ventral to dorsal axes, respectively. Finally, the geometrical properties of the slabs were used to augment the FN reference frame within an average row-specific map of wMNs. We generated five slabs for rows A through E of equal size and orientation, and placed each slab at its respective average position within the FN. The center location of the C-row slab varied across animals by 51μm. Consequently, the FN reference frame has been augmented to have an average map of the wMNs that is as precise as the FN reference frame itself.

Registration of rabies labeled vMNs into the FN reference frame

I have just described a methodological approach that resulted in the generation of a standardized reference frame of the nucleus that illustrates the whisker-row specific organization of intrinsic wMNs. The purpose of generating such an anatomical reference frame of the FN is to be able to incorporate structural data obtained from different experimental techniques, thereby providing quantitative insight into the structural organization of the neuronal networks that underlie whisker motor control [38]. To illustrate how the FN model can help dissecting brain-wide whisker related networks, I

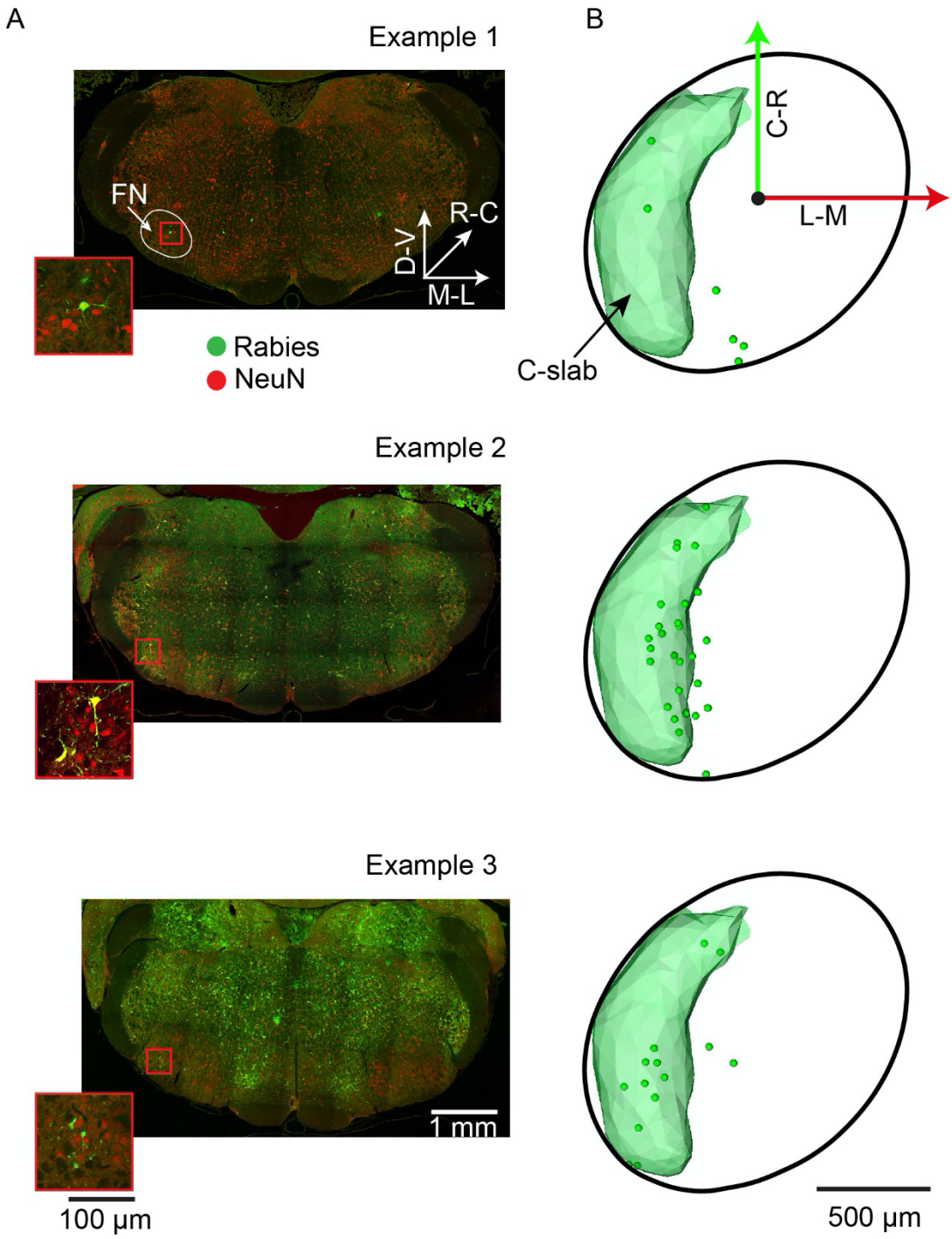
A
Example 1
FN
D-V
R-C
M-L
Rabies
NeuN
B
C-R
L-M
C-slab
Example 2
Example 3
1 mm
100 µm
500 µm

Figure 3.23 (*previous page*): Registration of rabies labeled wMNs. Retrogradely labeled vMNs in the lateral part of the FN resulting from injection of N2C strain of rabies virus into the C3 intrinsic muscle (*N* = 3 rats). (A) Exemplary confocal images from coronal brainstem slices at the location of the FN. White outline delineates the FN and red boxes represent zoom-ins to the lateral part of FN showing rabies labeled wMNs. Top images represent an experiment where rabies labeled neurons were restricted to the brainstem. Middle image represents an experiment where rabies labeling had spread to midbrain areas and to layer 5 of the neocortex. Bottom image represents an experiment where rabies labeled neurons had spread further to cortical layers above and below layer 5. (B) Results of registering rabies labeled wMNs in the lateral part of the FN to the standardized FN reference frame with respect to the slab representing the c-row. The green arrow denotes the caudal to rostral and red arrow denotes to lateral to medial orientations of the standardized reference frames. Top, middle and bottom reference frames represent registration of all rabies labeled wMNs for the three experiments illustrated in panel A respectively.

combined injections of replication competent rabies virus into the intrinsic muscles of the C3 whisker with registration to the standardized FN reference frame.

I injected the N2c strain of replication competent rabies virus into the intrinsic muscle of the C3 whisker. Animals were sacrificed every 12hrs, starting 3 days after injection and the entire brains were sliced into consecutive 50 µm thick coronal sections. Each tissue section was double immune-labeled with NeuN and a highly sensitive antibody against a phosphoprotein the rabies virus synthesizes during replication [72], thus revealing the distributions of rabies positive neurons with respect to all neurons. For the purpose of this thesis I used a total of 3 rats, illustrating different orders of synaptic spread for analysis. The first rat with a survival time of 96hrs after muscle injection, rabies

labeling was observed only in the brain stem. The 2nd rat with a survival time of 84hrs after muscle injection, rabies labeling was observed beyond the brainstem in the midbrain but at the level of the cortex was restricted to layer 5 of vS1, primary and secondary motor cortex. The 3rd rat had a survival time of 96 hours after muscle injection, rabies labeling had spread beyond layer 5 to other sensory cortical areas and layers. The center locations of neurons labeled by the rabies virus within the FN were marked and the outline of the FN was reconstructed as described previously for the CTB whisker injection experiments. The rabies labeled wMNs for each of the 3 experiments were registered to the FN reference frame [38], which confirmed that the locations of these 1rst order wMNs overlapped with those of the CTB labeled C-row somata in the ventrolateral part of the FN (Figure 3.23).

Chapter 4

Biological Results

4.1 Structural and functional properties of primary thalmo-cortical input in vS1

I described in the previous chapter, a method for selectively labeling and expressing channel rhodopsin in primary TC synaptic terminals within vS1 by injecting a recombinant adeno-associated virus (rAAV) into the VPM of rats. By combining these virus injection experiments with cell attached recordings and morphological reconstructions, I was able to both measure the neuronal response properties to photo stimulated TC synapses and quantify the structural organization of TC inputs on the dendrites of the neurons I recorded from. From these experiments I recovered a total of 65 morphologically identifiable neurons across 36 successfully injected rats. These 65 neurons segregated into 5 different morphological cell types. Four neurons were found to be layer 4 spiny stellates (L4sp), 5 were found to be L5 slender-tufted pyramids (also called intratelencephalic (IT) neurons), 25 were found to be L5 thick-tufted (also called pyramidal tract neurons (PTs)), 6 were found to layer 6 cortico-cortical pyramids

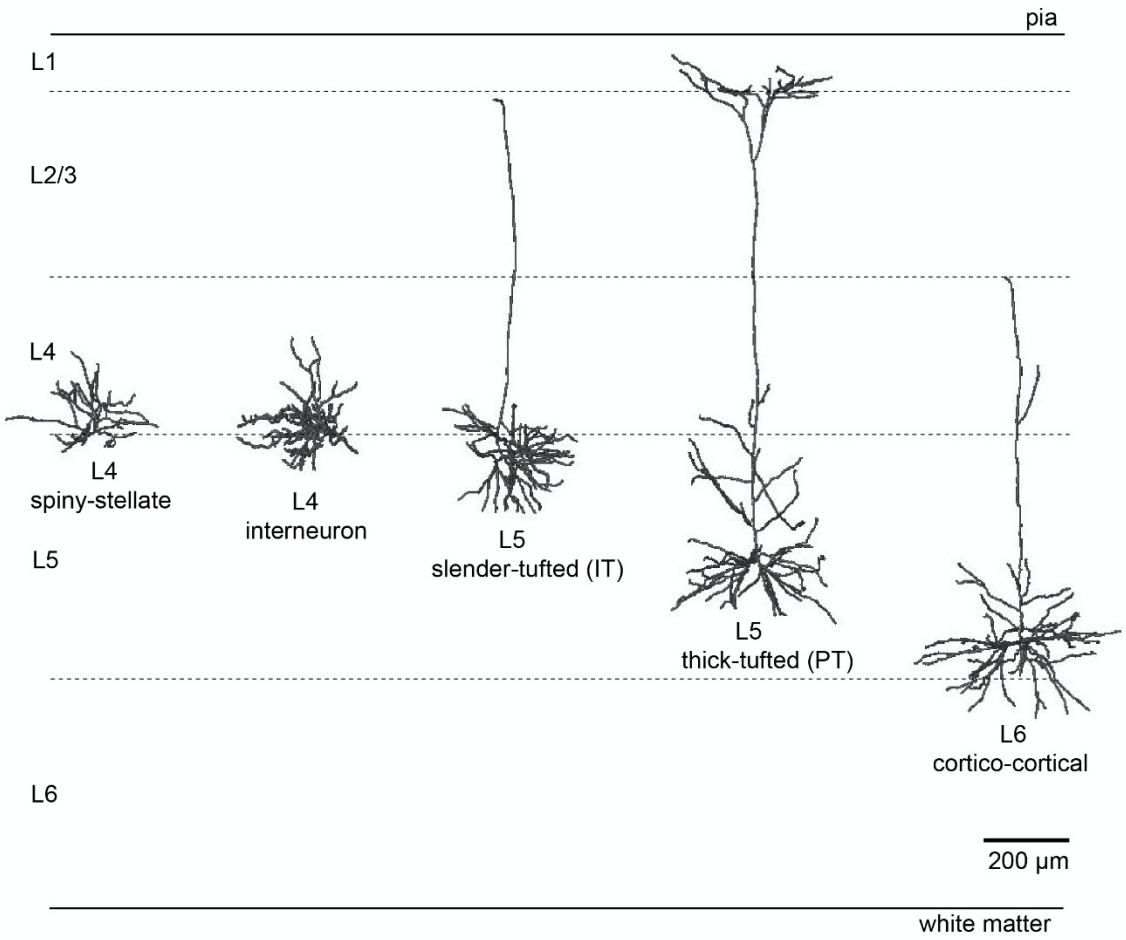

Figure 4.1: Morphological reconstructions of in vivo recorded neurons. Semi coronal view of complete dendrite reconstructions to illustrate the 5 different morphological neuronal cell types recovered from the rAAV injection experiments. Neurons (excluding the L4 interneuron) were registered to a standardized reference frame of the rat barrel cortex in order to obtain soma depths with respect to the pia surface. The pia to soma distance was measured manually using Amira software for the L4 interneuron. The dashed lines represent layer boarders and solid line represents the pia/white matter in vS1 as determined in [45].

(L6CC), and 22 neurons were identified as interneurons located across layers 4, 5, and 6 (see figure 4.1 for example morphologies). The electrophysiological response properties to whisker stimulation and photo stimulation were analyzed and is reported

here in this thesis. For quantification of TC input, I reconstructed and mapped all of the TC inputs onto the dendrites of 1 example layer 4 spiny stellate, 1 example L5IT, and 10 L5PTs, the results of which are also reported here. 1 L6CC was reconstructed by Marcel Oberlaender (Max Planck Group In Silico Brain Sciences, Center of Advanced European Studies and Research) and the primary TC inputs quantified by Rajeev Narayanan (Max Planck Group In Silico Brain Sciences, Center of Advanced European Studies and Research) published in [23] was also used for analysis and reported here. In the following section I will now describe in detail both the functional and morphological properties of primary TC input within vS1.

4.1.1 Cell-type specific response properties to photo stimulated primary TC synapses

Virus injected rats were re-anesthetized and cell attached recordings were performed. The sensory evoked action potential (AP) responses of neurons to passive multi-whisker deflection (air puff stimulation) and photo stimulated TC synapses were recorded (Figure 4.2). First by air puff stimulation, the whiskers (to include the principle and surrounding whiskers) were deflected for 700ms at a frequency of 0.30Hz for 30 trials. Next, TC synapses were stimulated by 10ms of pulsed light through an optical fiber positioned just above the cortical surface in close proximity to the recording site. Three different photo stimulation protocols were performed for each recorded neuron were as follows: 10ms pulsed light at a frequency of 0.40Hz (inter-stimulus interval of 2500ms) for

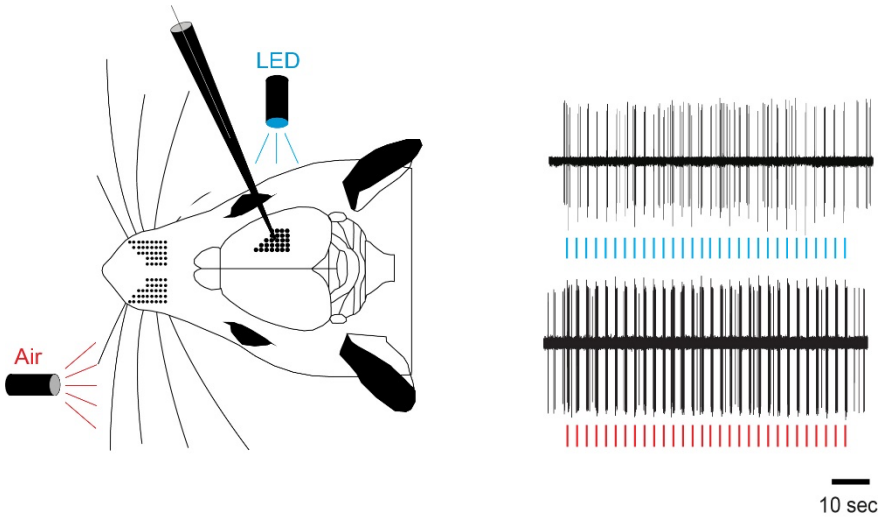

Figure 4.2: Schematic of in vivo optogenetic/passive multi-whisker recording experiment. Rats were first injected with rAAV expressing channel rhodopsin into the VPM to selectively label primary TC synapses in vS1. After a 16 – 21 day survival period rats were re-anesthetized and post synaptic neuronal responses to an air puff whisker stimulation and photo stimulation of TC synapse were recorded. Right panel: Filtered extracellular signal from a recording experiment illustrating AP responses from a L5PT (example 2 from Figure 4.7) to whisker deflection (top) and photo stimulation (bottom).

30 trials, then 10ms of pulsed light at a frequency of 1.96Hz (inter-stimulus interval of 500ms) for 50 trials, and finally 10ms of pulsed light at a frequency of 9.09Hz (inter-stimulus interval of 100ms) for 100 trials.

Ongoing AP activity

Ongoing AP spike rates were first determined for the 65 recovered neurons by the number of spontaneously occurring APs during 200ms prior to whisker stimulation across all 30 trials. The ongoing AP activity rates were then averaged according to morphological cell type and were found to be similar to previous reports [54]. The mean ongoing A.P.

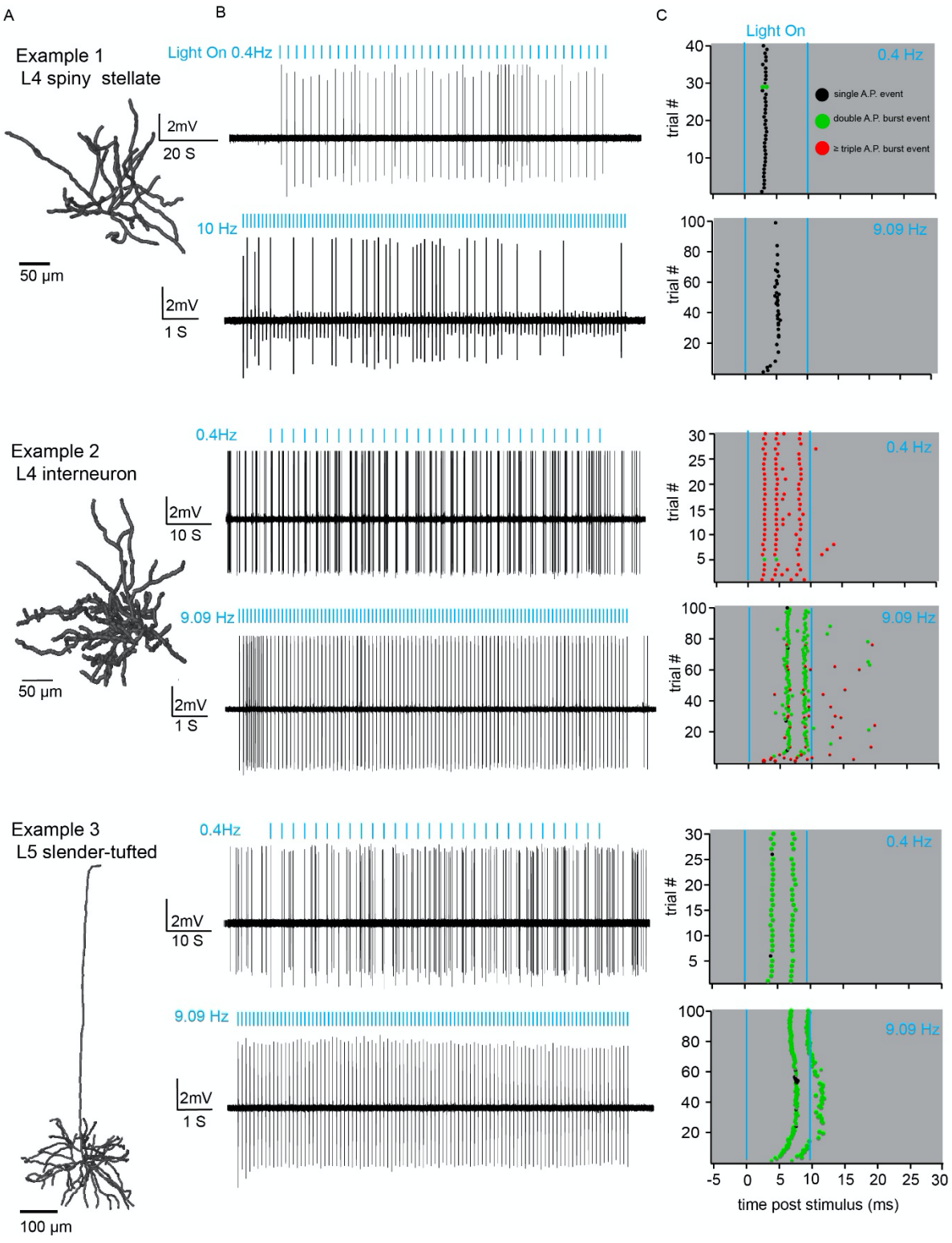
A
B
C
Example 1
L4 spiny stellate
Light On 0.4Hz
2mV
20 S
50 µm
10 Hz
2mV
1 S
Light On
0.4 Hz
single A.P. event
double A.P. burst event
≥ triple A.P. burst event
trial #
9.09 Hz
Example 2
L4 interneuron
0.4Hz
2mV
10 S
50 µm
9.09 Hz
2mV
1 S
Example 3
L5 slender-tufted
100 µm
time post stimulus (ms)

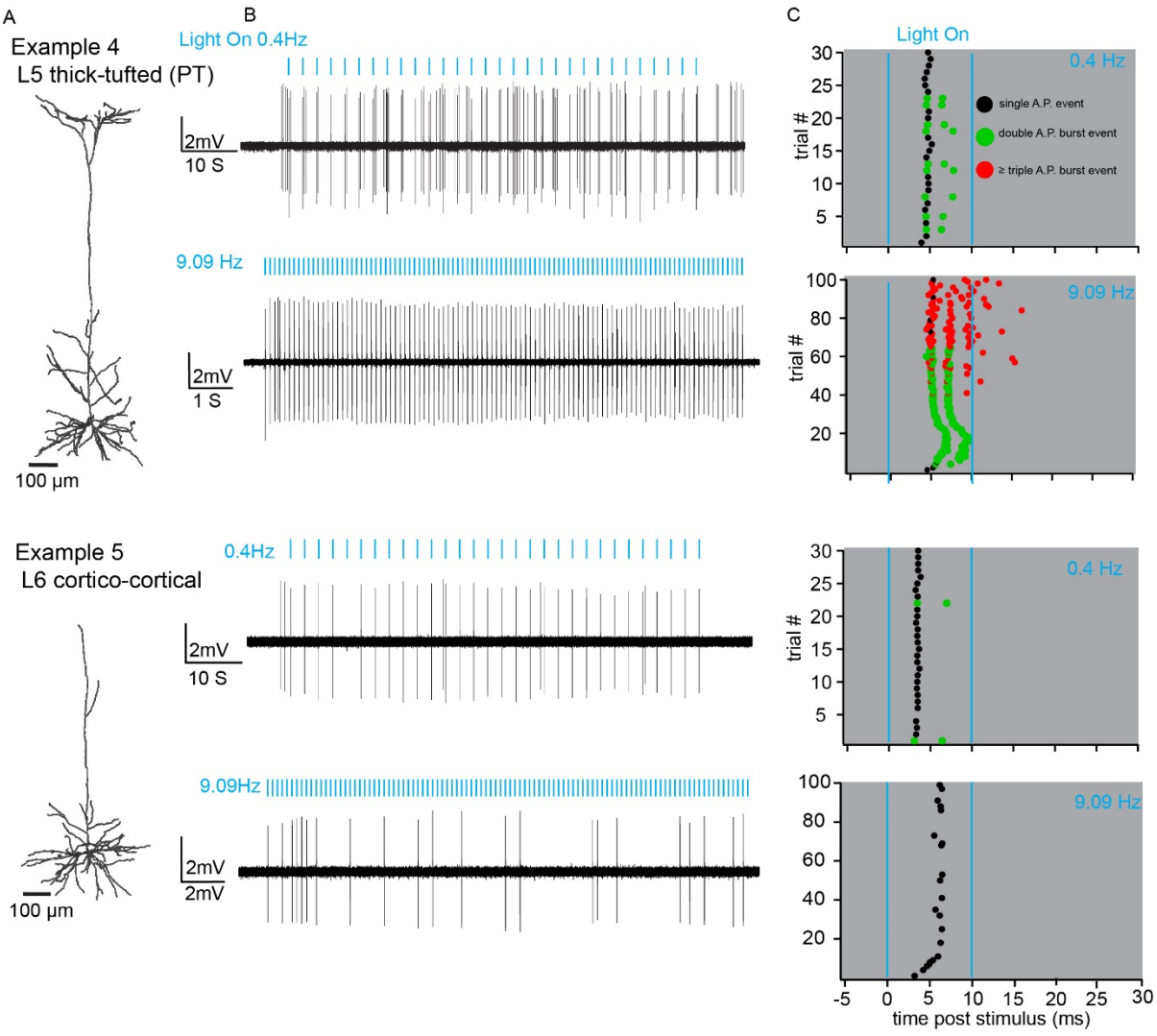

Figure 4.3 (*previous 2 pages*): Cell type specific responses photo stimulated TC synapses. (A) Example morphologies illustrating the five different neuronal cell types recovered from the rAAV injection experiments (same reconstructions shown in Figure 4.1). (B) Filtered extracellular signals from the recording experiment of the respective neuron in A. Top recording trace are AP responses to a .4 Hz photo stimulation of TC synapses and bottom recording trace are AP responses to a 9.09 Hz photo stimulation. Blue dashed lines illustrate when light stimulus was on and black lines represent action potentials. C. Raster plots for the recordings shown in B. Black markers represent single AP responses, green markers represent double AP responses and red markers represent three or more action potential responses measured at frequency greater than or equal to 100 Hz.

rates for the present sample of L4sp, interneurons, L5ITs, L5PTs and L6CC were determined to be 0.41 ± 0.23 Hz (*n* = 4), 1.24 ± 0.30 Hz (*n* = 22), 1.57 ± 0.42 Hz (*n* = 5), 2.21 ± 0.39 Hz (*n* = 25), and 1.02 ± 0.29 Hz (*n* = 6) respectively.

Post synaptic evoked responses to photo stimulated TC synapses are reliable and fast.

The sensory evoked AP responses of in vivo recoded neurons to photo stimulated TC synapses were analyzed with respect to morphological cell type (Figure 4.3). It was found that independent of morphological cell type, AP firing rates across all recorded neurons increased significantly on average to 36.23 ± 2.47 Hz (*n* = 65; two-sided *t*-test, paired: $P < 10^{-5}$). 84 percent of neurons in the present sample (51/65) responded with at least a single AP in the majority of trials at the onset of the 10ms light stimulus (see Figure 4.3C for examples), which therefore is defined as an “onset evoked event”. Three types of onset evoked events were observed that varied from across cell types (Fig 4.3C). In trials where an onset event occurred the response was with either a single AP, a burst of two APs (doublet burst) or a burst of three or more APs.(≥ triplet burst). Bursts of APs are defined as two or more APs that occur at a frequency greater than 100 Hz as previously reported [46]. Therefore both the probability of the occurrence of an onset event and occurrence of bursts events along with the latencies of evoked onset events were determined for all neurons with respect to morphological cell type.

For each cell type the average probability of an onset evoked event occurring within the first 20ms post light stimulus for each photo stimulation protocol was determined (Figure 4.4A). L4sps responded with a mean onset probability across all stimulus protocols of 0.52 ± 0.2. Seventy-five percent of L4sp recorded responded to the light stimulus (3 of 4) but had the lowest onset response probability when compared to the other four cell types. There was no significant change in evoked onset probability from the 0.4 Hz stimulation protocol to the 9.09 Hz stimulation (n = 4, two-sided t-test, paired: P = 0.16). Interneurons had the second highest evoked onset probability across all three stimulation protocols with a mean probability of 0.61 ± 0.1. Sixty-eight percent of interneurons recorded responded to the light stimulus (15 of 22) and there was a significant decrease in evoked onset response probabilities from the 0.4 Hz stimulation protocol to the 9.09 Hz stimulation protocol 0.63 ± 0.1 and 0.53 ± 0.1respectively (n = 22, two-sided t-test, paired: P = 0.04). L5ST neurons showed the most reliable evoked onset response across all stimulus protocols with a mean response probability of 0.72 ± 0.18. Eighty percent of L5ST recorded responded to the light stimulus (4 of 5) with no significant change in evoked onset event probability from the 0.4Hz stimulus protocol to the 9.09Hz (n = 5, two-sided t-test, paired: P = 0.46). Similar to the interneuron population, the L5PTs

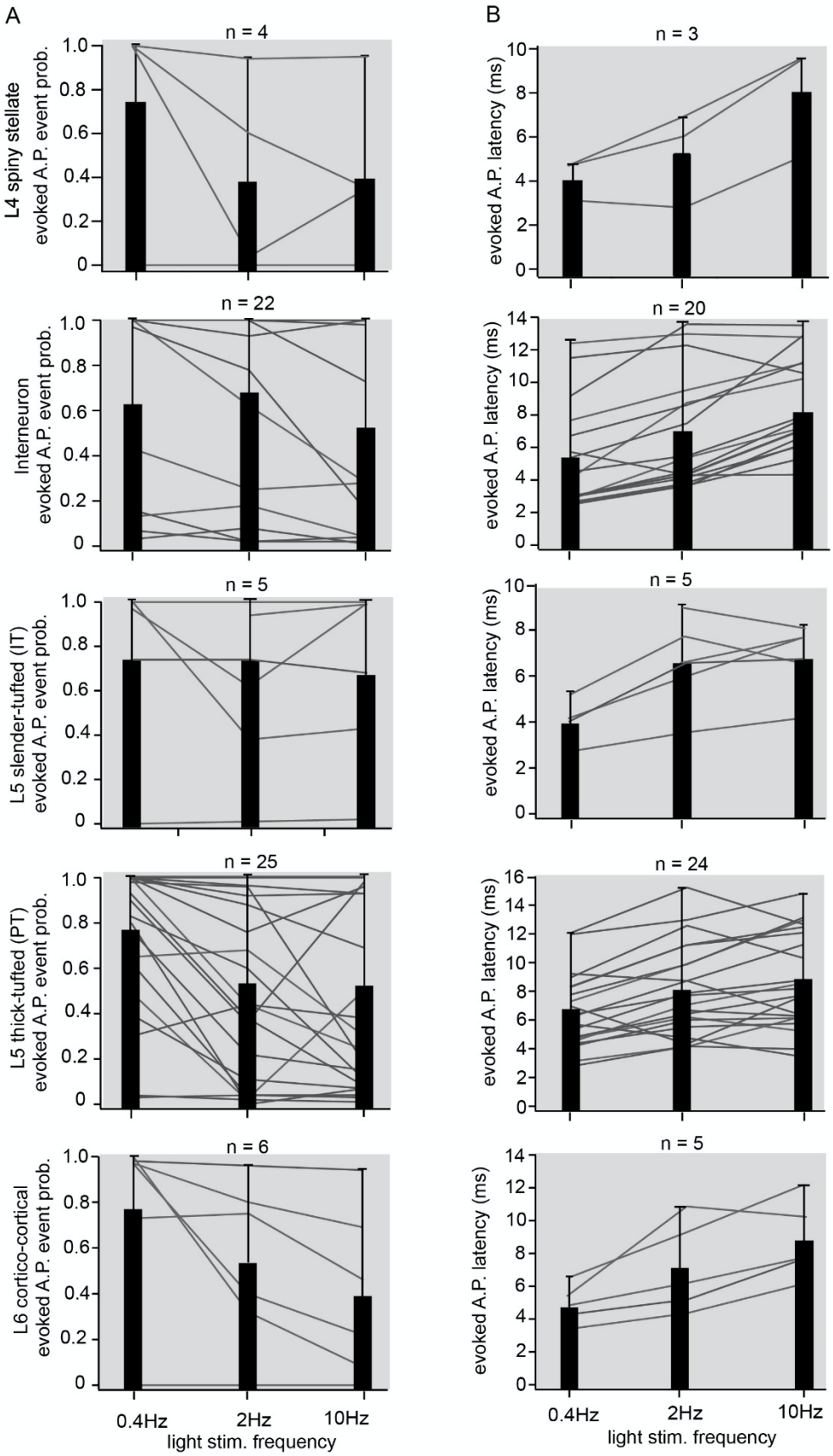
A
B
n = 4
n = 3
L4 spiny stellate
evoked A.P. event prob.
evoked A.P. latency (ms)
n = 22
n = 20
Interneuron
evoked A.P. event prob.
evoked A.P. latency (ms)
n = 5
n = 5
L5 slender-tufted (IT)
evoked A.P. event prob.
evoked A.P. latency (ms)
n = 25
n = 24
L5 thick-tufted (PT)
evoked A.P. event prob.
evoked A.P. latency (ms)
n = 6
n = 5
L6 cortico-cortical
evoked A.P. event prob.
evoked A.P. latency (ms)
0.4Hz
2Hz
10Hz
light stim. frequency

Figure 4.4 (*previous page*): Neurons in vS1 display reliable and fast AP responses to photo stimulated TC synapses (A) Probabilities of responding to at least one AP (defined as an evoked event) during the three photo stimulation protocols for all neurons recorded and grouped by morphological cell type. Response probabilities were calculated as the number of evoked events observed during the first 20ms when the 10ms photo stimulus occurred divided by the number of trials. (B) The evoked AP latencies observed for every neuron recorded during the three stimulus protocols. Latencies were calculated as the time the first spike occurred post light stimulus during the first 20ms and then averaged across all trials for each neuron. (A-B) Thick vertical bars represent the population mean for each morphological cell type. Thin vertical bars represent the maximum range and thin horizontal bars represent individual neurons within the population of each morphological cell type.

also had a mean evoked onset event probability across all stimulus protocols of 0.61 ± .06. Ninety-two percent of L5PTs responded to the light stimulus (23 of 25) and a significant decrease in evoked response probability was observed from the .04 Hz stimulus protocol to the 9.09 Hz protocol 0.77 ± .06 and 0.52 ± 0.09 respectively (n = 25, two-sided t-test, paired: P = 0.002). Finally the L6CCs mean evoked response probability was higher than the L4sp but lower than the L5PTs with a mean response probability of 0.57 ± .013. Eighty-three percent L6CC responded (5 of 6) to the light stimulus with no significant difference in evoked response probabilities from the 0.4 Hz stimulus protocol to the 9.09 Hz stimulus protocol n = 6, two-sided t-test, paired: P = 0.06).

Next, those neurons that showed a response to the photo stimulus, the latencies of the responses were measured (Figure 4.4). Evoked response latency is defined as the

time post light stimulus the first AP was elicited and averaged across all trials for each stimulus protocol. It was found that the mean evoked response latency across all morphological cell types for the 0.4 Hz, 1.96 Hz and 9.09 Hz stimulus was 5.81 ± 0.38 ms, 7.36 ± 0.45 ms, 8.28 ± 0.41 ms respectively. Eight-eight percent of the present sample (45 of 51) responded with an AP during the 10ms while the light stimulus was on. L4sp neurons displayed the fastest mean evoked onset response latency of 4.12 ± 0.66 ms, but significantly increased to 8.14 ± 1.48 ms during the 9.09 Hz stimulus protocol (n = 3, two-sided t-test, paired: P = 0.03). This may not be an accurate representation due to the small sample size, only a single L4sp had mean evoked response latency below 3 ms post light stimulus (2.72 ± 0.06 ms). For the interneurons, they were observed to have the second fastest evoked response latencies with a mean response time post stimulus of 4.48 ± 0.64 ms and also significantly increased to 8.65 ± 0.62 ms during the 9.09 Hz stimulus protocol (n = 15, two-sided t-test, paired: $P < 10^{-5}$). Seven interneurons showed a mean evoked response latency below 3ms with the fastest response time post stimulus of 2.52 ± 0.03 ms. L6CCs mean response latency time post stimulus was 4.86 ± 0.42 ms which also significantly increased to 8.20 ± 0.95 ms during the 9.09 Hz stimulus protocol (n = 5, two-sided t-test, paired: P = 0.003). For the L5STs, the mean response latency post time stimulus was 5.18 ± 0.58 ms however L5STs were the only morphological cell type in the present sample that did show a significant increase in response latencies upon increasing the light stimulus protocol to 9.09 Hz (n = 4, two-sided t-test, paired: P = 0.42). One L5ST did have an evoked response latency time post stimulus below 3ms (2.72 ± 0.06 ms). Finally, L5PTs mean response latency time post stimulus was 6.77 ± 0.51 ms which significantly increased to 8.20 ± 0.95 ms during the 9.09 Hz stimulus protocol (n

=23, two-sided *t*-test, paired: *P* = 0.01). One L5PT had a mean evoked response latency below 3ms (2.77 ± 0.08).

Burst responses to photo stimulated TC synapses.

Neurons that had an evoked onset response or "event" upon light stimulus did so with either a single AP, a doublet burst of APs or triplet burst of APs (see Figure 4.3C for examples). Therefore for all neurons with an onset event response, the probability of these events being a doublet AP and triplet AP event response was determined for all trials across all stimulus protocols (Figure 4.5). For the three responding L4sp, 1 neuron responded with a triplet burst event in only a single trial in each stimulus protocol. The other 2 L4sp neurons responded mostly with single APs and only a probability of 0.05 ± .03 for doublet burst event responses. For the L5STs, only two of the responding neurons were observed responding with doublet AP bursts while the other two responding L5ST responded with single APs across all stimulus protocols. For the L6CCs, again two neurons were observed responding with doublet APs but only during the 0.4 Hz and 1.96 Hz but then only responding with single APs during the 9.09 Hz stimulus protocol. For the interneurons, eleven neurons responded with at least a triplet bursts of APs during the 0.4 Hz stimulus protocol. The triplet burst event probability was found to be 0.51 ± 0.12 during the 0.4 Hz stimulus protocol but decreased significantly to 0.17 ± 0.06 during the 9.09 Hz protocol (*n* =15, two-sided *t*-test, paired: *P* = 0.004). For the L5PTs, only a single neuron was observed to respond with a triplet AP burst in seven out of thirty trials during the 0.4 Hz protocol. The other twenty-one responding L5PTs responded with either single APs or doublet AP bursts. Interestingly however, a total of six L5PTs began

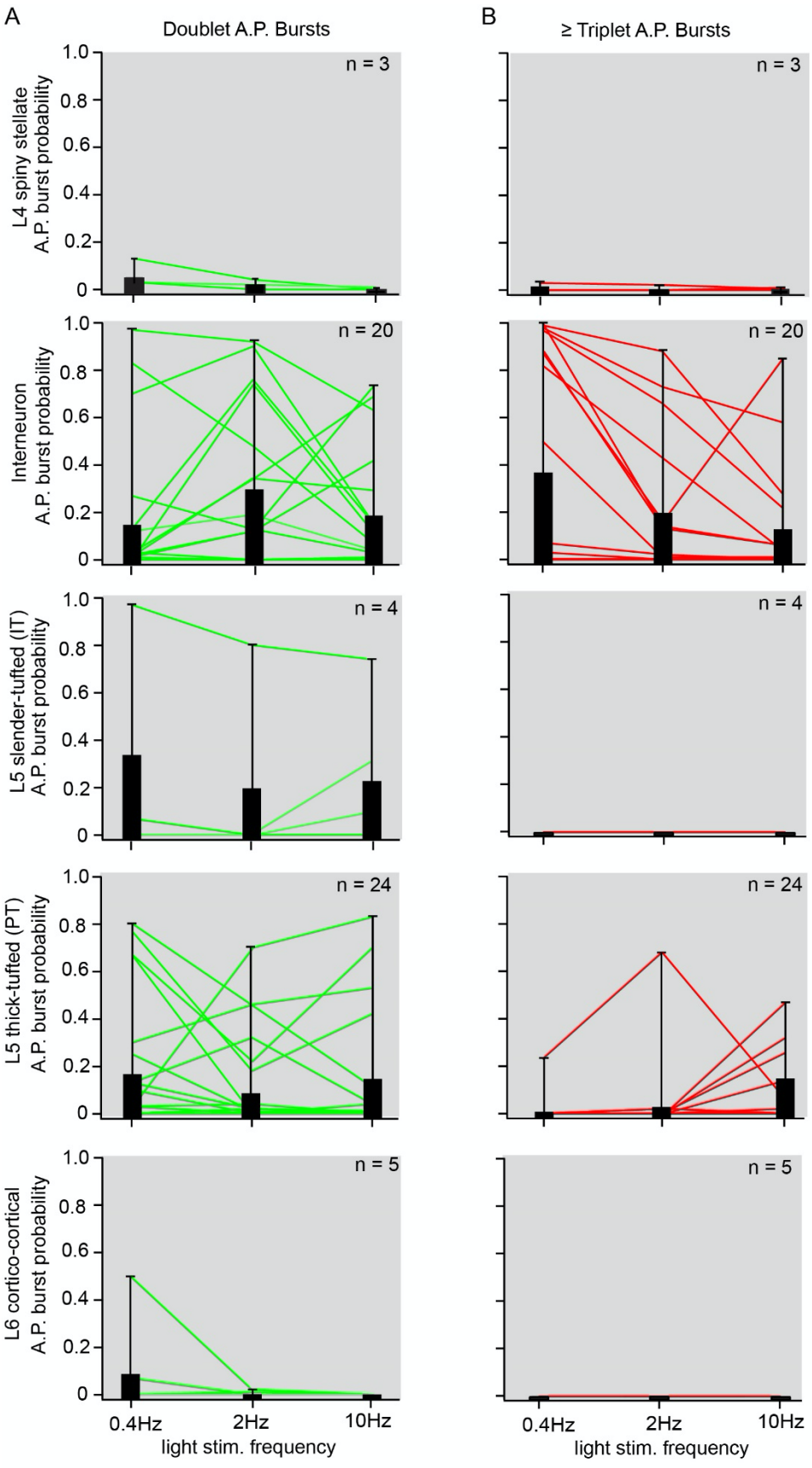
A
Doublet A.P. Bursts
B
≥ Triplet A.P. Bursts
L4 spiny stellate
A.P. burst probability
Interneuron
A.P. burst probability
L5 slender-tufted (IT)
A.P. burst probability
L5 thick-tufted (PT)
A.P. burst probability
L6 cortico-cortical
A.P. burst probability
n = 3
n = 20
n = 4
n = 24
n = 5
1.0
0.8
0.6
0.4
0.2
0
0.4Hz
2Hz
10Hz
light stim. frequency

Figure 4.5 *(previous page*): Cell type specific burst responses to photo stimulated TC synapses: (A) The probability for each recorded neuron that displayed an evoked event (see figure 4.4A) to respond with a doublet AP burst to each of the three photo stimulation protocols and grouped by morphological cell type. AP doublet burst probabilities were calculated by the number of evoked events that were observed to be doublets (see Figure 4.3C for examples) and divided by the number of stimulation trials in each photo stimulation protocol. Green thin bars represent individual neurons. Thick vertical bars represent the population mean and thin vertical bars represent the maximum range. (B) Same as in panel A, but probabilities that each neuron grouped by morphological cell type responded with a triplet burst of APs during each of the three photo stimulation protocols. Red horizontal lines represent individual neurons. Thick vertical bars represent the population mean and thin vertical bars represent the maximum range.

to show triplet AP burst responses during the 9.09 Hz stimulus protocol. Although not significant, the triplet AP burst probability increased from 0.01 ± 0.01 during the 0.4 Hz stimulus protocol to 0.06 ± 0.02 during the 9.09 Hz protocol contrasting to the triplet AP burst probabilities observed for the interneuron population (n =23, two-sided t-test, paired: P = 0.11).

4.1.2 Structural organization of TC inputs on dendrites of excitatory neurons in vS1.

The dendrites of ten of the twenty-five in vivo recorded L5PTs were fully reconstructed and the densities of virus labeled primary TC inputs were quantified. These ten L5PTs were chosen for reconstruction and TC input quantification because they displayed the highest quality biocytin labeling and dendritic spines were easily identifiable. After each L5PT was reconstructed, each spine along the complete L5PT dendritic tree was manually inspected and a landmark was placed where a spine head made contact with a virus labeled TC bouton using dual channel 3D confocal image stacks representing the biocytin labeled neuron and the virus labeled TC synapses (Figure 4.6). The generation of the landmarks representing putative TC synapses and alignment of landmarks with dendrite reconstructions were done using Amira visualization software. Tissue sections representing the basal dendrites near to the soma and along the apical dendrite in layer 4 and layer 2/3 were additionally immune-labeled with vesicular glutamate transporter 2 antibody (VGlut2) and imaged using a super-resolution confocal laser microscope. The dendritic spines putatively identified as TC synapses located within these representative tissue sections were then checked for co-localization of a virus labeled TC bouton and antibody labeled primary thalamic glutamatergic neurotransmitter (VGLut2) (see Figure 4.6A and 4.7A for example images). After all dendritic spines were completely inspected for putative TC synapses, the density and distribution of the putative TC synapses were then quantified. The landmarks representing the putative synapse were aligned with the reconstructed dendritic tree and

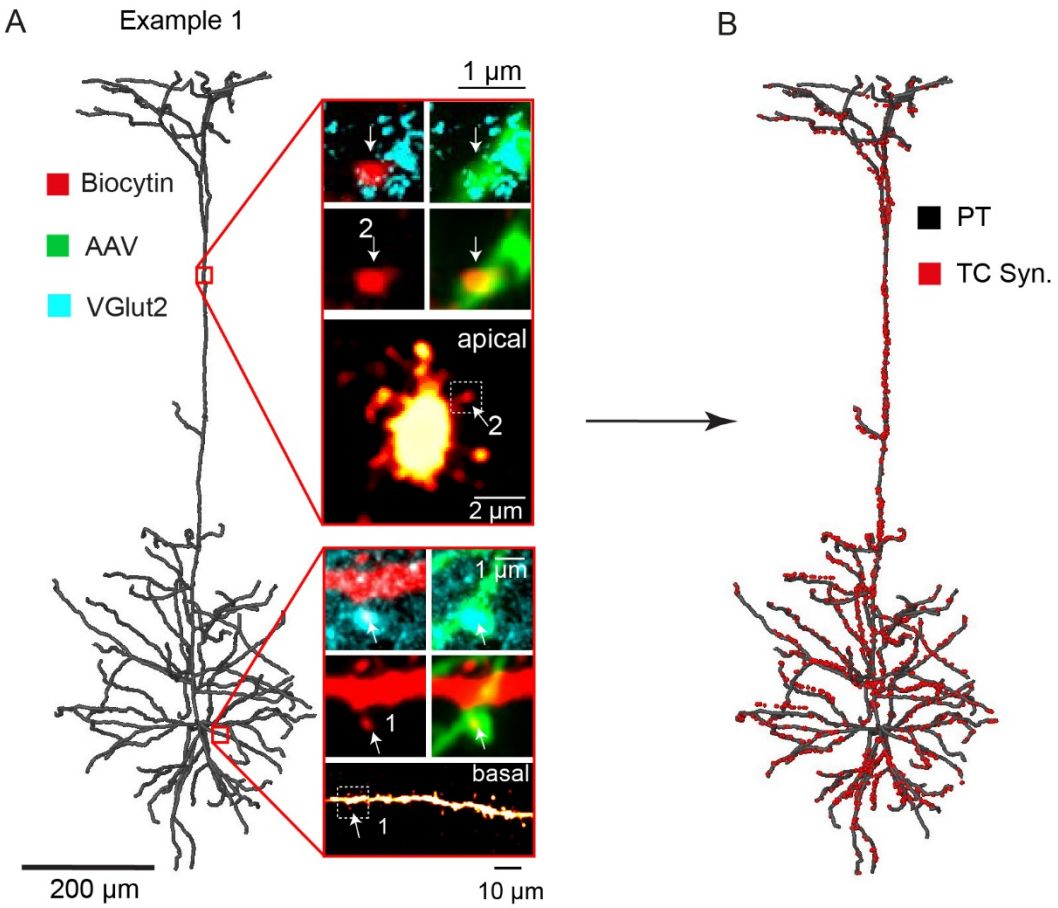

Figure 4.6: Manual inspection of biocytin labeled spines of L5PTs for rAAV labeled primary TC inputs. (A) Left: Exemplary example of a complete dendrite reconstruction of an in vivo recorded a biocytin labeled L5PT in vS1. Right bottom: Exemplary deconvolved confocal image of a basal dendrite branch illustrating spine quality labeling. (bottom) Super resolution image zoom-in on a basal spine head that overlaps with a rAAV labeled TC bouton and co-localizes with VGlut2. Illustrates a putative TC synapse in the basal dendrites. Red channel represents the biocytin labeled dendrites/spines of the L5PT, Cyan represents the VGlut2 signal, and Green represents the rAAV labeled TC boutons. (B) The same dendrite reconstructed morphology as in panel A illustrating the results of manual inspection of all spine heads and placing markers on spine that overlap with rAAV labeled TC boutons. Red markers represent the locations of putative TC synapses.

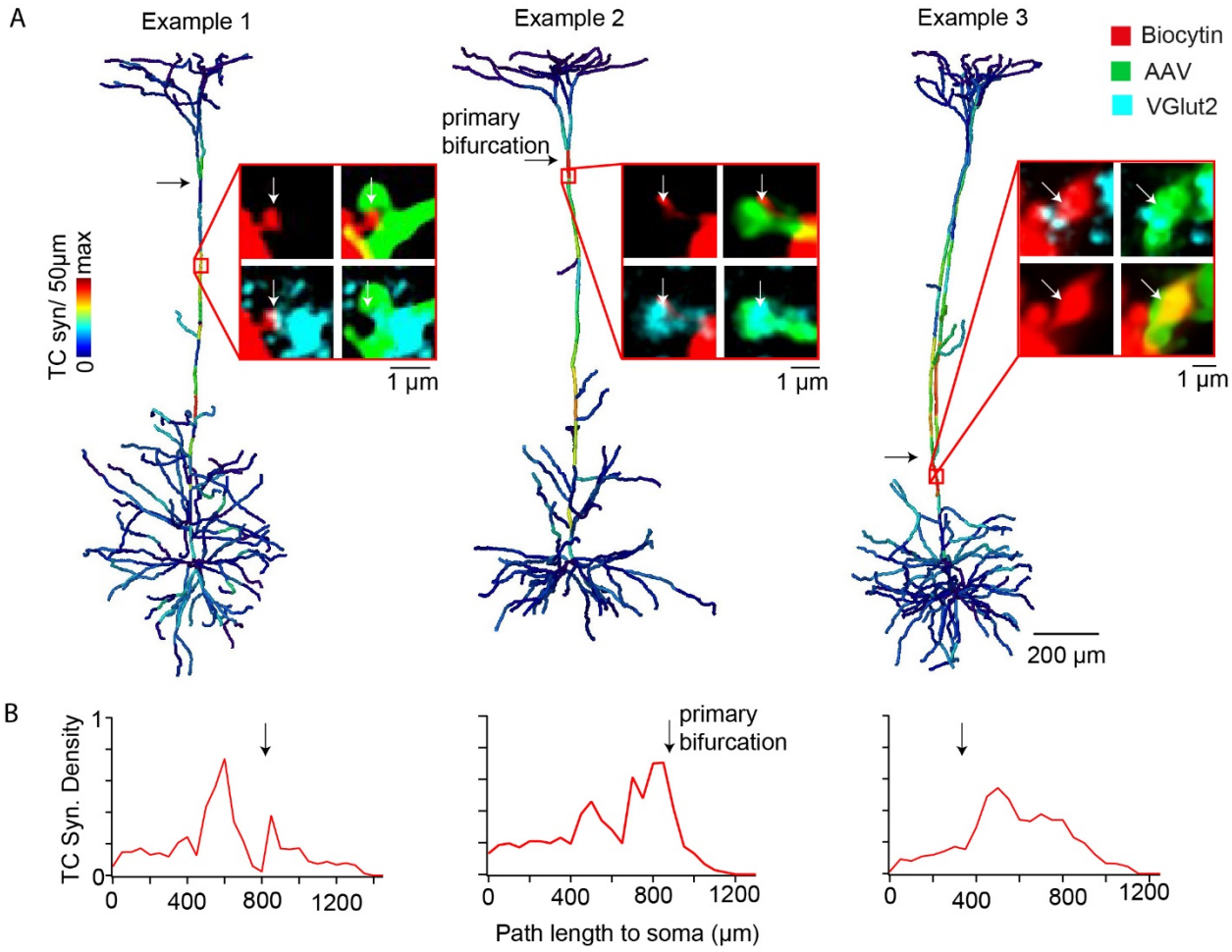

Figure 4.7: Quantification of primary TC input density on the dendrites of L5PTs. The number of dendritic spine heads that overlapped with a rAAV labeled bouton was divided by dendritic pathlength to measure the distribution of putative TC synapses through the dendritic arbor. The TC putative synaptic density was measured along each individual dendritic branch in bin sizes of 50 um of dendrite pathlength. (A) Putative TC synapse densities visualized on the dendrite reconstructions as heat maps to illustrate the difference in densities between the basal dendrites and the apical dendrites for 3 example L5PTs. The image zoom-ins represent super resolution confocal images to show example putative TC synapses along the apical trunk dendrite that also co-localize with VGlut2. Black arrows on the L5PT dendrite morphology mark the apical dendrite primary bifurcation. (B) Putative TC synapse density measurements with respect to distance from the soma shown as histograms. Bin size is 50 um. Black arrows illustrate the location of the apical dendrite primary bifurcation distance with respect to the soma.

moved to the closest point on the reconstruction (Figure 4.6B). The path length distance was calculated from the landmark location along the reconstructed dendrite to the soma. The densities of putative TC synapses were then measured for each dendritic branch in bin sizes of 50 μm and displayed as a heat map on the dendritic reconstruction and plotted as a histogram with respect to distance to the soma. (Figure 4.7 and 4.8). For morphological comparison the same procedure was then repeated for a single L4sp, L5IT, and L6CC (Figure 4.12).

Primary TC synapse density is significantly higher in apical dendrites than basal dendrites of L5PTs

The dendrite morphologies of ten L5PTs recovered from in vivo recording experiments of VPM virus injected rats were reconstructed. The mean total dendritic length was similar to previous reports for L5PTs (mean ± SD: 13.69 ± 3.05 mm, n = 10) [73], [22]. The results of mapping primary TC inputs onto the dendrites of the in vivo labeled L5PTs reveals they receive on average 1,325 ± 597 (mean ± SD, n = 10) synapses from neurons located in the VPM. The mean primary TC synaptic density with respect to the complete dendritic tree was determined to be 0.10 ± 0.05 TC synapses per 1μm of dendritic path length (mean ± SD, n = 10). The primary TC synaptic density was then measured separately for the apical dendrites and the basal dendrites. It was determined that the TC synaptic density for all ten L5PTs was significantly higher in apical dendrites than when compared to the basal dendrites (n =10, two-sided t-test, unpaired: P = 0.001).

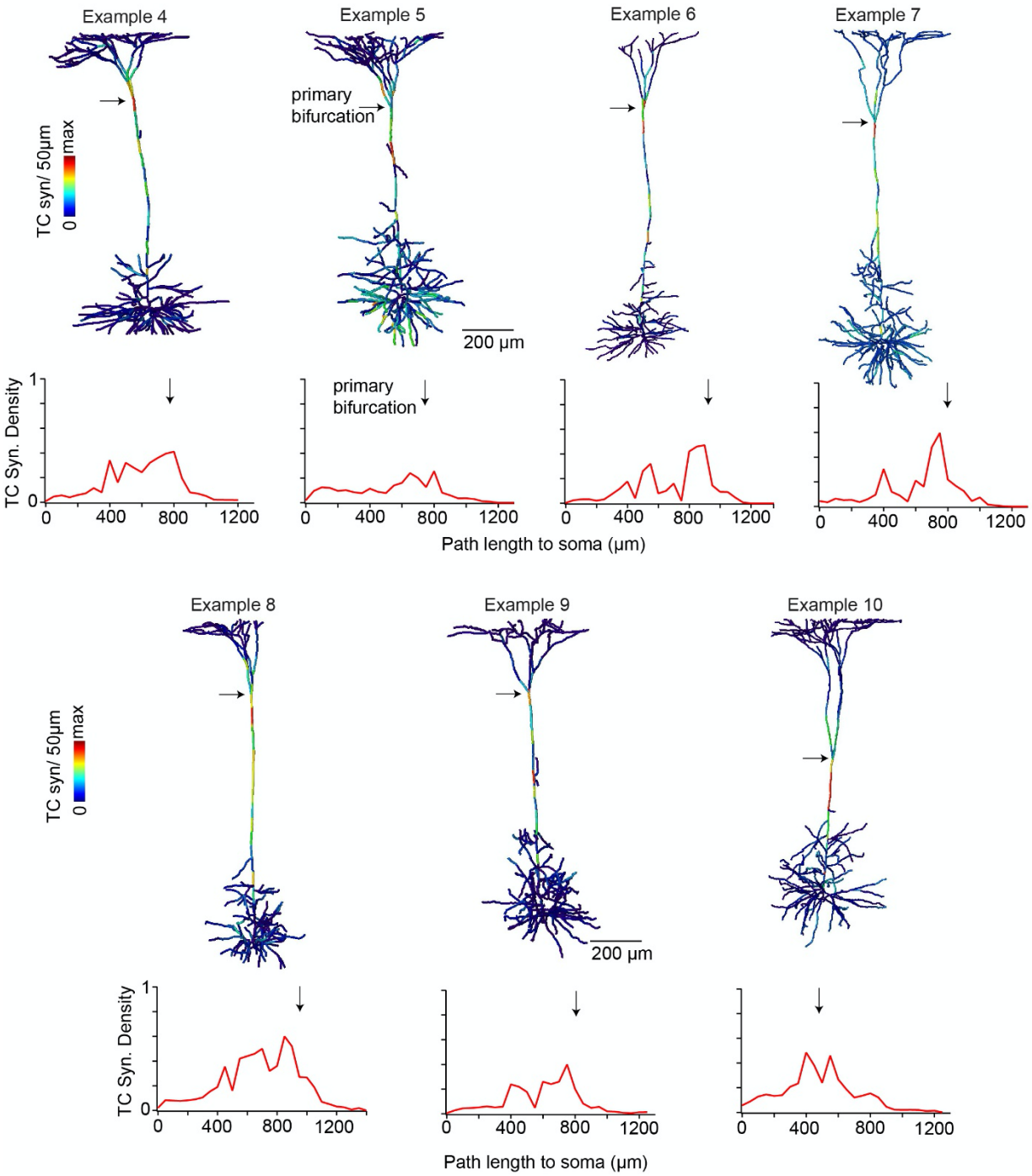

Figure 4.8 VPM neurons form a dense hot zone of connections on the distal apical trunk of L5PTs: Putative TC synapse density distributions were quantified for seven additional L5PTs as shown in Figure 4.7. Peak putative TC density was consistently observed on the apical trunk near the primary apical dendrite primary bifurcation.

Neurons in the VPM form a "hot zone" of synaptic connections

For each L5PT the density of primary TC input was measured in 50μm bins along each segment of dendrite and then visualized as a heat map (Figure 4.7A and Figure 4.8A). Next, the distance to the soma of all 50μm bins representing TC synaptic density along each dendritic segment was measured in order to quantify the distribution of TC synaptic density with respect to distance to the soma Figure 4.7B and 4.8B. Surprisingly, for all ten L5PTs quantified the primary TC synapses were distributed along the dendritic tree in a manner that resulted in a peak density area that was always located along the apical dendrite and proximal to the primary apical dendrite bifurcation (Figure 4.9). This peak area of TC synaptic density is referred to as a primary "TC hot zone" and is defined as the 50 μm bin with the highest primary TC synapse density.

The distance from the soma to the TC hot zone for each L5PT was measured. The mean soma to TC hot zone distance was determined to be 702.50 μm (median: 725 μm, range: 425 – 900 μm, n = 10). Next, the distance from the soma to the location of the apical dendrite primary bifurcation was measured. The mean soma to primary apical dendrite bifurcation distance was determined to be 730.04 μm (median: 784.22 μm, range: 260.25 μm – 955.74 μm, n = 10). Finally the distance from the location of the TC hot zone to the primary apical dendrite bifurcation was measured. The mean distance between the TC hot zone and apical dendrite primary bifurcation was determined to be 96.72 μm (median: 67.08 μm, range: 19.56 – 230.73 μm, n = 10). Therefore, neurons in the VPM that provide primary thalamic input to vS1 form a dense area or hot zone of synaptic connections to a specific area on the apical dendrite of L5PTs that is strongly

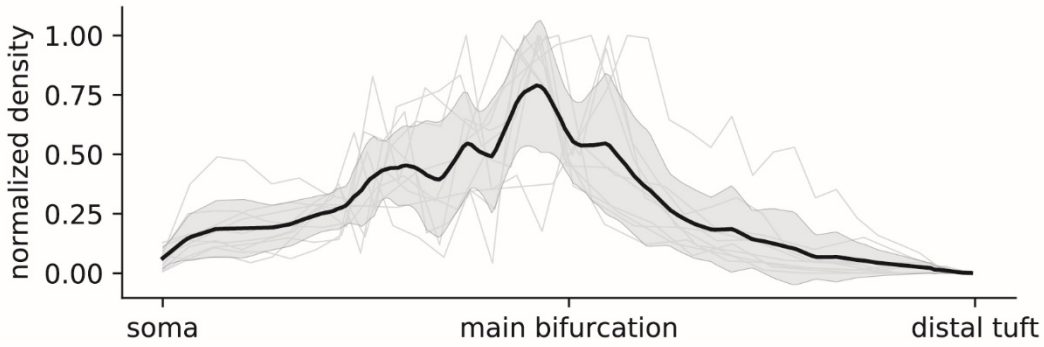

Figure 4.9: VPM neurons form a dense hot zone of synaptic connections on the distal part of the apical dendrite of L5PTs. The soma distance to the primary bifurcation as well as the most distal apical tuft dendrite was calculated (n = 10). Each profile was normalized by linearly scaling the interval (0; main bifurcation distance) to (0,1) and the interval (main bifurcation distance; most distal apical tuft dendrite) to (1,2). Furthermore, the peak of each profile was normalized to 1. The thin grey lines represent the normalized profile for each individual L5PT. The thick black line represents the mean. The shaded area represents the standard deviation.

correlated to the location of the primary apical dendrite bifurcation (n = 10, Pearson: R = 0.80, P =0.005) (Figure 4.10).

Wiring specificity between VPM neurons and L5PTs

It has been previously reported that spine densities are significantly higher along the apical trunk than in the basal dendrites of L5PTs [74]. To determine if the observation of the TC hot zone is a result of neurons in the VPM specifically targeting the apical dendrite or just a result of significant increases in number spines in these areas, apical and basal dendrite spine densities were measured for all ten L5PTs in the present sample. For each L5PT where primary TC synapses were quantified, spines were counted on

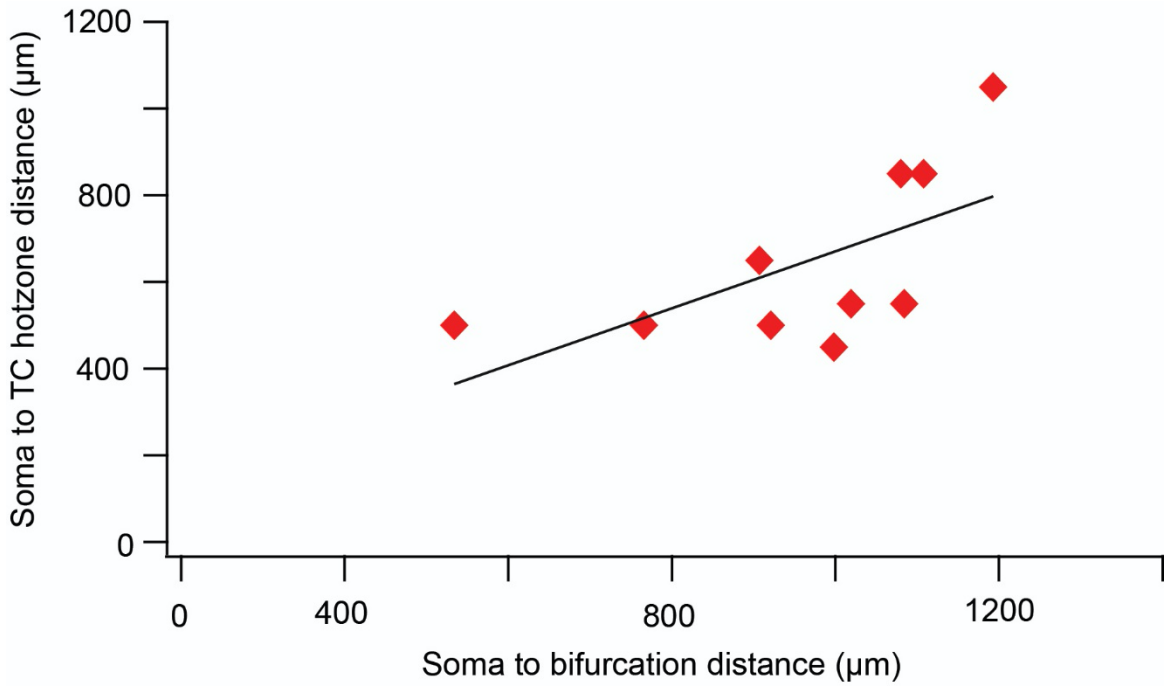

Figure 4.10: TC hot zone correlates with the primary apical dendrite bifurcation. The distance from the soma to the location of the apical dendrite bifurcation was quantified with respect to the distance to the TC hot zone location. Distances of both locations measured from the soma were significantly correlated (n = 10; Pearson: R =0.8).

three randomly chosen 50µm basal dendritic segments, a single 50 µm segment of the apical trunk in layer 4 and a 50 µm apical trunk segment at the location of the TC hot zone, in order to determine the number of spines per 1 µm of dendritic path length. The primary TC synapse densities were then divided by the number of spines counted to determine the number of TC synapses per spines for the sample dendritic segments (Figure 4.11).

The mean spine density in the basal dendrites was found to be 1.03 ± 0.04 spines per 1 µm (n = 30). The mean spine density significantly increased along the apical trunk in L4 by 130% to 2.37 ± 0.19 spines per 1 µm (n = 10, 2 side t test unpaired: $P < 10^{-5}$).

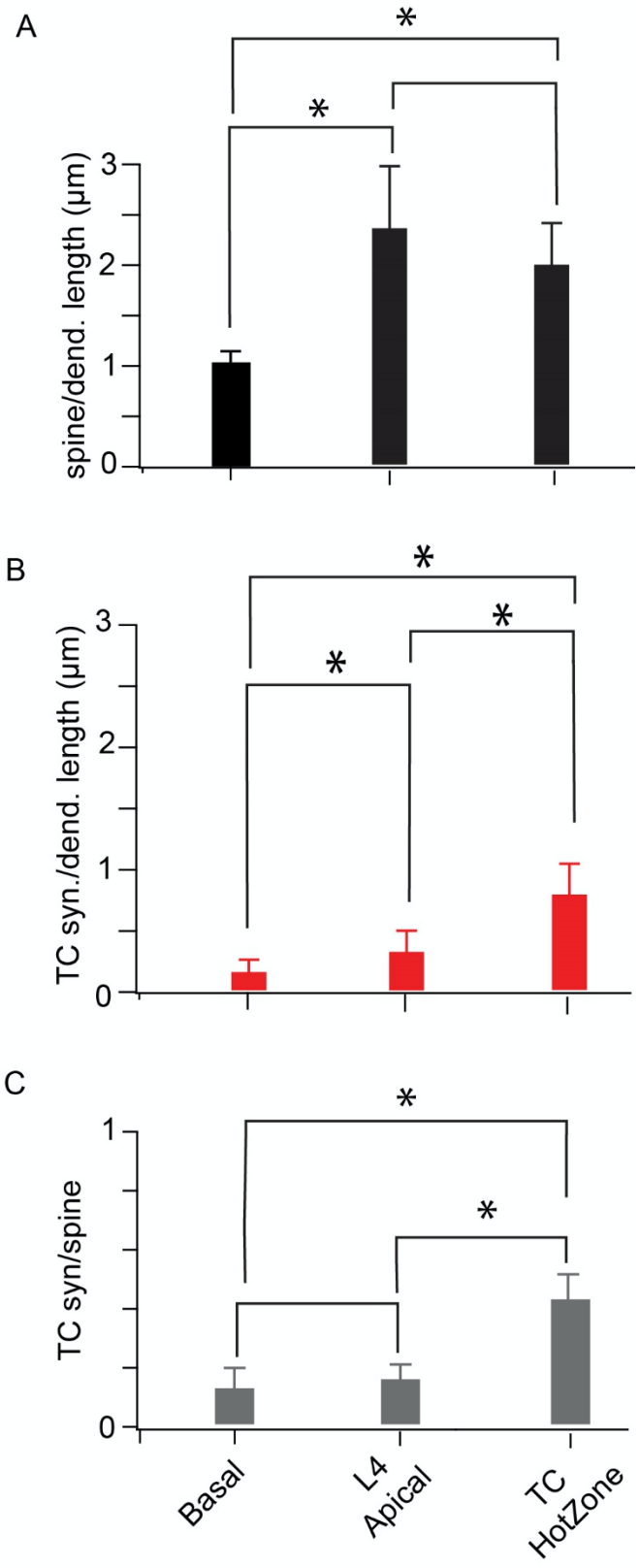
A
*
*
spine/dend. length (µm)
3
2
1
0
B
*
*
*
TC syn./dend. length (µm)
3
2
1
0
C
*
*
TC syn/spine
1
0
Basal
L4
Apical
TC
HotZone

Figure 4.11 (*previous page*): VPM neurons specifically target the apical dendrite near the primary bifurcation of L5PTs. (A-C) Spine densities, TC densities and TC putative synapses per number of spines in the basal, apical trunk in L4 and apical trunk at the location of the TC hot zone on the apical trunk of L5PTs. Thick bars represent the mean and error bars represent the SEM. (A) Spine densities in the apical trunk were observed to be significantly higher than in the basal dendrites. (B) TC synaptic densities were observed to be significantly higher on the apical trunk than in the basal dendrites. (C) The number of TC synapses were quantified per number of dendritic spines for the basal, apical trunk in L4 and the apical trunk at the location of the TC hot zone. The number of TC synapses per spines in the apical trunk in L4 was not significantly different when compared to the basal dendrites. The number of TC synapses per spines at the location of the TC hot zone was significantly higher when compared to the basal dendrites and the apical dendrite in L4.

The mean spine density along the apical dendrite at the location of the TC hot zone across all ten L5PTs was found to be 1.99 ± 0.13 spines per 1 µm (n = 10), a significant increase by 93% from the mean spine density observed in the basal dendrites (n = 10, 2 sided t test, unpaired: P = 0.0002).

For the same dendritic segments where spines were counted, the mean TC synapse density in the basal dendrites was found to be 0.13 ± 0.02 putative contacts per 1 µm (n = 30). The mean TC synapse density along apical trunk in layer 4 increased significantly to 0.34 ± 0.05 putative contacts per 1 µm (n = 10, 2 side t test unpaired: P = 0.0014). The mean TC synapses density at the dendritic location of the TC hot zone was found to be 0.81 ± 0.8 putative contacts per 1 µm, a significant increase from the basal dendrites and layer 4 apical trunk of 523% and 138% respectively (n = 10, 2 sided t test, unpaired: $P < 10^{-5}$).

Next the number of TC synapses per number of spines was determined for all dendritic segments sampled. It was found that the mean number of TC synapses per number of spines in the basal dendrites was 0.13 ± .02 (n =30). There was no significant increase observed in the number of TC synapses per spine along the apical trunk in layer due to the large increase in spine density for this dendritic segment (n = 10, 2 sided t test, unpaired: P = 0.62). However, the mean number of TC synapses per number of spines did increase significantly along the apical dendrite in the area of the TC hot zone to 0.41 ± .04 (n = 10, 2 sided t test, unpaired: $P < 10^{-5}$). This suggests the TC hot zone that is consistently observed to be located near to the L5PTs primary bifurcation is a result of specific axonal targeting by neurons located in the VPM and not due to significant increases in spine densities along the apical trunk (Figure 4.11C).

Organization of primary TC input on the dendrites of other excitatory neurons in vS1

The above procedure to quantify the density and distribution of primary TC inputs on the dendrites of in vivo labeled L5PTs was additionally repeated for one example L4sp, L5IT, and L6CC (Figure 4.12). Similarly as previously reported, the total dendritic length was measured to be 2756.73 µm, 6960.90 µm, and 8260.17 µm for the L4sp, L5IT, and L6CC respectively [73]. For the L4sp, 504 putative primary TC synapses were identified, yielding a synapse per 1 µm dendritic length density of 0.18. This was higher than the mean primary TC synaptic density observed for the dendrites of L5PTs however for the single L4sp the peak density was much closer to the soma at a distance of approximately

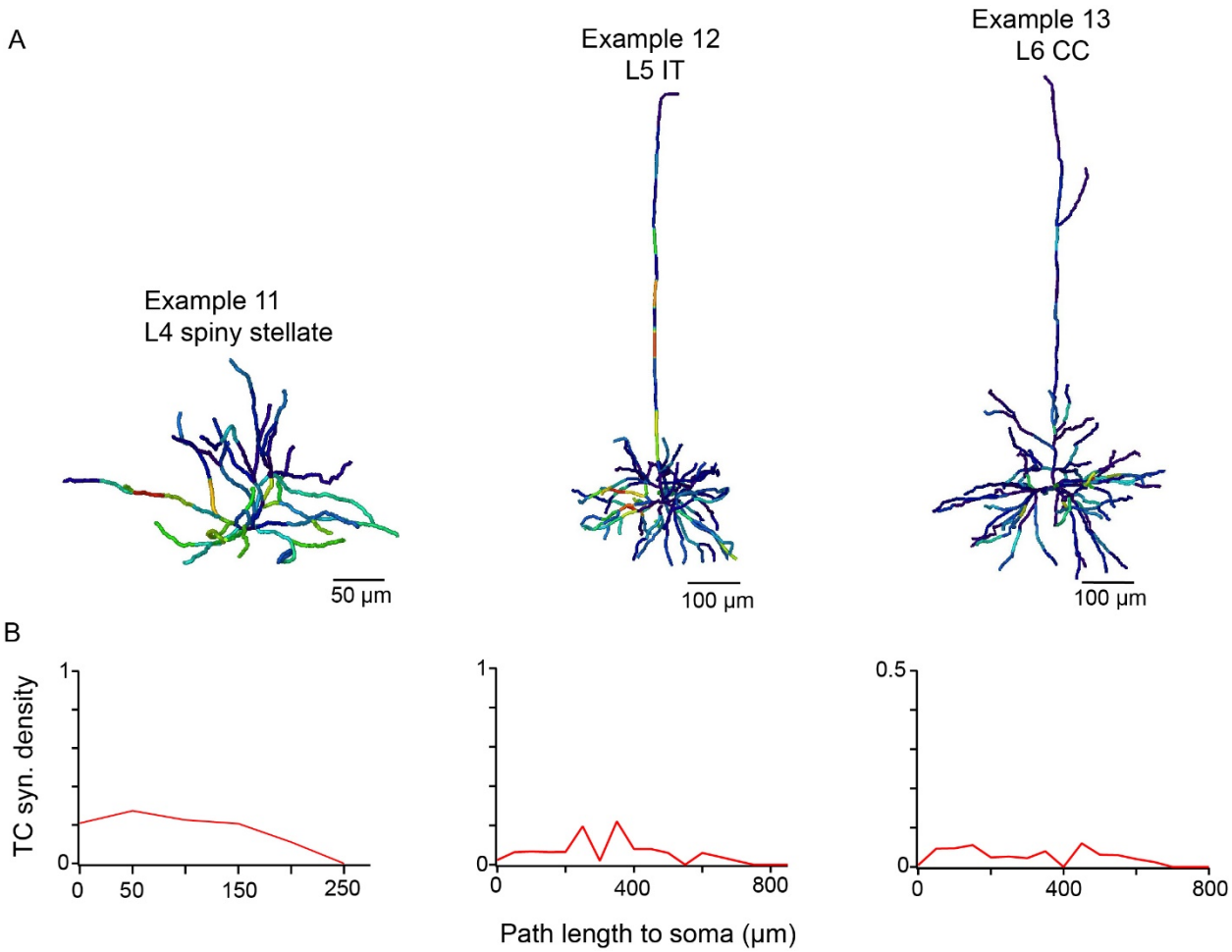

Figure 4.12: Quantification of TC input on the dendrites of other excitatory cell types. (A-B) Same quantification of putative TC synapses as done for the L5PTs, were repeated for 1 exemplary L4 spiny stellate, 1 L5IT, and 1 L6CC. (A) Each spine head was manually inspected for overlap with a rAAV labeled bouton. The density of putative TC synapses per 1 um of dendrite for each individual dendritic branch in bin sizes of 50 um. The densities are then shown as heat maps on the dendrite morphology reconstruction. (B) Putative TC synapse density measurements with respect to distance from the soma shown as histograms. Bin size is 50 um.

50 μm. For the single L5IT, the total number of putative primary TC synapses identified was 446 which yielded a synaptic density of 0.06 TC synapses per 1 μm of dendritic length. The TC synaptic density was slightly lower in the apical dendrites than the basal dendrites at 0.05 and 0.07 respectively. There was however a peak TC density observed along the apical trunk at a distance of 350 μm from the soma. Finally for the single L6CC, a total of 324 putative primary synapses were identified which yielded the lowest TC synaptic density when compared to the other morphological cell types of 0.04 TC synapses per 1 μm of dendritic length.

4.2 Structural and functional properties of L5 pyramidal tract neurons

The following description is adapted from Rojas-Piloni, Guest et al. 2017 [22]. Experiments to retrogradely label L5PTs and in vivo recordings were carried out by Gerardo Rojas-Piloni (Max Planck Florida Institute for Neuroscience).

Pyramidal tract neurons (PTs) located in layer 5 represent the major output cell type of the neocortex. Through long-range projecting axons, L5PTs broadcast results of cortical processing to specific groups of subcortical brain areas. Here to exam the principles of how processed cortical information is broadcast to downstream targets, ongoing AP activity and sensory evoked responses of L5PTs were recorded in vivo whose long-range axonal targets were identified by retrograde tracer injections. In the previous chapter I reported that retrograde tracer injections into the Pom, Pons, SC, and SP5C resulted in labeling of different populations of L5PTs within vS1. The retrograde tracer injections also revealed that each subcortical target receives input from different cortical areas but always from L5B in vS1. The results from quantifying the number and distribution of retrogradely labeled L5PTs revealed that the majority of L5PTs in vS1 project to only one of the four subcortical targets investigated and their peak densities in L5 form target related overlapping sub layers (i.e. peak densities of Pom and SC projectors were 100 μm more superficial than Pons and SP5C projectors.

In the following section I will describe empirical evidence that L5PTs have dendrite distributions, soma depth, and electrophysiological properties that not only reflect their

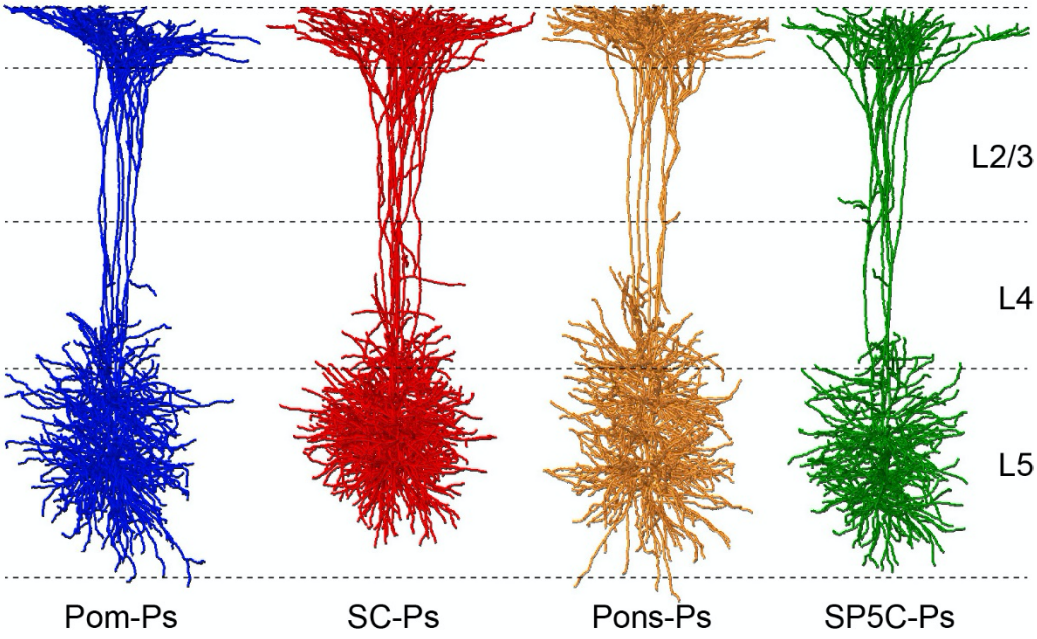

Figure 4.13: L5PT dendrite morphology according to subcortical target. 3D reconstruction of in vivo labeled L5PTs with identified subcortical target (n = 5 for Pom/SC/Pons projectors, *n* = 4 for SP5C projectors). L5PTs were registered to a geometrical reference frame of rat vS1 with a 50 um precision. Figure is adopted from [22]

long-range axonal targets but taken together are actually predictive of the subcortical brain region L5PTs project to.

4.2.1 Dendrite distributions reflect the subcortical target of L5PTs

The dendrite morphologies of twenty-two L5PTs were reconstructed whose sub-cortical targets were identified by retrograde tracer injections. The tracing results were augmented with reconstructions of the pial surface, white matter tract, and barrel field in layer 4. These anatomical structures were used to register each reconstructed dendritic morphology to a geometrical reference frame of vS1, which allowed determining the 3D soma and dendritic locations with approximately a 50 μm precision (Figure 4.13). It was observed that seven L5PTs had soma locations in layer 5A and fifteen were located in layer 5B. The overall soma depth distributions for the current sample of reconstructed L5PTs (n = 22; range: 913-1244 μm, median: 1090μm) was similar to the overall distribution of Pts in vS1 (range: 900-1300 μm, peak 1119 μm). The soma depth locations were not significantly different between PTs when grouping them by their respective subcortical targets (n = 5/5/5/4 for Pom/SC/Pons/SP5C-Ps; one-way ANOVA: P = 0.76).

The dendrite distributions of L5PTs along the vertical cortex axis within the cortical layers were observed to be different across L5PTs with different axonal target areas (Figure 4.14). In order to quantify this observation, the dendritic path length and the branch points that each population of L5PTs contributed to L1, L2/3, L4, L5A, L5B, respectively were calculated. Dendritic path lengths correlated significantly with the respective number of branch points within and across layers (n = 22, Pearson: $R > 0.84$, $P < 10^{-5}$) (Figure 4.15). Dendrite distributions of Pom projecting L5PTs were significantly

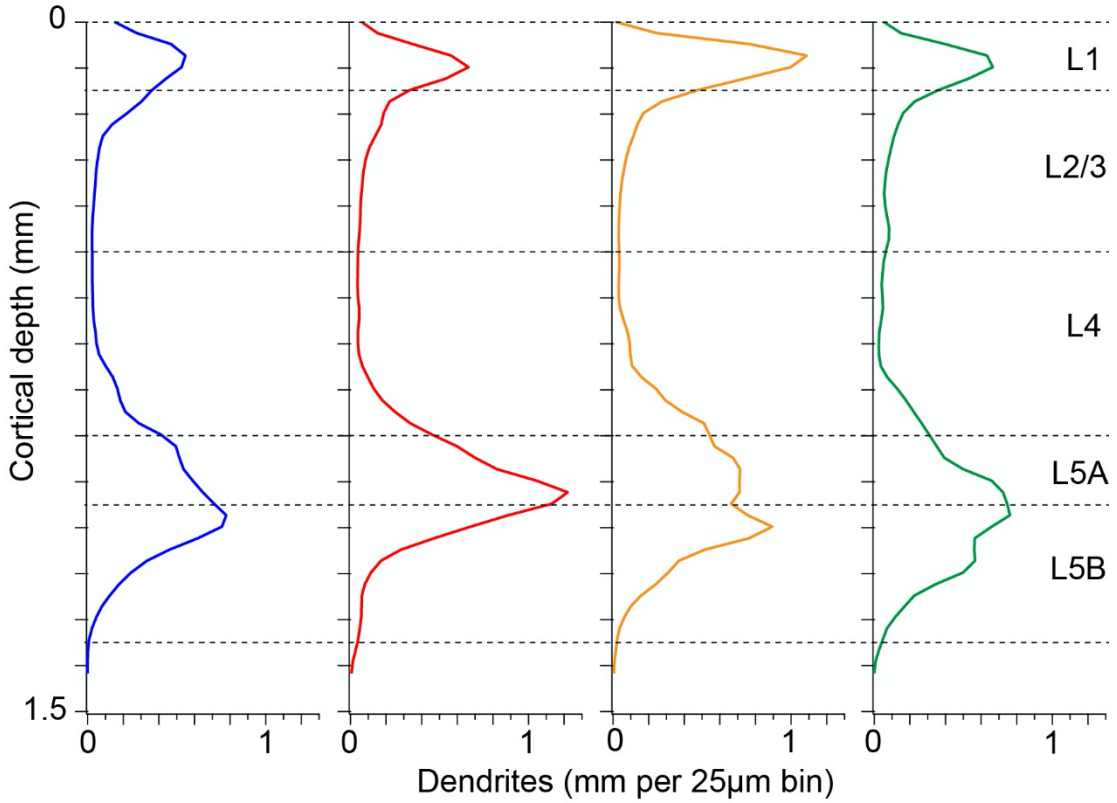

Figure 4.14: Laminar distributions reflect subcortical targets of L5Pts. Distribution of dendrites along the vertical cortical axis, averaged across the L5PTs shown in Figure 4.13. Figure is adopted from [22]

less complex (i.e. quantified as path length times the number of branch points) than L5PTs with different targets (n = 22; two-sided t-test of dendritic complexity distributions along the vertical cortex axis: $P < 0.002$). These differences were primarily due to significantly less dendrites/branch points within L5A (n = 22: two-sided t-test: $P < 0.007$). In contrast, S.C. projecting L5PTs had more complex dendrite distributions within L5A, compared to L5PTs with different targets (n = 22: two-sided t-test: $P < 0.04$), and less

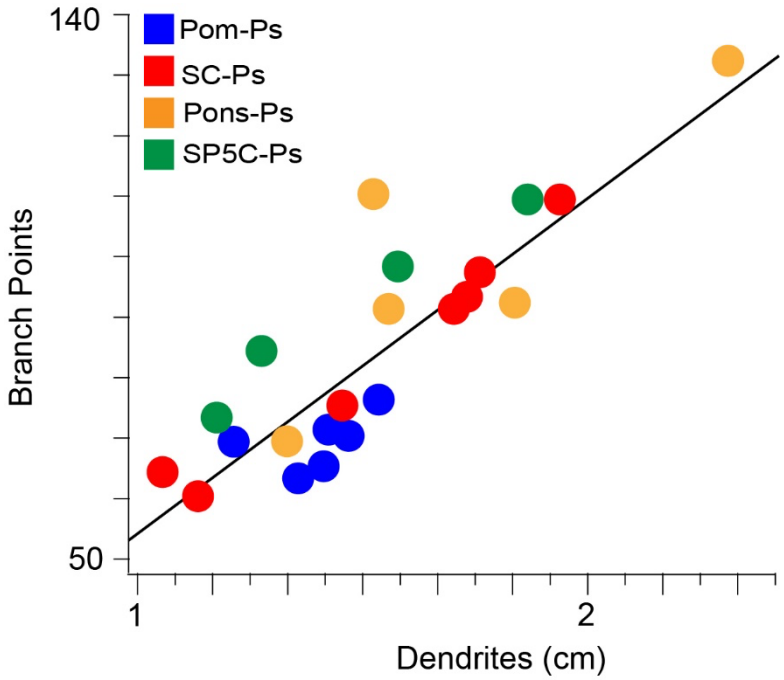

Figure 4.15: Dendritic path length and branch points are correlated. The number of dendritic branch points were plotted against the dendrite path lengths with respect to each target group. Dendritic path length per L5PT is significantly correlated to the respective number of branch points. Markers with two colors represent L5PTs that project to two targets. Figure is adopted from [22]

complex distributions within L5B (n = 22: two-sided t-test: $P < 0.001$). Pons projecting L5PTs had the most complex dendritic distributions within L1 (n = 22: two-sided t-test: $P < 0.001$). Finally SP5C projecting L5PTs had the least complex dendritic distributions in L4 compared to L5PTs with other targets (n = 22: two-sided t-test: $P < 0.07$).

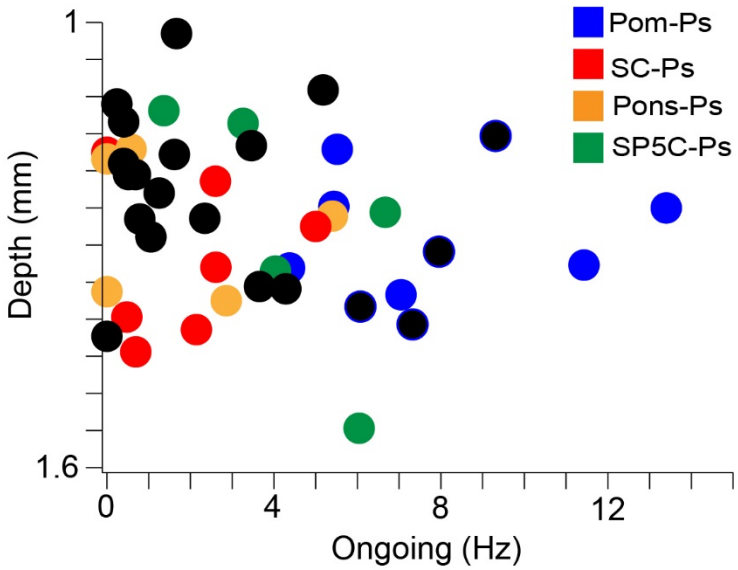

Figure 4.16: Recording depth versus ongoing AP rate of L5PTs. AP rates during recording periods without whisker stimulation (ongoing AP rate) were plotted against the measured recording depth. Black markers represent L5PTs whose targets could not be identified (soma did not co-localize with any retrograde tracer). Markers with two colors represent L5PTs that project to two targets. Figure is adopted from [22].

4.2.2 Ongoing AP rates reflect the subcortical axonal target of L5PTs

Several previous studies have associated L5PTs with the property of intrinsic bursting [25]. In line with these assessments [46], we found that in the current sample of L5PTs, the majority of L5PTs spiked in bursts of action potentials (APs; 100 Hz 37/43; 200 Hz: 29/43) during periods of ongoing activity. The fraction of ongoing APs that were elicited as bursts was independent of the respective subcortical axonal target (*n*= 5 for

each L5PT group; one-way ANOVA 100Hz: P = 0.31; 200 Hz: P = 0.18). Ongoing AP rates in the present sample of L5PTs (n = 43) were in line with those reported previously [34], [46] and were not found to be significantly different for the subset of L5PTs whose subcortical axonal targets had been identified (n = 22: two-sided t-test: P < 0.29). However, ongoing AP rates were found to reflect the subcortical axonal target region of L5PTs (Figure 4.16). Pom projecting L5PTs were on average significantly more active than L%PTs with different targets (n = 22: two-sided t-test: P < 0.05). SC and Pons projecting L5PTs had similarly low ongoing AP rates, rendering them the least active L5PTs in vS1 (n = 20: two-sided t-test: P < 0.004). SP5C projecting L5PTs had intermediate ongoing AP rates that were lower than those of Pom projectors and higher than L5PTs that projected to the SC and Pons.

4.2.3 Structure-function relationships predict subcortical targets of L5PTs

Ongoing spike rates of L5PTs were shown to not be significantly different during anesthetized and awake conditions [35], [46]. Together with the soma depth location in L5B and the layer-specific dendritic distribution, the present data thus reveals three cellular properties which are potentially independent of experimental conditions that reflect the respective subcortical axonal target region of L5PTs in rat vS1. Therefore the probability distributions for predicting the respective long-range targets based on each of these three properties were calculated respectively (Figure 4.17A). The resultant

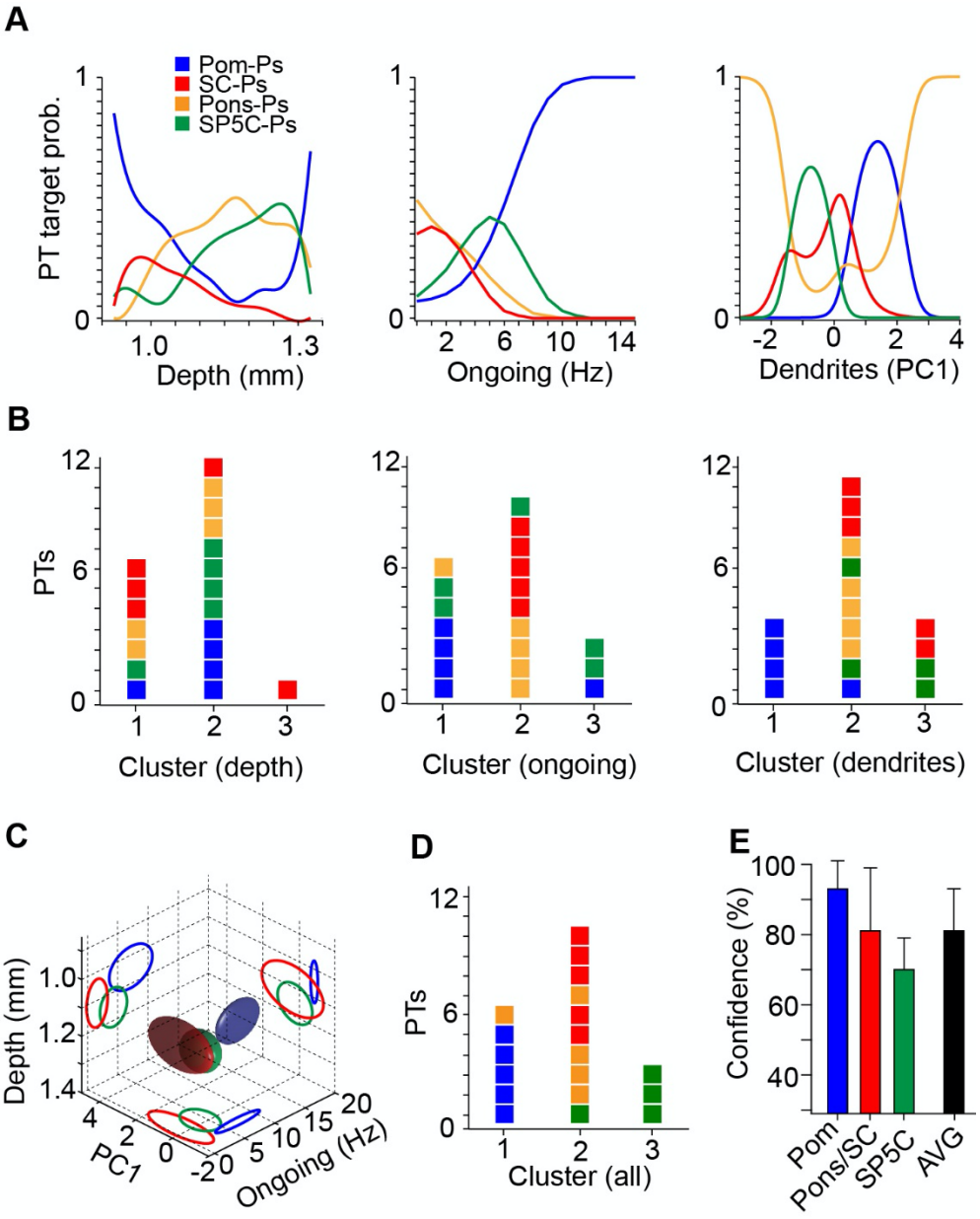
A
Pom-Ps
SC-Ps
Pons-Ps
SP5C-Ps
PT target prob.
1
0
1.0
1.3
Depth (mm)
2
6
10
14
Ongoing (Hz)
-2
0
2
4
Dendrites (PC1)
B
PTs
12
6
0
1
2
3
Cluster (depth)
Cluster (ongoing)
Cluster (dendrites)
C
Depth (mm)
1.0
1.2
1.4
4
2
0
-2
PC1
0
5
10
15
20
Ongoing (Hz)
D
PTs
Cluster (all)
E
Confidence (%)
100
80
60
40
Pom
Pons/SC
SP5C
AVG

Figure 4.17 (*previous page*): Structure-function relationships predict subcortical targets of L5PTs. (A) Probabilities that L5PTs project to each of the four subcortical targets, depending on their soma depth location, ongoing AP rate, or dendritic properties (from left to right). (B) Classification of L5PTs by each of the target-related properties yield clusters that are heterogeneous with respect to subcortical targets. (C) Combining the three target-related properties from panel A yields a 3D parameter space, where L5PTs with different targets form a largely non-overlapping ellipsoids that represent the means ± SDs across L5PTs with the same target (blue: Pom-projectors, green: SP5C-projectors, red: Pons- and SC-projectors. (D) Classification of L5PTs using all three target-related properties (dual target-projectors are outlined). (E) Confidence of predicting the subcortical target of L5PTs. Figure is adopted from [22]

probability distributions were target related for each property, but overlapped, as expected from the variability of the respective target related properties. The overlaps prevented unambiguous determination of the long-range axonal target for any of the three properties. As a result, classification if the in vivo recorded and reconstructed L5PTs, based on their soma depth location or AP spike rate or dendrite distributions, failed to identify clusters that were homogeneous with respect to subcortical targets (Figure 4.17B).

Next, the distributions of the three target-related properties were plotted in a joint three-dimensional feature space (Figure 4.17C). It was found that both the soma depth location and dendrite distributions correlate with ongoing AP rates. For example, L5PTs with ongoing AP rates larger than ~5 Hz that are located within the upper sublayer of layer 5B (i.e.as formed by somata of L5PTs with different targets primarily Pom projecting L5PTs., whereas those with lower ongoing AP rates project their long-range axon either

to the SC or Pons. Analogously in the lower sublayer, SP5C projecting L5PTs could be differentiated by higher ongoing AP rates from SC and Pons projecting L5PTs. Consequently, classification based on the combined target-related properties resulted in three clusters, each cluster comprising a L5PT with largely the same subcortical target (Figure 4.17D). Reconstruction of soma depth location and dendrite distribution, when complimented with measurements of the ongoing spike rate, thus allows predicting whether a recorded L5PT in rat vS1 projects its long-range axon to either the SC/Pons, Pom, or SP5C, with a confidence level of more than 80% (Figure 4.17E).

The analysis was repeated for three PTs that were labeled with tow retrograde tracers. One of the dual subcortical target projecting L5PTs innervated the Pom and Pons, two projected the Pom and SC (dual colored markers in Figures 4.16, 4.17, 4.19). Each dual projecting L5PTs had structural and functional properties that were realted to only one of its respective targets. For example morphology, dendrite distribution and ongoing spike rate of the Pom/Pons projecting L5PT were consistent with the respective properties of Pom projecting L5PTs. Consequently, the classification assigned this dual target projecting L5PT to the Pom cluster with a confidence of 80% (Figure 4.17D). Similarly, the properties of both Pom/SC projecting LPTs resembled those of SC projecting L5PTs, resulting in an assignment to the SC cluster with a confidence of 100 and 81% respectively.

4.2.4 Sensory-evoked spiking reflects the subcortical axonal target of L5PTs

Finally it was investigated whether the relationships between soma-dendrite distributions and ongoing AP rate translate into sensory-evoked activity patterns that also reflect a L5PT's subcortical target region. To do so, all facial whiskers were passively deflected along the rostral to caudal axis, by applying a low pressure air puff for 700ms. Stimulus-evoked spiking patterns resembled those reported previously for similar whisker stimuli [30, 32, 54, 75] (Figure 4.18A). During the first 100ms of whisker stimulation, AP rates increased significantly, on average to 7.5 ± 1.1 Hz (n = 43; two-sided t-test, paired $P < 10^{-5}$). Seventy-nine percent of the L5PTs in the present sample (34 of 43) responded with increased AP rates. On the onset of the stimulus. The amplitude of the onset response (i.e. AP rate 0-100 ms post stimulus minus ongoing AP rate) was independent of the long-range target (n = 5 for each L5PT group; one-way ANOVA: P = 48) (Table1). Response probabilities were also not different between L5PTs with different targets. Specifically, the fraction of stimulation trials in which L5Pts increased AP activity at short latencies after the onset of the stimulus was similar to those previously reported [30, 54] and did not depend on the subcortical target (n = 5 for each L5PT group; one-way ANOVA: P = 0.11). Hence, L5PTs responded reliably to the onset of the present stimulus, independent of their respective subcortical target. Following the "onset" responses, AP rates remained significantly elevated (n = 43; 5.6 ± 0.8 Hz; two-side t-test, paired: P < 0.03) for the entire duration of the air puff whisker stimulus, before returning back to baseline approximately 100 ms after the stimulus had

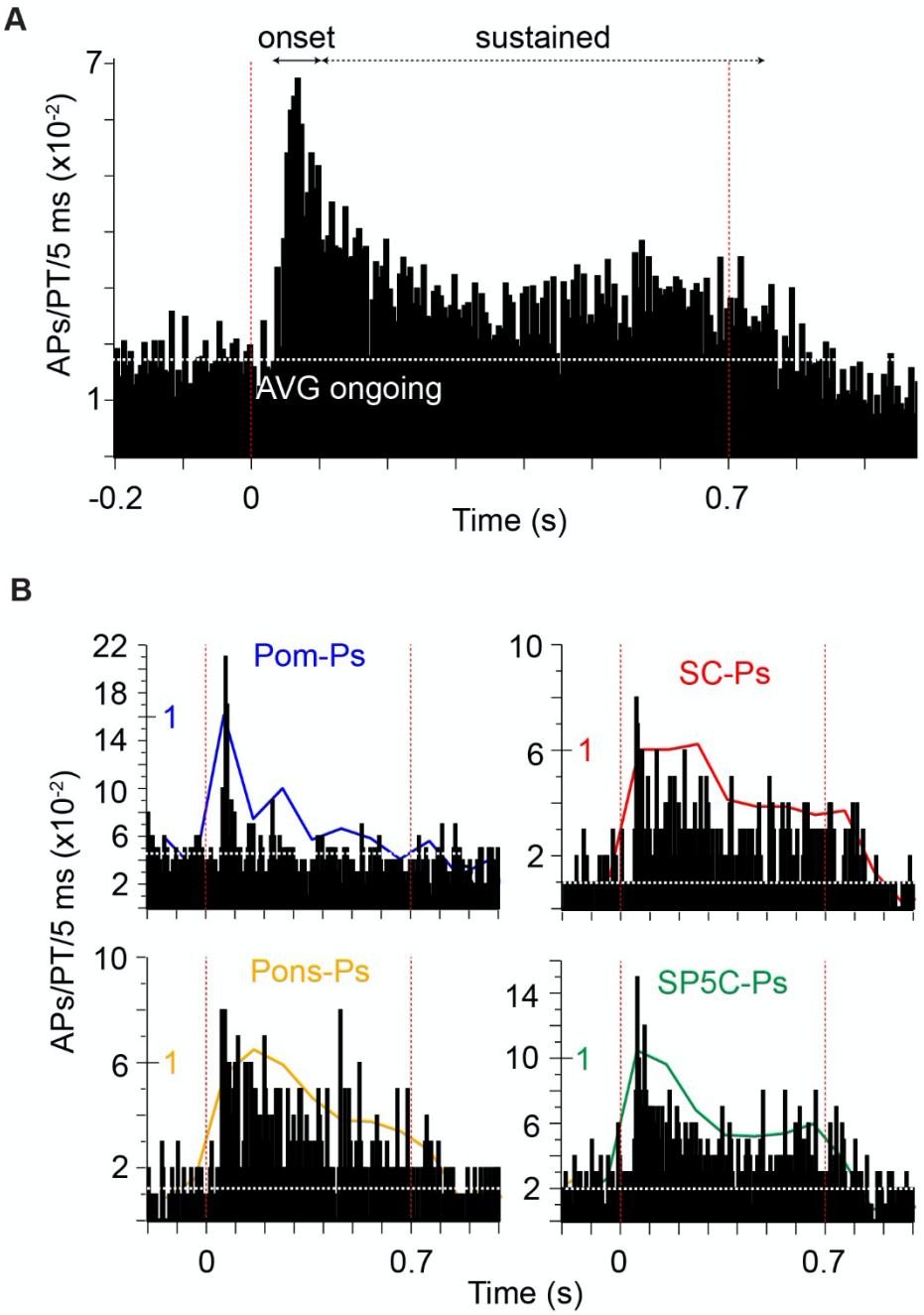

Figure 4.18: Sensory-evoked spiking reflects the subcortical targets of L5PTs: (A) PSTH averaged across 43 L5PTs for passive multi-whisker deflections. (B) PSTHs averaged across L5PTs with the same target. Colored lines: PSTHs with 100 ms resolution and normalized to peak response. Figure is adopted from [22].

ended. These “sustained” responses were related to the respective subcortical target. To quantify these differences two indices (SI) were calculated that allow quantifying the similarity between the PSTH of each individual L5PT and the four PSTHs averaged across L5PTs with the same target (Figure 4.18B). The similarity analysis revealed that sustained AP responses were more similar (n = 5 for each L5PT group; one-way ANOVA of SI1/2: $P < 0.0001/0.0004$) when L5PTs had the same subcortical target Figure 4.19). In Pom projecting L5PTs, AP rates during the sustained responses were comparable to those during ongoing periods, which was significantly different compared to L5PTs that did not project the Pom (n = 28; two-sided t-test of SI1 + 2: $P < 0.002$). In contrast, SP5C projecting, SC projecting, and Pons projecting L5PTs showed increased activity throughout the sustained responses (n = 5 for each L5PT group; Tukey HSD of SI1: $P < 0.01/0.05/0.1$ for Pom projectors vs. SP5C/SC/Pons projectors). Specific for SP5C projecting L5PTs, sustained AP rates increased after about 500 ms, whereas AP rates remained largely constant in SC projecting L5PTs throughout the stimulation and decreased with stimulus duration in Pons projecting L5PTs (Tukey HSD of SI1: $P < 0.01/0.01$ for SP5C projectors (n = 5) vs. SC/Pons projectors (n = 10)). Sustained AP activity patterns of SC and Pons projecting L5PTs were more similar to each other, when compared to Pom and SP5C projecting L5PTs (Figure 4.20), which was also true for their ongoing AP rates. Nonetheless, sustained AP activity patterns of SC and Pons projecting L5PTs differed from each other (n = 10; Tukey HSD of SI2: $P < 0.01$). L5PTs that projected to two targets had evoked spiking patterns that were most similar to those L5PTs, whose cluster they were assigned to (Figure 4.19). Combining the stimulus-

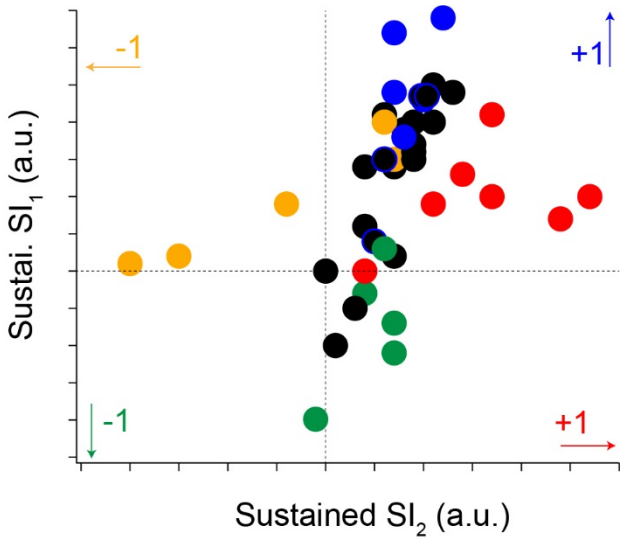

Figure 4.19: Similarities in the sustained responses if L5PTs with the same target. Similarity indices (SIs) between PSTHs of each individual L5PT. Figure is adopted from [22]

independent feature space with responses to the present stimulus increased the confidence level of the clustering to 95%.

4.3 Structural organization of brain-wide whisker muscle related neuronal networks.

Note: This description is adapted from Guest, et al. 2018 [38]. Procedures to label, image, and manually count rabies positive neurons were done by Aman Maharjan, Li Yida, and Fiorella Gomez under my supervision.

I have described in the previous section that L5PTs have structural and functional properties that both reflect and are predictive of their long-range axonal targets. I reported that the soma depth within layer 5, dendrite distribution within the cortical layers, ongoing AP spike rates as well as sensory evoked sustained responses of L5PTs are all predictive of the subcortical target they project to. These findings are indicative that L5PTs when processing information from the same sensory stimulus may be extracting certain features of the stimulus that are most relevant to the downstream target they project to and may be imbedded into target-area related subnetworks. The target related morphological features that L5PTs have, may also indicate that they integrate inputs from different presynaptic populations which could also explain their target related electrophysiological properties.

To test this hypothesis and to better understand how output pathways originating in vS1 are organized, I investigated the structural organization of whisker muscle related brain-wide networks. In the previous chapter I have described in detail of injecting replication competent rabies virus into a single intrinsic whisker muscle which allowed for labeling only sparse population of wMNs, then trans-synaptically labeling presynaptic populations of neurons within brain regions that constitute whisker related neuronal

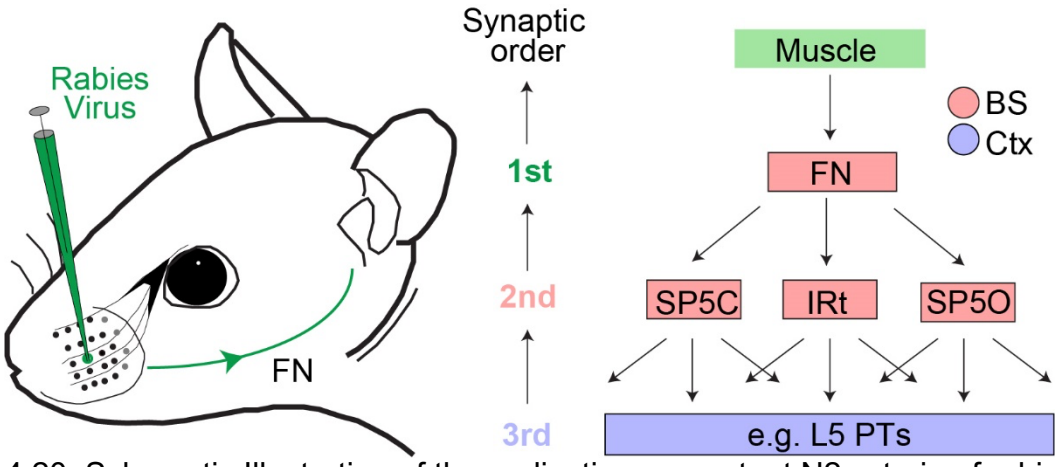

Figure 4.20: Schematic Illustration of the replication competent N2c strain of rabies virus injection experiment. Left: The N2c strain of rabies virus is injected into the C3 intrinsic whisker muscle. Right: Illustration to define the trans-synaptic spread of rabies virus. Figure is adopted from [38]

networks. Quantifying the trans-synaptic spread of the rabies virus across multiple whisker muscle injection experiments revealed certain organizational principles of whisker related brain-wide pathways. In this final result section I will describe anatomical results from injecting replication competent rabies virus targeting a single intrinsic whisker muscle.

Trans-synaptic tracing of whisker muscle-related neuronal networks: Defining orders of rabies infection.

I described in the previous chapter the advantages of using replication competent rabies virus to study the anatomical organization of brain-wide neuronal pathways across multiple synapses. Given the properties of fixed strains of rabies virus, the order of trans-synaptic spread by the time period between virus injection and perfusion was determined. However, because the initial uptake of the rabies virus is not efficient and thereby the onset of rabies infection varies across experiments, the order of trans-synaptic spread was additionally determined by quantifying the brain-wide distributions of rabies-positive neurons in each experiment (Figure 4.20). Following injection of rabies virus into a single whisker muscle, the virus crosses the neuromuscular junction in the retrograde direction, labeling first order motor neurons that innervate the injected muscle (similarly to retrogradely labeled wMNs shown in Figure 3.16). The rabies virus then goes through a round of replication and crosses synapses continuing exclusively in the retrograde direction labeling all 2nd order pre-motor neuronal populations that are presynaptic to (i.e. provide input to) the 1st order motor neurons labeled in the previous step. In the case presented here for the whisker-related musculature, such second order neurons should be restricted to the level of the brain stem [76, 77]. Next, the rabies virus replicates again, crossing synapses in the retrograde direction labeling 3rd order neuronal populations presynaptic to those pre-motor neurons representing 2nd order viral spread. Neurons located in the brainstem are typically post-synaptic (i.e. receive direct input) from PTs located in layer 5 (i.e. L5PTs) of the neocortex [78]. Therefore, experiments where the rabies virus has spread to the level of the neocortex but is restricted to layer 5 are most

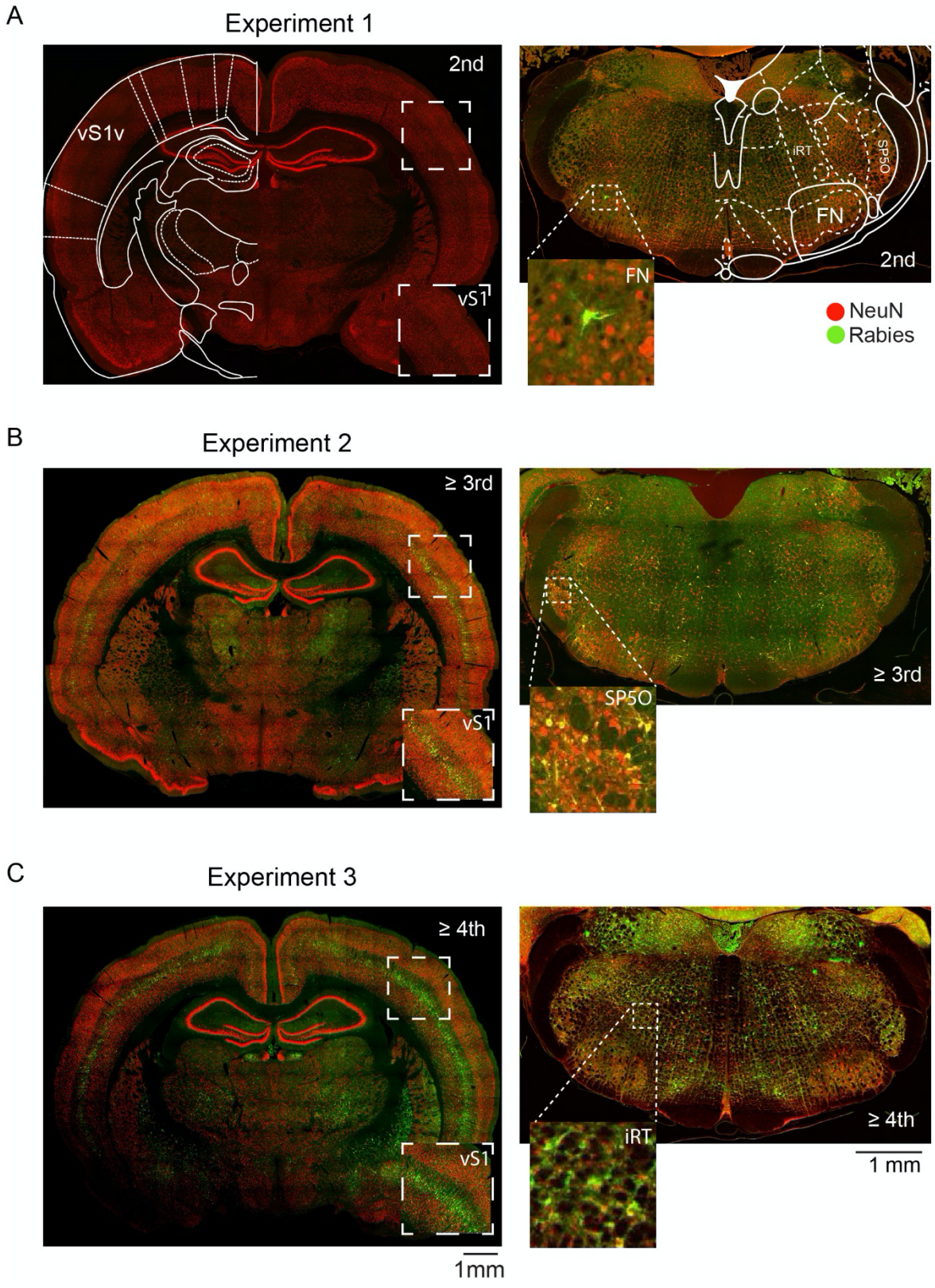
A
Experiment 1
2nd
vS1v
vS1
iRT
SP5O
FN
2nd
FN
NeuN
Rabies
B
Experiment 2
≥ 3rd
vS1
≥ 3rd
SP5O
C
Experiment 3
≥ 4th
vS1
1mm
≥ 4th
iRT
1 mm

Figure 4.21 (*previous page*): Trans-synaptic spread of rabies virus through the brain stem and neocortex. Exemplary images of three experiments illustrating 2nd, 3rd, and ≥ 4th order synaptic spread of N2c strain of rabies virus after injection into the C3 intrinsic whisker muscle. (A) Represents 2nd order rabies spread. Left: Coronal confocal image of a tissue section in the cortex within vS1, illustrating rabies virus labeled neurons were not observed at the level of neocortex. Right: Coronal confocal image of a tissue section in the brain stem within the FN. Rabies labeling was sparse and restricted the brainstem. Zoom-in shows a rabies positive wMN located in the ventro-lateral part of the FN. (B,C) Same as A but illustrates a 3rd order spread (Middle) and ≥4th order spread (bottom). Experiment 2, rabies labeling had spread to the neocortex but was restricted to L5 in vs1 and vM1. Experiment 3, rabies labeling had spread to upper and lower layers and to other sensory cortical areas. B left: Zoom-in is rabies labeled neurons in the trigeminal nucleus oralis (SP5O) (B left) and intermediate reticular nucleus (IRT) (C left). Red neurons are from NeuN labeling and green neurons are rabies labeled.

likely to reflect third order trans-synaptic spread. Experiments where the rabies labeling has spread to layers above and below L5 represent fourth order or higher trans-synaptic spread.

4.3.1 wMNs located in the ventral-lateral facial nucleus are the terminal points of whisker related neuronal networks

In total I injected the C3 whisker with the replication competent N2c strain of rabies virus in 41 rats. For the purpose of this thesis I will report the results of 3 of these injection experiments. I have included a fourth experiment (see figure 4.24) however this experiment is still being analyzed, is speculated to be at least 5th order or higher and is for illustration purposes only. The rest of the injection experiments are currently being analyzed to answer several anatomical questions by other Master and PhD students in the lab.

By quantifying the number and distribution of the rabies labeled neurons and using the criterion for determining the order of synaptic spread I determined that three of the example experiments shown here represent a second order, a 3rd order and a 4th order or higher trans-synaptic spread (Figure 4.21). The first observation from these three experiments and from the registration of the rabies labeled wMNs in the facial nucleus (see Figure 3.23 in the previous chapter) was that was rabies labeled neurons throughout the brainstem increased significantly from lower to higher orders of virus spread except for the first order wMNs in the facial nucleus (Figure 4.21). This indicates that premotor neurons that innervate wMNs in the facial nucleus seem to be interconnected with each other however the first order wMNs are not. To quantify this observation I counted all rabies labeled neurons in whisker related brainstem nuclei including the wMNs in the facial

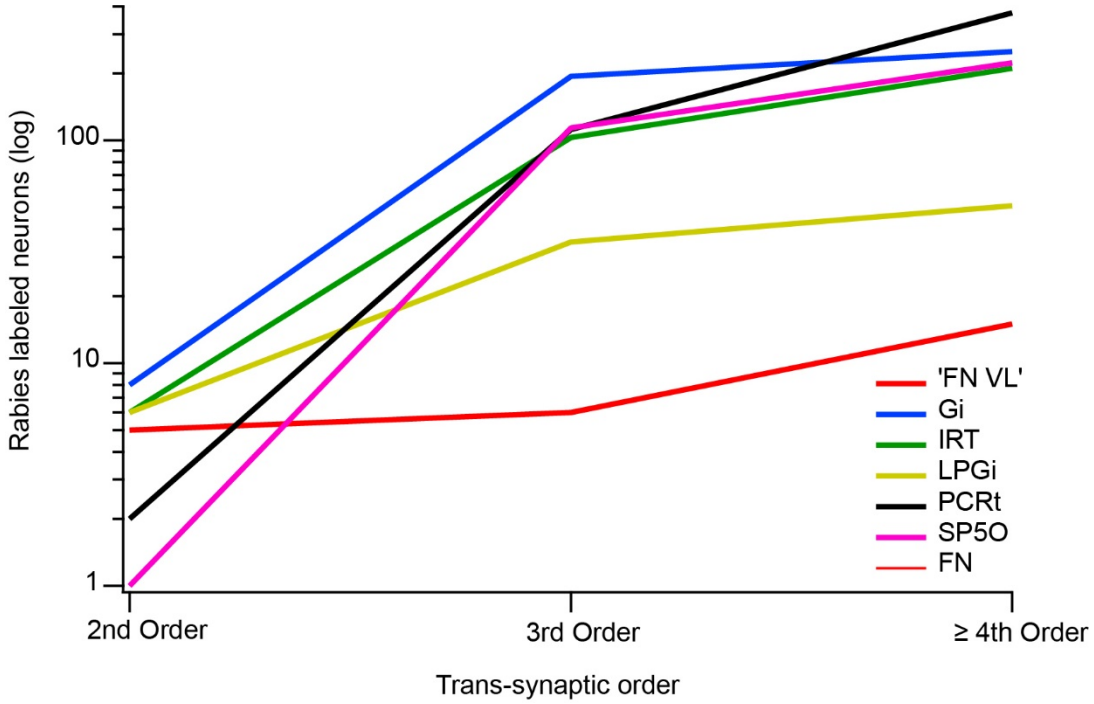

Figure 4.22: Quantification of trans-synaptic rabies spread within the brainstem. From 2nd to 3rd order the increase of rabies labeled neurons was one order of magnitude. The increase from 3rd to ≥4th was 2-4 fold depending on the brainstem nuclei. The lateral part of the facial nucleus was independent of the order of spread, however outside of the lateral (whisker part) of the FN there was an increase in rabies labeling. Figure is adapted from [22].

nucleus across the three experiments representing increasing orders of synaptic spread. It was found that as the rabies spreads from 2nd order to 4th order or higher the number of rabies positive neurons outside of the facial nucleus increased by at least one order of magnitude but remarkably the number of vMNs labeled in the lateral part of the facial nucleus did not significantly increase (Figure 4.22). The lack of recurrent connections observed in wMNs of the lateral FN indicates that they are the terminal points of whisker-related neuronal networks.

4.3.2 Trans-synaptic spread of rabies virus reveals L5PTs in vS1 vary in synaptic distance to the whisker muscles and may receive target related presynaptic input.

In one experiment it was observed that rabies virus had spread beyond the level of the brain stem to the neocortex. Remarkably the spread of rabies labeling in the neocortex was only found in layer 5 of the vibrissal-related somatosensory (i.e. vS1 and S2) and motor areas in both the ipsilateral and contralateral hemispheres (Figure 4.21B and Figure 4.24A). This experiment therefore was determined to be an example of third order synaptic spread. Since neurons labeled by the rabies virus at 2nd order synaptic spread are restricted to the brainstem it could be assumed that the layer 5 neurons labeled at 3rd order represent those L5PTs that only project to the brainstem (for example L5PTs that project to the SP5C). To further investigate this observation I looked at the three experiments representing 2nd order, 3rd order and 4th order or higher synaptic spread to see at which synaptic spreads do the four long-range axonal targets of L5PTs (Pom, Pons, SC, SP5C) investigated in the previous section become labeled with rabies virus (Figure 4.23). I found that at 2nd order synaptic spread that of the four targets only the SP5C in the brainstem was labeled (Figure 4.23A). At 3rd order, I then observed that rabies labeling had spread to the Pons and SC (Figure 4.23B). Finally, rabies labeling in the Pom was not observed until the virus had spread to at least 4 synapses from the whisker muscle. These observations indicates that neurons in layer 5 of vS1 that project to the brainstem (i.e. SP5C) have the shortest synaptic distance to the intrinsic whisker muscles than compared to neurons that project to other long-range subcortical targets (i.e. Pons or SC).

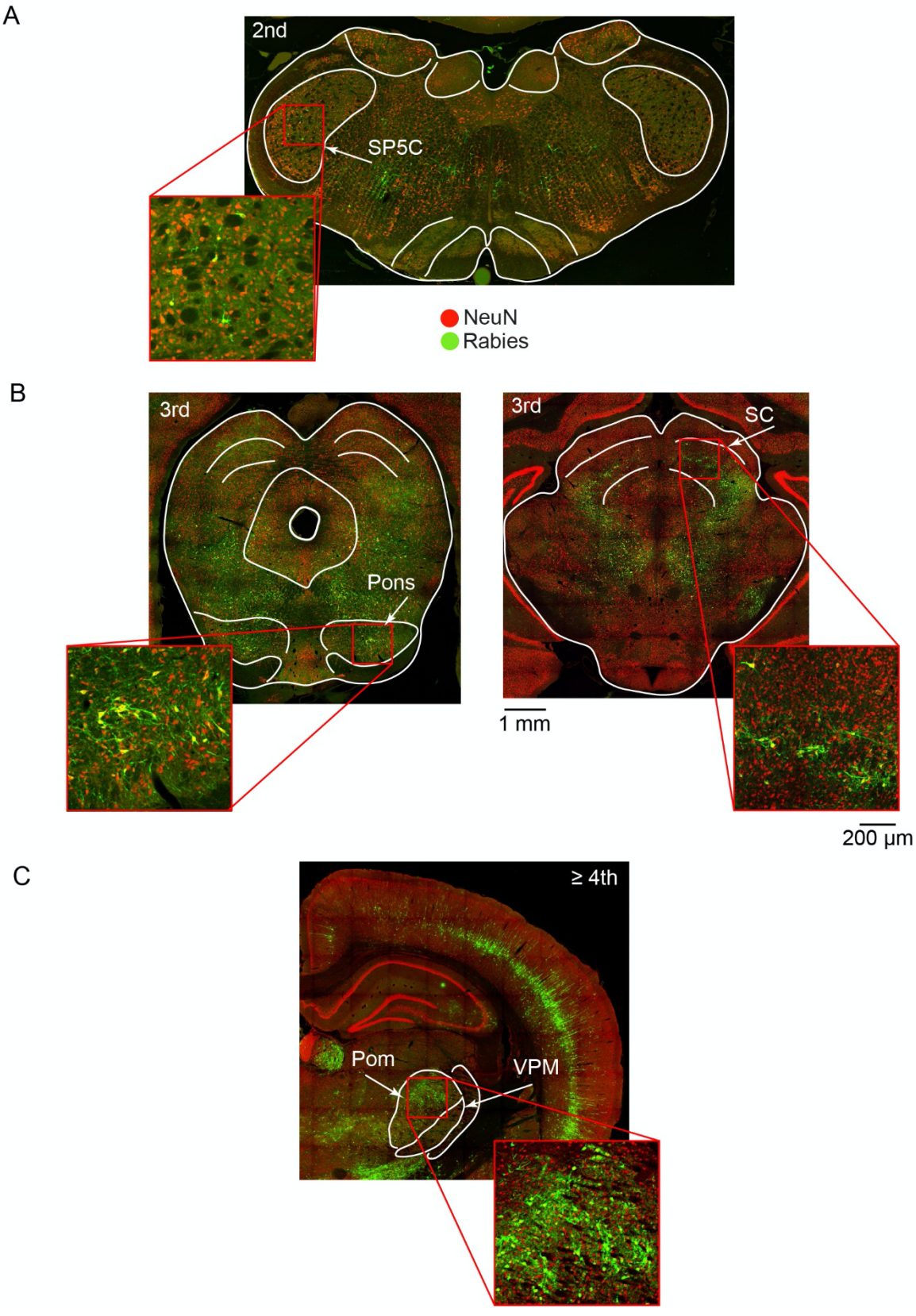
A
2nd
SP5C
NeuN
Rabies
B
3rd
Pons
3rd
SC
1 mm
200 µm
C
≥ 4th
Pom
VPM

Figure 4.23 (*previous page*): Subcortical targets of L5PTs become labeled by rabies virus at different trans-synaptic orders. (A) Example of 2nd order rabies spread and SP5C is the only presently investigated L5PT target area with rabies labeled neurons. Zoom-in shows rabies positive neurons in the SP5C. (B) Example of 3rd order rabies spread and rabies positive neurons are observed in the Pons and SC but not in the Pom (not pictured). Left: zoom-in shows rabies positive neurons in the Pons. Right: zoom-in shows rabies positive neurons in the SC. (C) Example ≥4th order rabies spread and rabies positive neurons are observed in the Pom. Zoom-in shows rabies labeled neurons in the Pom.

To further investigate this observation I quantified the increase of rabies labeling in vS1 and whisker related motor cortex across three different examples of synaptic spread from 3rd order to 5th order or higher (Figure 4.24). For the 3rd order experiment where in the neocortex rabies labeling was confined to layer 5, approximately 6% of neurons in vS1 and 2% of neurons in vM1 were labeled (with respect to NeuN Figure4.24A,D). In the next experiment that showed an increase of at least one additional synaptic order (i.e. ≥ 4th Order) the rabies labeling in L5 for both vS1 and vM1 increased to 12%. It was also observed in this experiment that for both vS1 and vM1 rabies had spread to other layers. In vS1 rabies labeled neurons were observed in L2/3, L4, and L6. In vM1 rabies labeled neurons were also observed in L3, and L6 in addition to the increase in L5 (Figure 4.24B,D). In the last experiment where rabies labeling had been estimated to cross at least one more additional synapse (i.e. ≥ 5th Order) rabies labeling had spread to all cortical layers with the most significant increase in L6 in both vS1 and vM1 (Figure 4.24C,D). Since at 3rd order the rabies labeled neurons in L5 of the neocortex represent only those L5PTs that project to brainstem areas (i.e. SP5C) is assumed that neurons that are presynaptic to these brainstem projecting neurons, contribute to the increase in

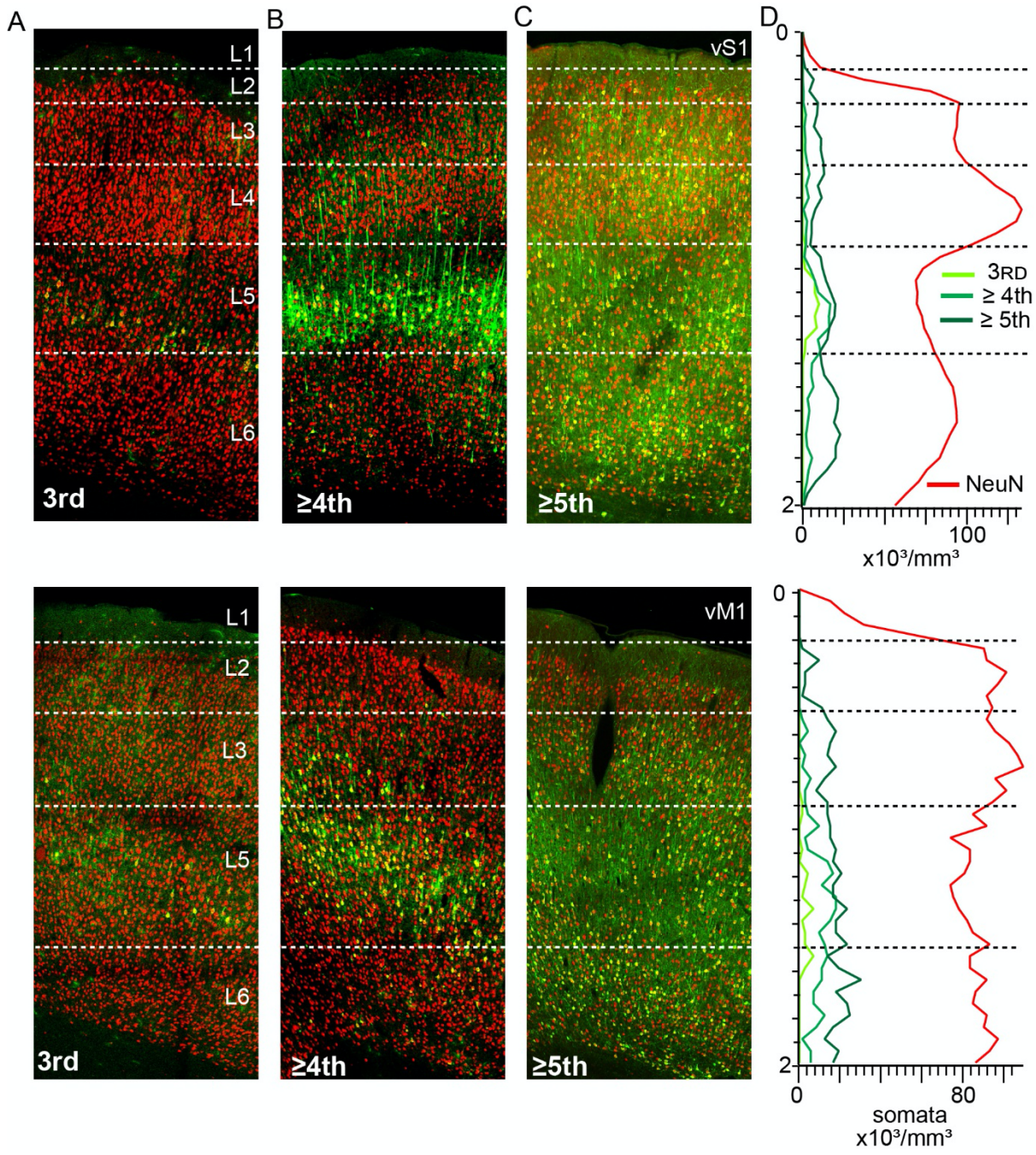
A
B
C
D
L1
L2
L3
L4
L5
L6
3rd
≥4th
≥5th
vS1
vM1
3RD
≥ 4th
≥ 5th
NeuN
0
2
0
100
x10³/mm³
80
somata
x10³/mm³

Figure 4.24 (*previous page*): Quantification of trans-synaptic spread in the neocortex. (A) Example images in vS1 and vM1 of the neocortex of a 3rd order spread experiment. Rabies labeling was restricted to L5 and to both cortical areas. (B) Example images in vs1 and vM1 where rabies labeling had spread to layer 2/3, L4, L6 and increased in L5. (C) Example images where rabies labeling had additionally increased in all layers. (D) 1D profiles showing the step wise increase in rabies labeling in three experiments (shown in A-C) to quantify the increase of rabies labeling in vS1 and vM1 across at least three synaptic crosses of the rabies virus. For all three experiments the number of rabies labeled neurons were aligned and scaled to match the peak density of the NeuN profile in L4.

cortical labeling in the next higher synaptic order and are not presynaptic to L5PTs that project to other long-range subcortical targets. Thus suggesting that L5PTs that project to the brainstem may receive synaptic inputs from different neuronal populations compared to L5PTs that project to either the Pons/SC or Pom.

Chapter 5

Discussion

5.1 Long-range target area related structure-function of cortical output.

The following description is adapted in part from Rojas-Piloni, Guest et al. 2017 [22].

In this thesis I presented an experimental approach to assess the structural properties and in vivo physiology of L5PTs with respect to their long-range axonal targets. The results from combining retrograde tracer injections with in vivo recordings and morphological reconstructions revealed relationships between structure, in vivo function and the respective target area of L5PTs. My colleagues and I investigated four previously identified targets of L5PTs within vS1: Pom, Pons, SC, and SP5C. Surprisingly we found that within these four target areas investigated, L5PTs in vS1 only project to one of these targets. For example L5PTs that project to the Pom do not typically additionally project to the SC, SP5C, or Pons. This does not however infer that L5PTs in vS1 have only a single target in general. It has been shown in the mouse that approximately 40% of PTs project

to two targets and approximately 20% can project to three targets [79]. The target areas investigated in this study also comprise of several sub-nuclei which can contribute to the L5PTs other targets. It has been shown that axon terminals of L5PTs in vS1 cluster within the principle and caudal interpolaris nuclei of the spinal trigeminal tract, in addition to those innervating the SP5C located in the brainstem [80]. Most recently it has also been reported that L5PTs in the mice that project to the Pom also project to the parafasicular and mediodorsal nucleus of the thalamus [81].

The results of these experiments revealed that L5PTs in vS1 have long-range target related AP activity patterns. An explanation for this could be that L5PTs depending on their targets may have different genetic/molecular identity, morphology, and or intrinsic physiological properties. In mouse somatosensory cortex genetic approaches have failed to reveal long-range projections to specific subcortical targets within the group of PTs [55]. However a recently published study revealed in the mouse motor cortex, genetic markers did successfully discriminate between L5PTs that project to either the thalamus or medulla and in agreement with our study that these two neuronal populations displayed long-range target related functional properties [82].

5.2 Cortical output is organized in long-range target related pathways

The results of the replication competent rabies virus injection into a single whisker revealed the multi-synaptic organization of brain structures associated with whisker motor control. In order to assess the accuracy of the rabies injection I compared the rabies labeled neurons that were located in the facial nucleus with those neurons labeled by cholera toxin injection into the same whisker from separate experiments. By incorporating data from rabies and cholera toxin injection experiments into a standardized FN reference frame [38] the majority of rabies labeled wMNs were located in the targeted whisker's representative "slab". There were a few rabies labeled neurons in all experiments that were found just outside of target whisker slab suggesting that the rabies virus could have spread to adjacent rows as observed in the cholera toxin injection experiments. Also for experiments where the rabies virus crossed more than 3 synapses rabies labeling was observed in the more medial part of the facial nucleus in addition to the expected ventral lateral labeling of wMNs. Recent studies using the same N2c strain of rabies virus injected into the deflector nasi muscle in rats resulted in labeling first order neurons in the far medial part of the facial nucleus [83]. This suggests that motor neurons involved in nose movement may be presynaptic to brain regions that are also involved in whisker networks. Given the large distance from the whisker muscle to the delfector nasi muscle, makes it unlikely the labeling observed in the medial part of the FN was due to tracer spread or an errant injection.

The major result from the rabies injection experiments is that not all of the subcortical targets of L5PTs in vS1 investigated in this thesis showed rabies infection in the same synaptic order, indicating that L5PTs depending on their long-range target, have different synaptic differences to the whisker muscles. For example at 2nd order (i.e. two synapse from the whisker muscle) rabies labeling was restricted to the brainstem including the SP5C trigeminal nuclei ipsilateral to the injected whisker. In the next synaptic order rabies labeling had spread to the Pons, SC and observed in the neocortex in L5. Therefore those rabies labeled neurons observed in L5 at 3rd order must be presynaptic to the premotor brainstem neurons that were labeled in the previous synaptic order (i.e. 2nd order). This long-range target related organization of L5PTs may not be restricted to the whisker system as similar organizational principles were observed for the neuronal pathways involved in nose movements [83].

5.3 Top-down modulation of cortical output is gated by the thalamus.

The results of quantifying the structural organization of primary TC inputs onto the complete dendritic arbors of L5PTs in vS1 revealed that neurons located in the VPM specifically form a dense area of synaptic connections near to the main apical dendrite bifurcation. I referred to this dense area of TC synapses as a TC “hot zone” and is defined as an area along the dendritic arbor with the highest observed TC putative synaptic density. For the ten L5PTs where I quantified the distribution of primary TC putative synapses, the highest synaptic density was always found on the apical trunk and significantly correlated with the location of the apical dendrite main bifurcation (see figures 4.7 - 4.10). The measured distance from the soma to the TC hot zone ranged from 425 – 900 μm. In most cases the TC hot zone was found to be an obvious single peak in proximity to where the apical dendrite first bifurcates to form the apical tuft. For some L5PTs two even three TC synaptic density peaks were observed along the apical trunk and for 3 cells it appeared there was a preference of TC input for most of the apical trunk in L4 and L2/3. The most interesting observation was that most of the TC hot zones were found on segments of the apical trunk in L2/3 and the oblique dendrites located in L4 were mostly spared of TC synapses even though L4 has been reported to have the highest density of primary TC synapses [16].

Even though the virus mediated method for mapping synaptic inputs presented in this thesis has been successfully used in a prior study for L4 excitatory neurons [47], to date this is the first time this method has been applied to the complete dendritic arbors of

L5PTs. Since the dendrites of L5PTs can reach all six layers it was not only necessary to validate the labeling efficiency of the virus but also confirm that the synapses labeled were from primary and not higher order thalamus, since it is known that L5PTs in vS1 additionally receive input also from Pom [84]. Therefore I estimated the virus efficiency and percentage of falsely identified primary TC synapses not only for L4 but also for L2/3 and L5 by combining the injection experiments with VGlut2 staining (see Figure 3.3). I found no significant difference in virus efficacy nor significant change in percentage of false positives across the different cortical layers indicting that majority if not all of the identified putative primary TC synapses should be primary TC synapses and not higher order TC synapses. Another limitation to this method is that electron microscopy is required to determine whether a putative synapse identified using light microscopy contains the necessary ultrastructural features to be confirmed a true synapse. In order to overcome this limitation I repeated the exact light microscopy method and achieved similar results for estimating the primary TC synaptic distribution for one L4 spiny stellate (see Figure 3.4) as done in [47] in which the authors did confirm a subset of their putative synapses using electron microscopy. So now what could be the functional implications for the TC “hot zone”?

L5PTs are large pyramidal neurons whose dendrites integrate proximal and far distal synaptic inputs across all six layers of neocortex (reviewed in [25]). Another property of L5PTs is the presence of several calcium mediated dendritic activation zones that are thought to be required for the coupling of far distal inputs arriving in the tuft dendrites with those inputs arriving more proximal to the soma [85-87]. In a study by Yuste et al [87], the authors revealed that localized accumulation of calcium forms a “band” on

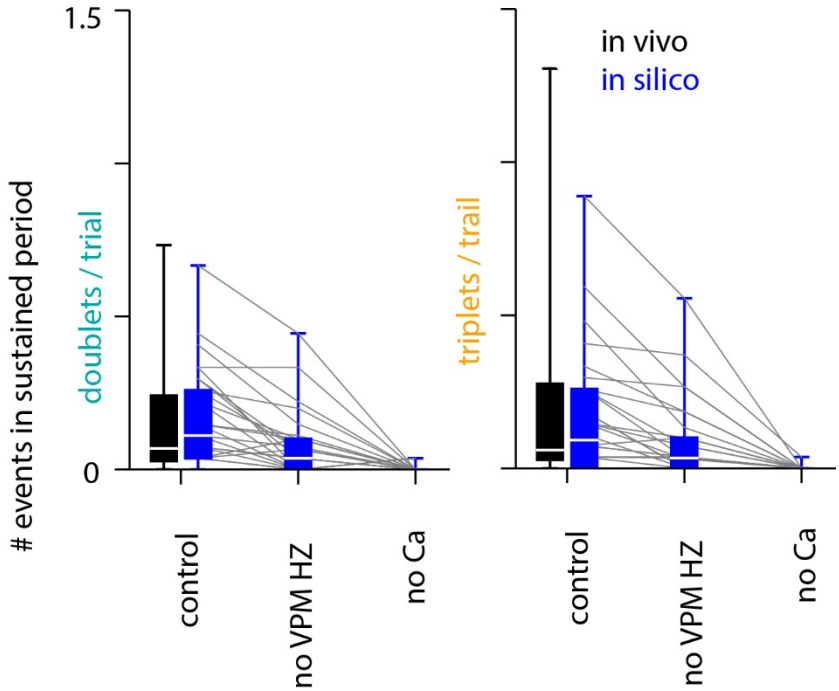

Figure 5.1: In silico model predicts TC hot zone facilitates calcium mediated burst responses in L5PTs. First, VPM synapses at a distance > 500 microns were removed. Second, the synapses remained unchanged, however Ca conductances were removed from the dendrite. For each model and each manipulation, the amount of high frequency events (burst: 3 spikes in 30ms, doublet: 2 spikes in 10ms; if an event full fills both definitions, it is assigned as burst) was calculated. The burst and doublet rate for each individual model is visualized as thin grey lines. Barplots represent mean and standard deviation. These manipulations show a moderate reduction in the rate of high frequency events if distal VPM synapses are removed and an almost complete reduction if the Ca-conductances are removed from the dendritic tree. Figure provided by Arco Bast (Max Planck Group In Silico Brain Sciences, Center of Advanced European Research and Studies).

the apical dendrite near to the apical dendrite primary bifurcation that can be activated synaptically. The authors also showed that the apical band can generate calcium spikes when activated and may functionally serve to amplify distal synaptic events. In another study by Larkum et al. published in 1999 [88], revealed an in vitro mechanism, albeit that is dependent on a back propagating AP, by where L5PTs can associate inputs arriving at different distal dendritic locations which results in a burst of APs at the soma, evidence of a dendritic non-linearity event. More recent in vivo studies have shown that calcium mediated coupling of long-range distal inputs arriving in the apical tuft dendrites of L5PTs plays an important role for higher order brain functions such as sensory perception and perceptual learning [89-91].

What all these studies have in common is they show that calcium channels expressed in specific compartments of the apical dendrite mediate non-linear dendritic events is required for dendritic coupling. To test whether primary TC input to the “hot zone” can facilitate calcium activity in the apical dendrite and thereby serve a functional role in dendritic coupling, my colleague Arco Bast (Max Planck Group In Silico Brain Sciences, Center of Advanced European Studies and Research) performed in silico simulations using one of my reconstructed L5PTs (example 2 shown in Figure 4.7) as a full compartmental neuron model. This is currently on going work, however preliminary results do provide evidence for a functional role of the TC hot zone. The multiscale L5PT model showed that during sensory stimulation, primary TC input to the “hot zone” can contribute to calcium mediated burst responses at the soma. During simulation trials where the TC synapses were removed from the hot zone the result was a significant decrease in the bursting activity of the neuron. In simulation trials where calcium channels

were removed from the hot zone bursting activity was nearly abolished (Figure 5.1). These in silico predictions suggest that dense primary TC synaptic input to the hot zone of the L5PTs can facilitate dendritic non-linear events (i.e. burst firing of APs) and thus allow otherwise fast attenuating distal inputs to modulate AP spiking output activity of the neuron.

5.4 Outlook

The results that I have presented in this thesis provide an understanding to basic principles underlying the structural organization and function of primary thalamic input pathways and cortical output pathways originating from L5PTs. Although the findings presented in this thesis do provide new insight into how long-range pathways contribute to sensory information processing, further investigations are needed to understand how these newly discovered principles are actually used by the animal, for example decision making during tactile based behaviors. It has been reported that rats can detect small changes in surface textures to a level of efficiency and accuracy that compares to how humans and non-human primates use their fingertips [92]. Since the target-related sensory evoked responses reported in this thesis were measured for a passive whisker stimulus and under anesthetized conditions, it would be extremely interesting to see how L5PTs that have different long-range targets extract information for an active whisker stimulus (such as texture discrimination) in an awake brain state. This would be feasible since the structural and functional properties of L5PTs allow for the prediction

of their targets and therefore it would not be necessary to rely on combining the use of retrograde injections to correlate the behavioral neuronal responses to the long-range target.

The discovery of the primary TC “hotzone” on the dendrites was based on bulk labeling of TC synaptic boutons by virus injections into the VPM thalamus. This provides anatomical insight to how in general neurons in the primary thalamus can target L5PTs within a cortical area. Further studies are required to understand how this newly discovered wring principle is applied at the single cell level. For example one could ask do all thalamic neurons innervate the basal dendrites and apical dendrite trunk equally or are some neurons specific for each dendritic compartment? Therefore a challenging but necessary in vivo experiment would be to record/biocyin fill neurons in the VPM and L5PTs in vS1, in order to measure where the synaptic connections occur between a single thalamic neuron and its paired L5PT.

Chapter 6

Summary

In this thesis I have presented the results from several in vivo experimental approaches for the purpose of understanding basic structure-function properties of long-range primary thalamo-cortical input pathways and primary output neurons in vS1 of rats. In a collaborative effort, my colleagues and I discovered that L5PTs in rat vS1 display certain structural and functional properties that reflect their long-range axonal target area. By combining monosynaptic injections of retrograde tracers with cell-attached recordings and morphological reconstructions we showed that soma depth, layer-specific dendrite distributions, ongoing and sensory evoked responses of L5PTs are predictive of the subcortical brain area they target. We concluded from this finding that L5PTs may be imbedded in the local circuitry in a long-range axonal target related manner. Specifically, that due to target related differences in soma depth and layer-specific dendrite distributions, L5PTs may integrate synaptic inputs from different neuronal populations that allow them to extract certain features of the same sensory stimulus that are most relevant to their targets.

In order to test this hypothesis and to better understand how output pathways in vS1 are organized in general, using an entirely anatomical approach, I investigated the structural organization of whisker muscle related brain-wide neuronal networks. Injecting

the replication competent N2c strain of rabies virus into a single intrinsic whisker muscle revealed the trans-synaptic organization of brainstem and cortical brain areas that are involved in whisker sensory-motor control. These experiments revealed that wMNs located in the lateral facial nucleus that control the movements of single whiskers are the terminal points of whisker related neuronal pathways. More importantly these experiments also yielded anatomical evidence that L5PTs that project to the trigeminal nuclei in the brainstem have the shortest synaptic distance to the whisker muscles compared to L5PTs that project to either the Pons, SC or Pom. Thus indicating that L5PTs may be imbedded into brain-wide subnetworks that are specific to their long-range targets.

Finally in an effort to better understand the basic principles of how L5PTs integrate long-range inputs and how these inputs may contribute to their sensory evoked activity patterns, I investigated the structural organization of primary TC inputs in vS1 of rats. By selectively labeling primary TC synaptic terminals in vS1 by virus injections combined with cell attached recordings and morphological reconstructions, I measured the neuronal response properties to photo stimulated TC synapses and quantified the distribution of these inputs onto the dendrites of L5PTs. These results revealed that the same neurons in the primary thalamus that provide feed-forward excitation to the basal dendrites of L5PTs in vS1 additionally form a dense hot zone of synaptic connections that coincide with the location of the apical dendrite primary bifurcation. Preliminary results of multiscale simulations showed that during sensory stimulation, TC input into the hot zone coinciding with top-down inputs into the apical dendrites can facilitate calcium mediated non-linear dendritic events which results in action potential bursts at the soma. In addition

optogenetic activation of these primary TC synapses resulted in burst responses by L5PTs, experimental evidence that TC synapses can directly contribute to non-linear dendritic events. The data presented in this thesis suggests the TC hot zone could function to effectively depolarize the apical dendrite past the threshold for calcium activity, providing a gating mechanism by which the thalamus can regulate how inputs to the apical dendrites modulate sensory evoked cortical output patterns.

In conclusion the results I show in this thesis provides empirical evidence that L5PTs extract certain features from the same sensory stimulus that are most relevant for their long-range targets by in part integrating target specific presynaptic inputs. Because the TC hot zone seems to be a common wiring principle for L5PTs throughout vS1, this may be a mechanistic origin for the target related function of L5PTs. By providing synchronous feed-forward excitation from the thalamus to the hot zone upon sensory stimulation would provide the necessary integration window by which any distal inputs arriving in the apical dendrites at the time of the stimulus, to modulate the output response at the soma and thereby contribute to the L5PTs target related sensory evoked AP activity patterns.

List of Figures

Bibliography

1. Oh, S.W., et al., *A mesoscale connectome of the mouse brain.* Nature, 2014. **508**(7495): p. 207-214.

2. Park, H.J. and K. Friston, *Structural and functional brain networks: from connections to cognition.* Science, 2013. **342**(6158): p. 1238411.

3. Zavitz, E. and N.S.C. Price, *Understanding Sensory Information Processing Through Simultaneous Multi-area Population Recordings.* Frontiers in neural circuits, 2019. **12**: p. 115-115.

4. Larkum, M., *A cellular mechanism for cortical associations: an organizing principle for the cerebral cortex.* Trends in Neurosciences, 2013. **36**(3): p. 141-151.

5. Nelson, A., et al., *A Circuit for Motor Cortical Modulation of Auditory Cortical Activity.* The Journal of Neuroscience, 2013. **33**(36): p. 14342.

6. Akintunde, A. and D.F. Buxton, *Differential sites of origin and collateralization of corticospinal neurons in the rat: a multiple fluorescent retrograde tracer study.* Brain Res., 1992. **575**.

7. Aronoff, R., et al., *Long-range connectivity of mouse primary somatosensory barrel cortex.* Eur J Neurosci, 2010. **31**(12): p. 2221-33.

8. Welker, E., P.V. Hoogland, and H. Van der Loos, *Organization of feedback and feedforward projections of the barrel cortex: a PHA-L study in the mouse.* Exp Brain Res, 1988. **73**(2): p. 411-35.

9. White, E.L. and R.A. DeAmicis, *Afferent and efferent projections of the region in mouse SmL cortex which contains the posteromedial barrel subfield.* J Comp Neurol, 1977. **175**(4): p. 455-82.

10. Yamashita, T., et al., *Diverse Long-Range Axonal Projections of Excitatory Layer 2/3 Neurons in Mouse Barrel Cortex.* Front Neuroanat, 2018. **12**: p. 33.

11. Petersen, C.C.H., *Sensorimotor processing in the rodent barrel cortex.* Nat Rev Neurosci, 2019. **20**(9): p. 533-546.

12. Leong, A.T., et al., *Long-range projections coordinate distributed brain-wide neural activity with a specific spatiotemporal profile.* Proc Natl Acad Sci U S A, 2016. **113**(51): p. E8306-e8315.

13. MacLean, J.N., et al., *Internal dynamics determine the cortical response to thalamic stimulation.* Neuron, 2005. **48**(5): p. 811-23.

14. Alonso, J.M. and H.A. Swadlow, *Thalamus controls recurrent cortical dynamics.* Nat Neurosci, 2015. **18**(12): p. 1703-4.

15. Feldmeyer, D., et al., *Barrel cortex function.* Prog Neurobiol, 2013. **103**: p. 3-27.

16. Wimmer, V.C., et al., *Dimensions of a projection column and architecture of VPM and POm axons in rat vibrissal cortex.* Cereb Cortex, 2010. **20**(10): p. 2265-76.

17. Oberlaender, M., *Cell type-specific three-dimensional structure of thalamocortical circuits in a column of rat vibrissal cortex.* Cereb. Cortex, 2012. **22**.

18. Bruno, R.M., *Synchrony in sensation.* Curr Opin Neurobiol, 2011. **21**(5): p. 701-8.

19. Harris, K.D. and G.M. Shepherd, *The neocortical circuit: themes and variations.* Nat. Neurosci., 2015. **18**.

20. Wise, S.P. and E.G. Jones, *Somatotopic and columnar organization in the corticotectal projection of the rat somatic sensory cortex.* Brain Res., 1977. **133**.

21. Chen, J.L., et al., *Behaviour-dependent recruitment of long-range projection neurons in somatosensory cortex.* Nature, 2013. **499**.

22. Rojas-Piloni, G., et al., *Relationships between structure, in vivo function and long-range axonal target of cortical pyramidal tract neurons.* Nat Commun, 2017. **8**(1): p. 870.

23. Egger, R., et al., *Cortical Output Is Gated by Horizontally Projecting Neurons in the Deep Layers.* Neuron, 2020. **105**(1): p. 122-137.e8.

24. Wise, S.P. and E.G. Jones, *Cells of origin and terminal distribution of descending projections of the rat somatic sensory cortex.* J. Comp. Neurol., 1977. **175**.

25. Ramaswamy, S. and H. Markram, *Anatomy and physiology of the thick-tufted layer 5 pyramidal neuron.* Front. Cell Neurosci., 2015. **9**.

26. Narayanan, R.T., *Beyond columnar organization: cell type- and target layer-specific principles of horizontal axon projection patterns in rat vibrissal cortex.* Cereb. Cortex, 2015. **25**.

27. Brown, S.P. and S. Hestrin, *Intracortical circuits of pyramidal neurons reflect their long-range axonal targets.* Nature, 2009. **457**(7233): p. 1133-6.

28. Shepherd, G.M., *Corticostriatal connectivity and its role in disease.* Nat. Rev. Neurosci., 2013. **14**.

29. Brecht, M. and B. Sakmann, *Whisker maps of neuronal subclasses of the rat ventral posterior medial thalamus, identified by whole-cell voltage recording and morphological reconstruction.* J Physiol, 2002. **538**(Pt 2): p. 495-515.

30. Manns, I.D., B. Sakmann, and M. Brecht, *Sub- and suprathreshold receptive field properties of pyramidal neurones in layers 5A and 5B of rat somatosensory barrel cortex.* J. Physiol., 2004. **556**.

31. Ito, M., *Simultaneous visualization of cortical barrels and horseradish peroxidase-injected layer 5b vibrissa neurones in the rat.* J Physiol, 1992. **454**: p. 247-65.

32. Constantinople, C.M. and R.M. Bruno, *Deep cortical layers are activated directly by thalamus.* Science, 2013. **340**.

33. Kasper, E.M., et al., *Pyramidal neurons in layer-5 of the rat visual-cortex .1. Correlation among cell morphology, intrinsic electrophysiological properties, and axon targets.* J. Comp. Neurol., 1994. **339**.

34. Kim, E.J., et al., *Three types of cortical layer 5 neurons that differ in brain-wide connectivity and function.* Neuron, 2015. **88**.

35. Kock, C.P. and B. Sakmann, *Spiking in primary somatosensory cortex during natural whisking in awake head-restrained rats is cell-type specific.* Proc. Natl Acad. Sci. USA, 2009. **106**.

36. Oberlaender, M., *Three-dimensional axon morphologies of individual layer 5 neurons indicate cell type-specific intracortical pathways for whisker motion and touch.* Proc. Natl Acad. Sci. USA, 2011. **108**.

37. Lur, G., et al., *Projection-specific visual feature encoding by layer 5 cortical subnetworks.* Cell Rep., 2016. **14**.

38. Guest, J.M., et al., *3D reconstruction and standardization of the rat facial nucleus for precise mapping of vibrissal motor networks.* Neuroscience, 2018. **368**: p. 171-186.

39. Mullen, R.J., C.R. Buck, and A.M. Smith, *NeuN, a neuronal specific nuclear protein in vertebrates.* Development, 1992. **116**.

40. Oberlaender, M., et al., *Transmitted light brightfield mosaic microscopy for three-dimensional tracing of single neuron morphology.* J Biomed Opt, 2007. **12**(6): p. 064029.

41. Oberlaender, M., et al., *Shack-Hartmann wave front measurements in cortical tissue for deconvolution of large three-dimensional mosaic transmitted light brightfield micrographs.* J. Microsc., 2009. **233**.

42. Dercksen, V.J., H.C. Hege, and M. Oberlaender, *The filament editor: an interactive software environment for visualization, proof-editing and analysis of 3D neuron morphology.* Neuroinformatics, 2014. **12**.

43. *Stalling, D., Westerhoff, M. & Hege, H. Visualization Handbook (Academic Press 2005).*

44. Oberlaender, M., *Automated three-dimensional detection and counting of neuron somata.* J. Neurosci. Methods, 2009. **180**.

45. Meyer, H.S., *Cellular organization of cortical barrel columns is whisker-specific.* Proc. Natl Acad. Sci. USA, 2013. **110**.

46. de Kock, C.P. and B. Sakmann, *High frequency action potential bursts (>or= 100 Hz) in L2/3 and L5B thick tufted neurons in anaesthetized and awake rat primary somatosensory cortex.* J Physiol, 2008. **586**(14): p. 3353-64.

47. Schoonover, C.E., et al., *Comparative strength and dendritic organization of thalamocortical and corticocortical synapses onto excitatory layer 4 neurons.* J Neurosci, 2014. **34**(20): p. 6746-58.

48. *Paxinos, G. & Watson, C. The Rat Brain and Stereotaxic Coordinates (Amsterdam Elsevier Academic Press, 2005).*

49. Fujiyama, F., T. Furuta, and T. Kaneko, *Immunocytochemical localization of candidates for vesicular glutamate transporters in the rat cerebral cortex.* J Comp Neurol, 2001. **435**(3): p. 379-87.

50. Graziano, A., et al., *Vesicular glutamate transporters define two sets of glutamatergic afferents to the somatosensory thalamus and two thalamocortical projections in the mouse.* J Comp Neurol, 2008. **507**(2): p. 1258-76.

51. Mease, R.A., et al., *Corticothalamic spike transfer via the L5B-POm pathway in vivo.* Cereb. Cortex, 2016. **26**.

52. Lee, J.H., et al., *LFP-guided targeting of a cortical barrel column for in vivo two-photon calcium imaging.* Sci Rep, 2015. **5**: p. 15905.

53. Mitzdorf, U., *Current source-density method and application in cat cerebral cortex: investigation of evoked potentials and EEG phenomena.* Physiol Rev, 1985. **65**(1): p. 37-100.

54. de Kock, C.P., et al., *Layer- and cell-type-specific suprathreshold stimulus representation in rat primary somatosensory cortex.* J Physiol, 2007. **581**(Pt 1): p. 139-54.

55. Sorensen, S.A., *Correlated gene expression and target specificity demonstrate excitatory projection neuron diversity.* Cereb. Cortex, 2015. **25**.

56. Killackey, H.P. and S.M. Sherman, *Corticothalamic projections from the rat primary somatosensory cortex.* J. Neurosci., 2003. **23**.

57. Wang, Z. and D.A. McCormick, *Control of firing mode of corticotectal and corticopontine layer V burst-generating neurons by norepinephrine, acetylcholine, and 1S,3R-ACPD.* J. Neurosci., 1993. **13**.

58. Ashwell, K.W., *The adult mouse facial nerve nucleus: morphology and musculotopic organization.* Journal of anatomy, 1982. **135**(Pt 3): p. 531-538.

59. Dörfl, J., *The innervation of the mystacial region of the white mouse: A topographical study.* Journal of anatomy, 1985. **142**: p. 173-184.

60. Wineski, L.E., *Facial morphology and vibrissal movement in the golden hamster.* J Morphol, 1985. **183**(2): p. 199-217.

61. Ugolini, G., *Advances in viral transneuronal tracing.* J Neurosci Methods, 2010. **194**(1): p. 2-20.

62. Kelly, R.M. and P.L. Strick, *Rabies as a transneuronal tracer of circuits in the central nervous system.* J Neurosci Methods, 2000. **103**(1): p. 63-71.

63. Tang, Y., et al., *Spinal and brain circuits to motoneurons of the bulbospongiosus muscle: retrograde transneuronal tracing with rabies virus.* J Comp Neurol, 1999. **414**(2): p. 167-92.

64. Ugolini, G., *Use of rabies virus as a transneuronal tracer of neuronal connections: implications for the understanding of rabies pathogenesis.* Dev Biol (Basel), 2008. **131**: p. 493-506.

65. Ugolini, G., *Specificity of rabies virus as a transneuronal tracer of motor networks: transfer from hypoglossal motoneurons to connected second-order and higher order central nervous system cell groups.* J Comp Neurol, 1995. **356**(3): p. 457-80.

66. Klingen, Y., K.K. Conzelmann, and S. Finke, *Double-labeled rabies virus: live tracking of enveloped virus transport.* J Virol, 2008. **82**(1): p. 237-45.

67. Kelly, R.M. and P.L. Strick, *Cerebellar loops with motor cortex and prefrontal cortex of a nonhuman primate.* J Neurosci, 2003. **23**(23): p. 8432-44.

68. Rathelot, J.A. and P.L. Strick, *Subdivisions of primary motor cortex based on cortico-motoneuronal cells.* Proc Natl Acad Sci U S A, 2009. **106**(3): p. 918-23.

69. Rathelot, J.A., R.P. Dum, and P.L. Strick, *Posterior parietal cortex contains a command apparatus for hand movements.* Proc Natl Acad Sci U S A, 2017. **114**(16): p. 4255-4260.

70. Klein, B.G. and R.W. Rhoades, *Representation of whisker follicle intrinsic musculature in the facial motor nucleus of the rat.* J Comp Neurol, 1985. **232**(1): p. 55-69.

71. Egger, R., et al., *3D reconstruction and standardization of the rat vibrissal cortex for precise registration of single neuron morphology.* PLoS Comput. Biol., 2012. **8**.

72. Tordo, N., et al., *Walking along the rabies genome: is the large G-L intergenic region a remnant gene?* Proc Natl Acad Sci U S A, 1986. **83**(11): p. 3914-8.

73. Narayanan, R.T., et al., *Beyond Columnar Organization: Cell Type- and Target Layer-Specific Principles of Horizontal Axon Projection Patterns in Rat Vibrissal Cortex.* Cereb Cortex, 2015. **25**(11): p. 4450-68.

74. Romand, S., et al., *Morphological Development of Thick-Tufted Layer V Pyramidal Cells in the Rat Somatosensory Cortex.* Frontiers in Neuroanatomy, 2011. **5**(5).

75. Ahissar, E., R. Sosnik, and S. Haidarliu, *Transformation from temporal to rate coding in a somatosensory thalamocortical pathway.* Nature, 2000. **406**.

76. Hattox, A.M., C.A. Priest, and A. Keller, *Functional circuitry involved in the regulation of whisker movements.* The Journal of comparative neurology, 2002. **442**(3): p. 266-276.

77. Takatoh, J., et al., *New modules are added to vibrissal premotor circuitry with the emergence of exploratory whisking.* Neuron, 2013. **77**(2): p. 346-60.

78. Sreenivasan, V., et al., *Parallel pathways from motor and somatosensory cortex for controlling whisker movements in mice.* The European journal of neuroscience, 2015. **41**(3): p. 354-367.

79. Guo, C., *Single-axon level morphological analysis of corticofugal projection neurons in mouse barrel field.* Sci. Rep., 2017. **7**.

80. Hattox, A.M. and S.B. Nelson, *Layer V neurons in mouse cortex projecting to different targets have distinct physiological properties.* J. Neurophysiol., 2007. **98**.

81. Winnubst, J., et al., *Reconstruction of 1,000 Projection Neurons Reveals New Cell Types and Organization of Long-Range Connectivity in the Mouse Brain.* Cell, 2019. **179**(1): p. 268-281.e13.

82. Economo, M.N., et al., *Distinct descending motor cortex pathways and their roles in movement.* Nature, 2018. **563**(7729): p. 79-84.

83. Kurnikova, A., M. Deschênes, and D. Kleinfeld, *Functional brain stem circuits for control of nose motion.* Journal of neurophysiology, 2019. **121**(1): p. 205-217.

84. Wimmer, V.C., et al., *Dimensions of a projection column and architecture of VPM and POm axons in rat vibrissal cortex.* Cereb. Cortex, 2010. **20**.

85. Schiller, J., et al., *Calcium action potentials restricted to distal apical dendrites of rat neocortical pyramidal neurons.* The Journal of physiology, 1997. **505 (Pt 3)**(Pt 3): p. 605-616.

86. Larkum, M.E., J.J. Zhu, and B. Sakmann, *Dendritic mechanisms underlying the coupling of the dendritic with the axonal action potential initiation zone of adult rat layer 5 pyramidal neurons.* J Physiol, 2001. **533**(Pt 2): p. 447-66.

87. Yuste, R., et al., *Ca2+ accumulations in dendrites of neocortical pyramidal neurons: an apical band and evidence for two functional compartments.* Neuron, 1994. **13**(1): p. 23-43.

88. Larkum, M.E., J.J. Zhu, and B. Sakmann, *A new cellular mechanism for coupling inputs arriving at different cortical layers.* Nature, 1999. **398**.

89. Caras, M.L. and D.H. Sanes, *Top-down modulation of sensory cortex gates perceptual learning.* Proc Natl Acad Sci U S A, 2017. **114**(37): p. 9972-9977.

90. Manita, S., et al., *A Top-Down Cortical Circuit for Accurate Sensory Perception.* Neuron, 2015. **86**(5): p. 1304-1316.

91. Xu, N.L., et al., *Nonlinear dendritic integration of sensory and motor input during an active sensing task.* Nature, 2012. **492**(7428): p. 247-51.

92. Carvell, G.E. and D.J. Simons, *Biometric analyses of vibrissal tactile discrimination in the rat.* The Journal of Neuroscience, 1990. **10**(8): p. 2638.

Acknowledgments

Special thanks go to:

- My supervisor Dr. Marcel Oberlaender, for your support, mentorship, the opportunity to contribute to so many great projects and most importantly your friendship.
- My thesis advisory committee, Prof. Dr. Heinz Beck and Prof. Dr. Stefan Remy for all of your constructive and helpful discussions.
- To all of my collaborators (in alphabetical order): Arco Bast, Dr. Robert Egger, Dr. Andrew Johnson, Dr. Gerardo Rojas-Piloni, Prof. Dr. Bert Sakmann, Mythreya Seetharama, Dr. Peter Strick and Elizabeth Wendell. Thank you so much for the great team work, your commitment to science, hard work, amazing talents and expertise. Without you all this thesis would not have been possible!
- To the students I supervised (in alphabetical order): Aman Maharjan (Master), Peter Park (Master), Fiorella Osorio (Bachelor), and Li Yida (Master). It was a pleasure having the opportunity to work with and mentor you all on the “Rabies Project”. You have all done and continue to do an absolute amazing job.
- To all the members of the In Silico Brain Sciences Group: Thanks for your friendship, support and many helpful discussions.

Most of all:

My wife Allison: We have come a long way! I can never thank you enough for the sacrifices you made so I can have this opportunity. Thanks for you constant support and love. I would have never come this far without you!

To my children James and Owen: you two boys continue to amaze me each and every day. I love being your dad most of all.

RESEARCH SUMMARY

My current research, supervised by Dr. Marcel Oberlaender focuses on the structural and functional determinants of transforming sensory input into output activity patterns in the mammalian neocortex using various in vivo experimental methods. In 2017, we reported on the example of the rat barrel cortex, that layer V pyramidal tract neurons (PTs) have both certain structural properties and activity patterns that reflect their sub-cortical axonal targets. We therefore concluded that these target related properties may arise from PTs being imbedded into long-range target related cortical sub-networks. To test this hypothesis and to investigate these sub-networks in a brain-wide context, I began injecting both mono and multi-synaptic retrograde agents into the terminal points of brain-wide whisker related pathways; the whisker muscles of the rat's snout. From the results of these experiments thus far we were able to report in 2018 a method for generating a standardized model of the rat facial nucleus and where we described the synaptic input patterns of the whisker motor neurons located in the facial nucleus that innervate individual whisker muscles. Ongoing data analysis of the whisker injection results has also revealed that PTs can have a different synaptic distance to the whisker motor neurons depending on their sub-cortical target. For example PTs that project to the trigeminal complex of the brain stem have the shorter synaptic distance to the whisker motor neurons than PTs that project to the Thalamus or Pons. Most recently I have been investigating how top-down inputs to apical dendrites of PTs can modulate their sensory evoked cortical output patterns. By combining in vivo cell attached recordings with optogenetic manipulations, we discovered that the same neurons in the primary thalamus that provide feed-forward excitation to the basal dendrites of PTs, additionally form a zone of dense synaptic connections along their apical dendrite that corresponds with the location of calcium channels. Our data reveals a gating mechanism by where the primary thalamus can regulate how top-down distal inputs to the apical dendrites of PTs modulates sensory evoked cortical output patterns, providing insight to how the neocortex can integrate external information from the environment with internal states of the brain.